Stochastic Modeling of Aerodynamic Force Dynamics on Wind Turbine Blades Under Turbulent Wind Inflow

Muhammad Ramzan Luhur

Von der Fakultät für Mathematik und Naturwissenschaften
der Carl von Ossietzky Universität Oldenburg
zur Erlangung des Grades und Titels eines

DOKTORS DER INGENIEURWISSENSCHAFTEN
DR.-ING.

angenommene Dissertation

von Herrn Muhammad Ramzan Luhur
geboren am 05.10.1977 in Larkana, Pakistan.

CARL VON OSSIETZKY universität OLDENBURG

Gutachter: Prof. Dr. Joachim Peinke
Zweitgutachter: Prof. Dr. Martin Kühn
Tag der Abgabe: 15.07.2014
Tag der Disputation: 08.09.2014

Dedicated to
my father Late Bahadur Luhur and family

Contents

Abstract

In this dissertation we present the development of a sophisticated stochastic model to represent the dynamic lift and drag response of an airfoil exposed to turbulent wind inflow conditions. The dissertation is structured in five chapters as follows.

Chapter 1, at first presents the cutting-edge growth of wind power industry, secondly the wind turbines in use, next the design and aerodynamic performance of modern horizontal axis wind turbine, and then introduction to stochastic processes followed by aims and objectives.

Chapter 2 presents the measurements and the stochastic approach (namely the Langevin approach) applied to model the complex dynamics of lift and drag forces for an airfoil FX 79-W-151A. The parameters of the model are directly derived from wind tunnel measurements performed in the wake of a fractal square grid at turbulence intensity of 4.6%. The stochastic model achieved through this approach is extended to account for oscillation effects contained in lift and drag dynamics that probably stem from unsteady aerodynamic effects. The results are optimized by applying a χ^2 test on the probability density functions (PDFs) of model and measurements. The model and measurement statistics show good correspondence with each other. A comparison of classical averaging and the stochastic approach shows that stochastic analysis offers additional insight into the local lift and drag force dynamics.

Chapter 3 presents the combination of the stochastic model with a well-known standard blade element momentum (BEM) model. The results show that in comparison to classical BEM model, the BEM model integrated with stochastic approach additionally reflects the local force dynamics on a rotating blade element, and therefore provides more information on aerodynamic forces that could be used by wind turbine simulation codes.

Chapter 4 presents the integration of the stochastic model into the aerodynamic simulation software AeroDyn. The proposed model in AeroDyn is integrated as an alternative to traditional table lookup method used by the classical BEM wake model. The stochastic forces are obtained for a rotor blade element using full field turbulence simulated wind data input and compared with the classical BEM and dynamic stall models for identical conditions. The comparison shows that the stochastic model generates additional extended dynamic response in terms of local force fluctuations. Further, the comparison of statistics between the classical BEM, dynamic stall and stochastic models' results in terms of their increment PDFs gives consistent results.

The last Chapter 5 summarizes the outcome and highlights the aspects that require further investigations.

The stochastic model is being developed to provide a proper description and characterization of the dynamic lift and drag forces under turbulent wind inflow conditions, which could contribute more dynamical loading information on wind turbine blades leading to an optimum rotor design. The goal for future work is to obtain an aerodynamic model such as AeroDyn completely integrated with the model under investigation, which could be combined with a wind energy converter model such as FAST to get a stochastic rotor model.

Zusammenfassung

In dieser Dissertation präsentieren wir die Entwicklung eines hochentwickelten stochastischen Modells, um den dynamischen Auftrieb und Widerstand eines Flügels in turbulenter Anströmung zu beschreiben.

Im 1. Kapitel wird anfangs das innovative Wachstum der Windenergieindustrie dargestellt, daran anschließend die aktuellen Windkraftanlagen, die zukünftigen Designs und die aerodynamischen Eigenschaften moderner Windkraftanlagen beschrieben. Einer Einführung in stochastische Prozesse folgen die Absichten und Ziele der Arbeit.

Das 2. Kapitel stellt die Messungen und den genutzten stochastischen Ansatz (Langevin-Ansatz) dar, um die komplexen Dynamiken von Auftriebs- und Widerstandskräften an einem FX 79-W-151A Flügelprofil zu modellieren. Die Modellparameter werden direkt aus Windkanal-Messungen im Nachlauf eines fraktalen Gitters mit einer Turbulenzintensität von 4,6% abgeleitet. Das so gewonnene stochastische Modell wird erweitert, um Oszillationen in der Auftriebs- und Widerstandsdynamik, die vermutlich von instationären aerodynamischen Effekten herrühren, Rechnung zu tragen. Die Resultate werden optimiert, indem ein χ^2-Test auf die Wahrscheinlichkeitsdichtefunktionen (PDFs) des Modells sowie der Messungen angewendet wird. Die Statistiken von Modell und Messungen zeigen gute Übereinstimmung. Ein Vergleich von klassischer Mittlung und dem stochastischen Ansatz zeigt, dass die stochastische Analyse zusätzlich Einblick in die lokalen Auftriebs- und Widerstandskraftdynamiken liefert.

Im 3. Kapitel wird das stochastische Modell mit einem wohlbekannten Blattelement-Impulstheorie-Modell (BEM-Modell) kombiniert. Die Ergebnisse zeigen im Vergleich zu klassischen BEM-Modellen, dass die lokalen Kraftdynamiken an einem rotierenden Blattelement aufgelöst werden. Diese zusätzlichen Informationen könnten von Software zu Windkraftanlagensimulation genutzt werden.

Die Integration des stochastischen Modells in die Software AeroDyn zur Aerodynamiksimulation wird in Kapitel 4 dargestellt. Das vorgeschlagene Modell wird als Alternative zu traditionellen Lookup-Tabellen, die von klassischen BEM-Nachlauf-Modellen genutzt werden, implementiert. Die stochastischen Kräfte werden mit Hilfe eines simulierten turbulenten Windfeldes für ein Rotorblattelement gewonnen und mit dem klassischen BEM-Modell und dynamischen Strömungsabriss-Modellen unter identischen Bedingungen verglichen. Der Vergleich zeigt, dass das stochastische Modell erweiterte dynamische Antworten im Bezug auf lokale Kraftfluktuationen liefert. Weiterhin liefert der Vergleich der Inkrement-PDFs

des klassischen BEM-Modells, der dynamischen Strömungsabriss-Modelle und des stochastischen Modells konsistente Resultate.

Das letzte Kapitel 5 fasst die Ergebnisse zusammen und stellt die Aspekte heraus, die weiterer Forschung bedürfen.

Das stochastische Modell wird entwickelt, um eine angemessene Beschreibung und Charakterisierung der dynamischen Auftriebs- und Widerstandskräfte bei turbulenten Anströmbedingungen zu liefern, was mehr Informationen über die dynamische Belastung von Windturbinenblättern bereitstellt und so zu einem optimalen Rotor-Design beitragen könnte. Ziel ist es, in der Zukunft ein stochastisches Rotormodell zu erhalten, indem das untersuchte, mit AeroDyn gekoppelte Modell vollständig in ein Windenergieanlagenmodell wie FAST integriert wird.

Chapter 1

Introduction

1.1 Wind energy

The growing population and modernizing life standard lead to a substantial increase in energy demand. The conventional energy sources alone, are not sufficient to face the growing demand of energy. Furthermore, the most conventional units are based on fossil fuels, which are not only decreasing but deteriorating the environment also. The demand for clean and increased energy, forces to explore and utilize the sustainable energy sources such as solar, wind, tides, biomass, waves, hydro, biofuels and geothermal, etc. Wind energy is a renewable, widely distributed, affordable, clean and environment friendly resource [1].

Wind energy being safe, significant and fundamental for economical as well as social development, is successfully penetrating the energy market. The current developments in policy improvements, innovation and cost reduction by industry boosted up the wind energy market [2]. According to 2012 wind energy statistics, the international wind power industry continued its most dynamic growth with an annual growth of 10% and a cumulative capacity of 19% [3]. At the end of 2012, with an annual market growth of 45 GW, the total global installed capacity approached a level of 282.5 GW; see Figures 1.1 and 1.2.

In terms of annual installations, for USA, 2012 was the distinct year ever, with the addition of 13.12 GW made it global leader of the new installations. China contributed 12.96 GW of new capacity with a significant drop compared to its last three years. However, on a cumulative basis China is still in the lead with a total capacity of 75.32 GW; see Figure 1.3. In 2012, Europe added 12.74 GW of new installations, which is more than expected,

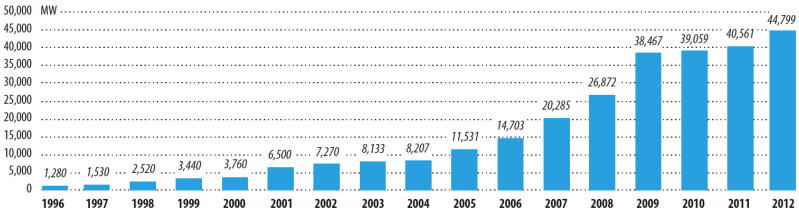

Figure 1.1: Global annual installed wind power capacity 1996-2012. Taken from [3].

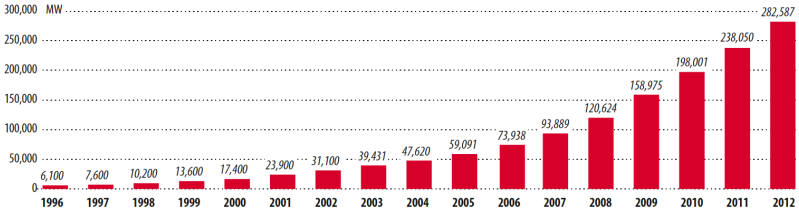

Figure 1.2: Global cumulative installed wind power capacity 1996-2012. Taken from [3].

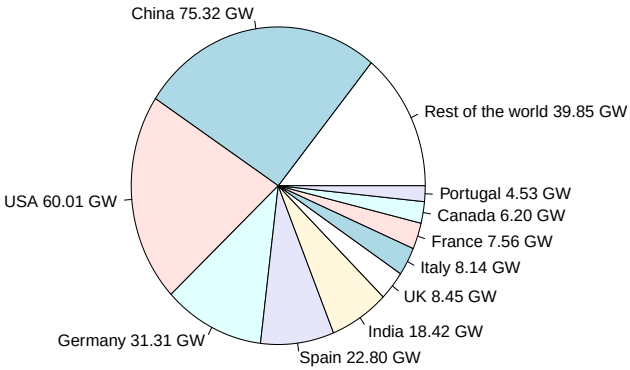

Figure 1.3: Top ten countries cumulative installed wind power capacity by the end of 2012. Reproduced from [3].

i.e. despite political uncertainty since 2011 [3]. The given statistics witnesses a significant progress of technology; however, still there are several aspects, where further research and improvements are necessary.

1.2 Wind turbines

The exploitation of power from wind is not a new technique, rather a thousands of years old approach. Famous historical windmills made from stones, cloth and wood were used for water pumping and grinding corn [4]. Wind turbines are machines, which extract kinetic energy from wind and convert it into electrical energy. Names to these machines can be assigned based on their application. If it is used for power production, it may be called a wind turbine. Similarly, if it is used for any other application, such as grinding grain or water pumping, it may be called a windmill or wind pump.

Wind turbines in the context of orientation of rotation with respect to the ground, are divided into two classes; the horizontal axis wind turbines (HAWTs) and the vertical axis wind turbines (VAWTs). The HAWT blades rotate around an axis parallel to the ground and VAWT blades rotate around an axis perpendicular to the ground; see Figure 1.4. Both types are available in number of varieties in the market.

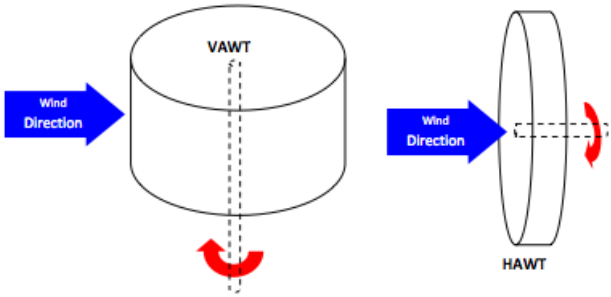

Figure 1.4: VAWT and HAWT orientation of rotation. Taken from [4].

Based on the principles of propulsion, wind turbines are further grouped into two categories; the lift and the drag based wind turbines. The method of propulsion has significant effect on the rotor maximum achievable efficiency [4]. The early persian vertical axis windmills developed in about 500-900 A.D used the drag principle. These windmills work by exposing half of their sails to the wind, which are pushed by the drag force causing the windmill to rotate as shown in Figure 1.5. The fully exposed (to wind) designs use curved blade shapes, which attain a lower drag coefficient on return into the wind. Latter concept can be found in the form of cup anemometer rotors and ventilation cowls nowadays [4].

The drag based wind turbine concept is the least efficient type. It attains its maximum efficiency when its collector is pushed away from the

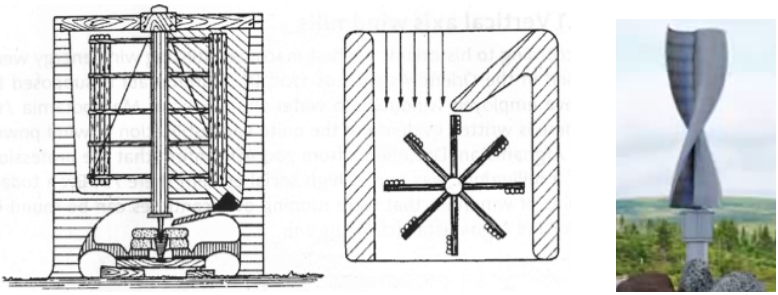

(a) (b)

Figure 1.5: Drag based wind turbines. (a) Early Persian windmill design and (b) Savonius wind turbine. Taken from [5, 6].

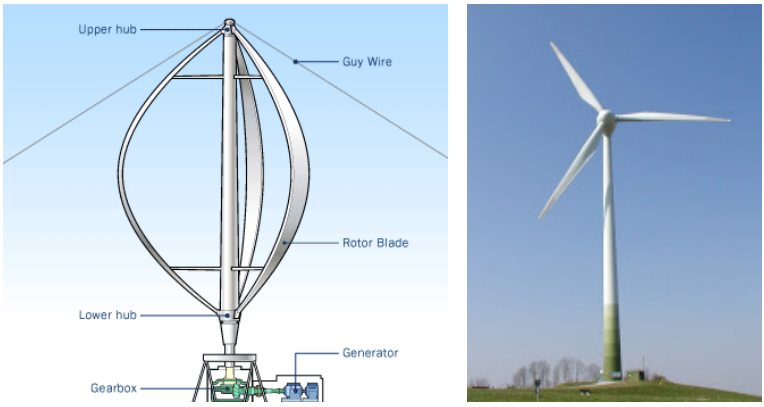

(a) (b)

Figure 1.6: Modern lift based wind turbines. (a) Darrieus vertical axis wind turbine and (b) horizontal axis wind turbine. Taken from [7].

wind [5]. The main drawback for its lower efficiency, is the consistent wind direction for force and rotation of the sail, which causes reduction in relative wind velocity with the increase in rotor speed [4].

The modern wind turbines are mostly lift based, which use blades made of airfoils. The wind flow over the airfoil surface with the combined effect of pressure and skin friction results in an aerodynamic force [8]. The resultant aerodynamic force consists of the lift and drag components acting perpendicular and parallel to the prevailing wind, respectively. The lift force being a multiple of the drag, is the relevant driving power of the wind turbine rotor [9].

1.2.1 HAWT versus VAWT

The HAWT is the most common and dominant type of wind turbine. The HAWTs with less blades (i.e. two or three) are more efficient for power generation. The addition of more blades result in a low tip speed ratio (TSR)[1]; therefore, generate less power. The torque increases but it does not support more power generation. An increase in shaft speed using any type of gearing seriously hurts the power output, particularly for low wind speeds. Use of three blades gives the best compromise of TSR versus torque resulting in higher power coefficient; see Figure 1.7. Any design with increased rotor solidity would not be suitable for efficient power generation [10]. The turbines with more blades are used for water pumping. Increased number of blades produce high starting torque suitable for fully automatic water pumping especially at increased wind speeds.

The VAWTs are less frequently used wind turbines. The VAWT development is mostly restrained by its low TSR and difficulties in controlling the rotor speed [4]. It yields low power coefficient in particular due to use of symmetric airfoils and lower part operation in boundary layer being close to ground. Additional drawbacks include self-starting incapability [11] and high torque fluctuations in each revolution. However, it operates independent of the wind direction (thus requires no any yaw mechanism) and advantageous in reduced tower load as its heavy generator equipment can be placed on ground [4].

1.2.2 Power coefficient

The power coefficient is the ratio between power extracted by the turbine and power available in the wind. The expression in mathematical form reads

$$C_p = \frac{P_{turbine}}{P_{wind}} = \frac{P_{turbine}}{\frac{1}{2}\rho A u^3}, \tag{1.1}$$

where C_p is the power coefficient, ρ the air density, A the rotor area and u the inflow wind speed.

For different wind turbine rotor designs, power coefficient is described as function of TSR and all other rotor dimensions are determined around this parameter. The higher tip speeds require narrow blade profiles with minimal material usage, thus, low production costs [4]. With the increase in tip speed, the blade aerodynamics becomes increasingly critical and results in higher cut in speed [12], which leads to self-starting difficulties. The

[1] TSR is the ratio between the wind turbine blade tip speed and the inflow wind speed, expressed as $\lambda = \frac{\omega R}{u}$, where ω is the blade rotational speed and R the blade radius.

modern HAWT is generally found to produce efficient power at TSR of nine-to-ten with two-bladed rotor and six-to-nine with three-bladed rotor [13, 14]; see Figure 1.7.

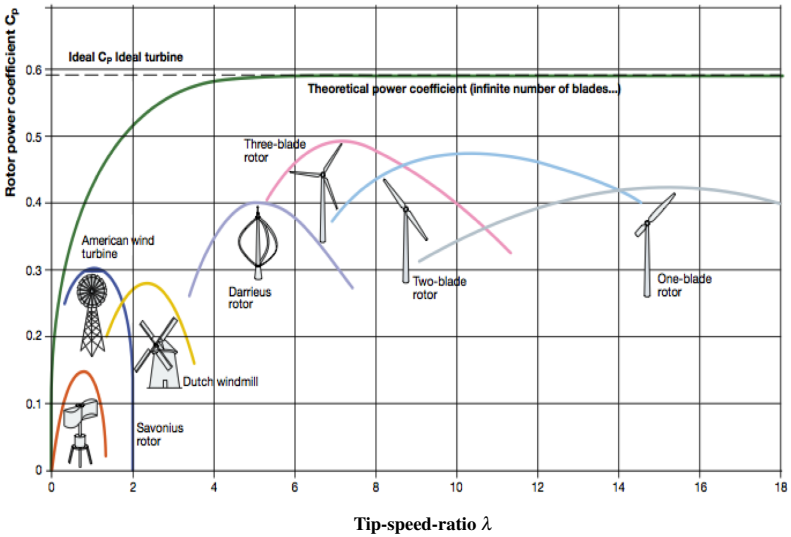

Figure 1.7: Power coefficient for different wind turbine rotor designs. Taken from [15].

For increased energy extraction from wind, the rotor efficiency is desired to be maximized within the affordable production limits. The well accepted ideal efficiency that a wind turbine could achieve in maximum is 59.3%, referred as Betz limit [14, 16, 17]. The Betz theory is based on uniform and linear wind velocity, i.e. axial wind velocity before and after the rotor. It ignores the wake rotation as well as turbulence caused by drag or tip vortices that further reduce the maximum efficiency. Therefore, the maximum ideal efficiency is yet to be perceived [18]. The losses from latter phenomena can not be ignored completely. However, such losses could be minimized through design improvements. The general steps to cut down the losses include; the decrease of wake rotation by increasing TSR, selection of airfoils with high lift-to-drag ratio and specialized tip configurations [4].

In practice, the peak efficiency of any wind turbine depends on its design. The historic drag based Persian windmill concept; the Savonius rotor attains the maximum efficiency of 16% and modern day cup anemometer up to 8%. The lift based American wind turbine and the Dutch windmill

achieve the peak efficiency of 31% and 27%, respectively. The modern lift based VAWT; the Darrieus rotor approaches the efficiency of 40% in maximum, whereas the HAWT with three blades attains the maximum efficiency close to 50% as shown in Figure 1.7.

1.3 Design and aerodynamics of HAWT

The aerodynamic research is very important and old science in wind energy, and has significant role in the success of modern wind energy systems [19]. The aerodynamics of the wind turbines is the study of wind flow pattern around and through the rotor, and the power extracted by the rotor. The Figure 1.8 shows the schematic of velocity and forces acting on a blade section of modern HAWT. These types of wind turbines are most widely

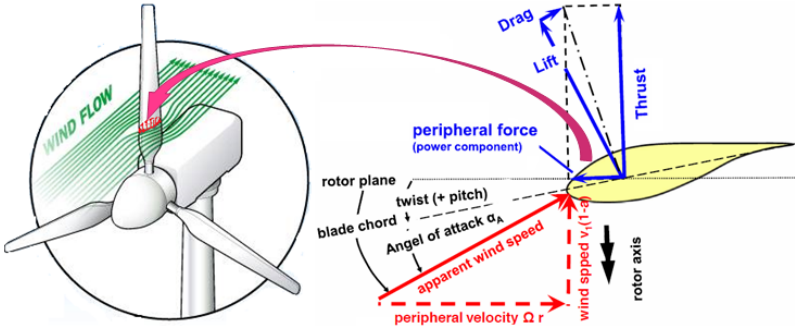

Figure 1.8: Schematic of velocity and forces acting on HAWT blade element. Taken from [20, 21].

used for power generation. The HAWT rotor extracts energy from the wind flowing around the blades. The bound circulation around the blades causes the lift and drag forces, which produce the mechanical energy with their combine effect. The produced mechanical energy is then either converted into electrical power or directly used for any other application. Compared to other types of the wind turbines, HAWT is predicted and experienced to have superior characteristics particularly in terms of higher efficiency [22].

For an efficient rotor design aerodynamic performance is very basic aspect to consider [23]. The components of aerodynamic force; the lift and drag have the key role in an appropriate rotor design. The lift force contributes to the power yield and drag force prevents the blade rotation. Thus, the objective is to maximize the lift and minimize the drag, i.e. high lift-to-drag ratio. The airfoil section typically with lift-to-drag ratio more

than 30 is recommended for rotor blade design [4, 23, 24]. The expression for lift-to-drag ratio reads

$$\varepsilon = \frac{C_L}{C_D}, \tag{1.2}$$

where C_L is the lift coefficient and C_D the drag coefficient.

The structural considerations suggest the use of airfoils with high thickness-to-chord ratio at root-part of the blades to withstand the intensive loads. The thick airfoils have usually low lift-to-drag ratio; therefore, for wind turbine blade design, thick airfoils are made with great care to maximize their lift [25, 26]. The mid-span and tip-part of the blade require more consideration to aerodynamic properties [26]. The blade tip-part needs thin airfoils to have reduced loads, strong linear velocity and good aerodynamic performance. It is believed that the use of latest materials with advanced mechanical properties may permit the use of thin airfoils even for root-part of the blade with higher lift-to-drag ratios [4]. More information on airfoil characteristics desired for different regions of the blade span can be found in Table 1.1.

Table 1.1: Desirable characteristics for airfoils for different regions of the blade along the span. Reproduced from [26].

Parameter Description	Root	Mid-span	Tip
Thickness-to-chord ratio	>27%	27%–21%	21%–15%
Structural load bearing requirement	High	Medium	Low
Geometrical compatibility	Medium	Medium	Medium
Maximum lift insensitive to leading edge roughness			High
Design lift close to maximum C_L off-design		Low	High
Maximum C_L and post stall behavior		Low	High
Low airfoil noise			High

Moreover, the wind turbines operate at boundary layer for long periods of time exposed to dust and bugs, which accumulate on the blade surface and affect the aerodynamic performance, in particular the lift generation. The phenomenon is known as fouling [25]. The development of wind turbines from specific airfoil profiles is mainly pushed by the blade sensitivity to fouling and off-design conditions [13, 26].

1.3.1 Airfoil characteristics and blade shape

The estimation of the lift and drag coefficients are based on angle of attack (AOA). It is the angle between the chord and apparent/relative wind speed. The airfoil sections along the blade span observe different apparent wind speed, thus, different AOA and different magnitude of the lift and drag

forces, which lead to different structural requirements. Therefore, the airfoil sections for different regions of the blade along the span are required to be designed according to their local conditions. Additionally, manufacturing of a blade using a single type of airfoil can also result in an ineffective design [23]. An efficient blade design may contain multiple airfoil types merged at twist angle ending at a round rim [16, 27] as shown in Figure 1.9.

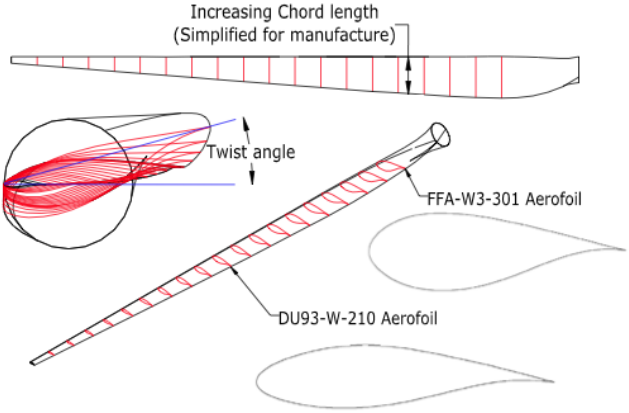

Figure 1.9: HAWT blade with multiple airfoil types and shape distribution along the span. Taken from [4].

For better efficiency, several simplifications may be considered such as reduction in twist angle, linearization of chord width and selection of reduced number of differing airfoils. Nowadays most of the foremost wind turbine manufacturers are considering nearly all these optimization aspects, i.e. the twist, variable chord length and multiple airfoil configurations [4].

Optimum chord length

Today, there are various methods to calculate the optimum chord length [28, 29, 30]. The simplest one is the method based on Betz optimization [4], which produces the basic shape of modern wind turbine blades. This can be achieved using blade element momentum (BEM) theory considering the Betz limit, local flow velocities and airfoil lift. In this context, the expression reads [31]

$$c(r)_{Betz} = \frac{1}{B}\,\frac{2\pi R}{C_L(\alpha)}\,\frac{8}{9}\,\frac{1}{\lambda_D\sqrt{\lambda_D^2\,(\frac{r}{R})^2+\frac{4}{9}}}, \tag{1.3}$$

where $c(r)_{Betz}$ is the local optimum chord length according to Betz limit. The parameter B represents the number of blades, r the local radius of blade, R the tip radius of blade, λ_D the chosen design TSR and $C_L(\alpha)$ the lift coefficient at design AOA. The design value for $C_L(\alpha)$ is usually taken close to best lift-to-drag ratio, i.e. at ε_{max}, $C_L = 0.6 - 1.2$ and $\alpha = 2^\circ - 6^\circ$. The equation (1.3) provides the information on chord distribution along the blade span. The selection of the number of blades depend on the material strength and manufacturing or dynamic aspects. The equation (1.3) in its more transparent and simplified form can be written as [31]

$$c(r)_{Betz} \approx 2\pi R \frac{1}{B} \frac{8}{9C_L(\alpha)} \frac{1}{\lambda_D^2(\frac{r}{R})}. \tag{1.4}$$

This simplified form can be used for turbines operating at high TSR, i.e. $\lambda_D > 3$. For blade designs having negligible drag and tip losses, operating in the TSR range of six-to-nine, Betz momentum theory holds with good approximation [4, 13]. However, in cases such as at low tip speeds, the blade designs utilizing airfoil sections with high drag and for blade sections at hub, this approach could be regarded unreliable. In latter cases, the wake and drag losses must be considered [4, 16, 28].

Optimum thickness

The optimal thickness of the airfoil along the blade radius depends on several factors, such as rotor design, aerodynamic loads, structural integrity and minimum cost. It varies inversely through the blade root to tip as described by the following relation [32]

$$t(r) \propto \frac{1}{r}, \tag{1.5}$$

where $t(r)$ is the local thickness of the blade. The root-part of the blade subjects to low relative wind velocity (because of small radius), which results reduced aerodynamic lift necessitating the use of large profiles at rotor hub. At this load intensive part, profiles require excessive thickness to ensure the structural integrity. With the increase in radius, there is increase in relative wind velocity, and thus increase in aerodynamic lift, which allow the use of thinner profiles with possible structural considerations at mid-span to tip [4]. Simply stated, the more the blade section distance from the root, the less the section thickness as illustrated in Figure 1.10.

The ratio of thickness-to-chord plays very crucial role in blade configuration as well as its geometric consistency. The ratio can be kept constant along the blade length. The change in thickness-to-chord ratio along the

blade radial length necessitates that the individual airfoils for varied thicknesses well correspond together to ensure the smooth shape of the blade [26].

Optimum twist angle

The blade rotational speed is proportional to the distance from its root. The more the distance from the root, the more the blade rotational speed; see Figure 1.10. The increase in blade speed causes the increase in apparent

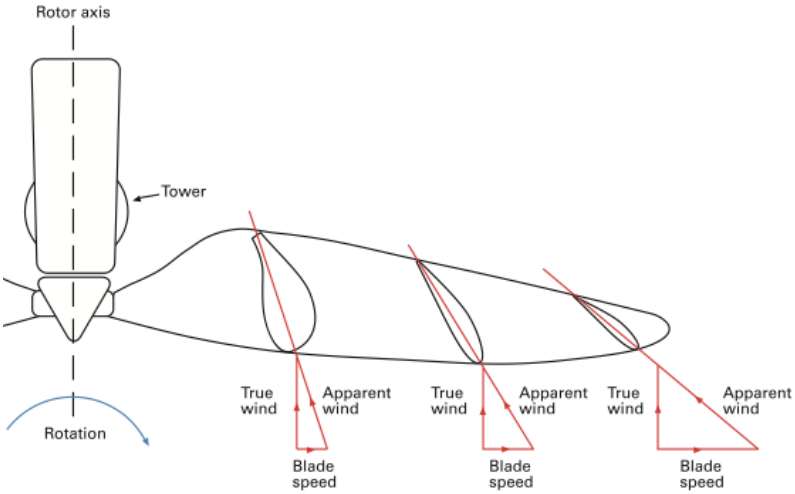

Figure 1.10: Components of apparent wind and resulting blade twist distribution along the span. Taken from [33].

wind speed and apparent wind angle. Thus, to maintain an optimum AOA for each blade section, blade must be twisted along the span. The typical twist distribution range from root to tip is $0^\circ - 20^\circ$ [14]. According to Betz, the blade optimum twist angle along the span can be determined using the relation [31]

$$\beta(r)_{Betz} = arctan\left(\frac{2}{3}\frac{R}{r\lambda_D}\right) - \alpha(r), \tag{1.6}$$

where $\beta(r)_{Betz}$ is the local optimum twist angle at Betz limit. The local twist angle in combination with pitch angle gives the local angle between rotor plane and chord of the blade; see Figure 1.8.

1.3.2 Smart blades

The wind turbine rotor blades are continously growing in size. The upcoming generation of the turbines intend to approach the size up to 20 MW, which could lead to several challenges such as increase in cost, weight and aerodynamic loads. To control the latter factors, modern research in blade design is aiming to realize the blades, which adjust their shape according to local wind situation. The concept could be important for wind turbines of size > 10 MW in particular. The general aim is to minimize the ultimate and fatigue loads to minimize the total cost of wind turbines. The research-move for smart blades, for the application of wind turbines, is the continuation of concepts from helicopter control. Work in this direction, is being carried out by different wind energy institutes under different projects [4, 34]. For example, German Environmental Ministry (BMU) project "Smart blade" [35], European Energy Research Alliance (EERA) initiated project "AVATAR" [36], European Commission funded UpWind project "Smart rotor blades and rotor control for wind turbines" [37], the Delft University project "Smart dynamic rotor control for large offshore wind turbines" [38] and the Danish national project "ADAPWING". The International Energy Agency (IEA) 50th and 56th topical expert meetings at Delft University in December 2006 and Sandia National Labs in May 2008, respectively on "The application of smart structures for large wind turbine rotors" also indicate the research progress in this direction [39, 40].

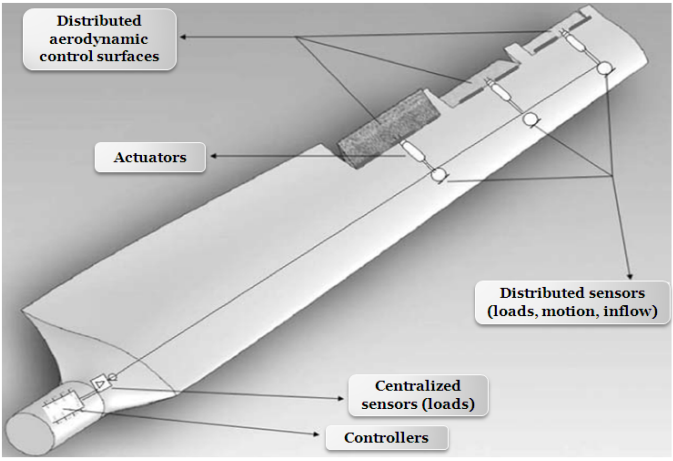

Figure 1.11: Design view of a smart rotor blade. Taken from [34].

The wind turbines with smart blades use different control concepts, which include; distributed aerodynamic control surfaces, actuators, sensors and controllers as shown in Figure 1.11 [34]. The control devices change the blade local aerodynamic characteristics and provide the required control actions. The actuator smart materials have the property to sense and drive in a controlled way in response to change in surrounding flow conditions [4, 34]. The concept of smart blades equipped with active flow control systems, is believed to replace the traditional pitch system and allow the manufacturing of even bigger size wind turbines [41]. However, such blades which require smart control system with possible high voltage, may attract more lightning strikes than the conventional blades [37].

1.3.3 Design codes

In order to carry out the wind turbine design calculations or model its dynamic behavior, several approaches do exist today. These are based on BEM wake, free wake vortex, acceleration potential and computational fluid dynamics (CFD) methods [19, 42, 43, 44, 45]. These methods basically were developed to deal with propeller and helicopter aerodynamics, but later used to model the HAWT aerodynamics [46]. A brief description and features of some commonly used design codes are presented in Table 1.2.

Compared to engineering methods, high fidelity CFD methods are very time consuming in computational terms. In case of large problems, CFD can take up to a week, while engineering methods need only few seconds. In addition, CFD needs significant expertise to run and interpret the results [47]. The CFD methods solve numerically either Euler or Navier-Stokes equations, and for wind turbine aerodynamics are related to turbulence modeling in particular [48]. Generally, for the calculation of wind turbine aerodynamics, engineering methods represent the best choice in computational terms, in particular for aeroelastic simulations [49]. Nevertheless, future increased computer power may make it possible to replace the classical methods with more advanced models to integrate into aeroelastic codes [46]. In this context, four wide categories of CFD techniques are believed to extend advancement over current design codes. These include the actuator disc/surface/line technique, hybrid Reynolds Averaged Navier-Stokes/Large Eddy Simulation (RANS/LES) method, Full Blade and Rotor CFD method (overset CFD solver), and coupling between CFD and Computational Structural Dynamics (CSD) [50].

Looking at the current situation, still most computational studies of wind turbine aerodynamics continue with simple and inexpensive classical BEM theory [51]. To predict for aerodynamic loads, different aeroelastic

Table 1.2: Design codes and their features

Design code	Feature
AeroDyn	Plug-in type package for computation of aerodynamic forces on wind turbine blades. It estimates the elemental forces at desired location and time, and delivers to dynamic analysis codes [52].
FAST	Fatigue Aerodynamics Structures and Turbulence code for predicting extreme and fatigue loads of HAWTs with AeroDyn routines [53].
ADAMS/WT	Automatic Dynamic Analysis of Mechanical Systems-Wind Turbine with AeroDyn routines for aerodynamic analysis of wind turbines [54].
SIMPACK	Multi-Body Simulation Software with interface to AeroDyn for wind turbine aerodynamic forces [55].
YawDyn	Used with ADAMS to simulate the yaw motions or loads of HAWT with a rigid or teetering hub [56].
DHAT	A traditional in-house wind-turbine-specific aeroelastic code. For aerodynamic calculations it uses BEM, dynamic and turbulent wake conditions, and dynamic stall options [57].
DUWECS	Delft University Wind Energy Converter Simulation in-house package in time domain for simulation and analysis of flexible wind turbines [58].
FLEX5	Simulates wind turbine dynamics with one to three blades, fixed or variable speed generator, pitch or stall power regulation [59].
BLADED	An integrated simulation package for wind turbine design and analysis [60].
GAST	General Aerodynamic and Structural prediction Tool for wind turbines [61]
HAWC2	Horizontal Axis Wind turbine simulation Code 2nd generation for simulation of HAWT response in time domain [62].
FLEXLAST	Flexible Load Analyzing Simulation Tool used by Dutch industries for wind turbine and rotor design [63].
PHATAS	Program for Horizontal Axis wind Turbine Analysis and Simulation. Code for time domain estimation of dynamic behavior and corresponding loads on the main components of a HAWT [64].
VIDYN	Simulation tool for static and dynamic structural analysis of HAWTs [65].
AERFORCE	Subroutine package for prediction of aerodynamic forces acting on the wind turbine rotors intended for use in aeroelastic codes [66].
ONERA	Semi-empirical dynamic stall model based on a set of non-linear differential equations, which describe the unsteady airfoil behavior [67].
DYNSTALL	Subroutine package with Beddoes-Leishman semi-empirical dynamic stall model for calculation of two-dimensional (2D) unsteady airfoil aerodynamics [68].
Snel Model	Semi-empirical dynamic stall model for use in aeroelastic design codes for wind turbines [69].
TURBU Offshore	Tool for combine frequency/time domain analysis of offshore HAWTs to asses turbine dynamic behavior in different sea-states and wind conditions [70].
ADCoS	AeroDynamic Consult GmbH (ADC) for load simulation of onshore wind turbines using Finite Element approach [71].
SOLVIA	Commercial Finite Element program for modeling of structural dynamics [72].
EllipSys3D	Navier-Stokes solver program for complete 3D CFD computations considering steady state conditions with a moving mesh technique [73].
FLUENT/CFX	Simulate wind turbulence and aerodynamic characteristics [74].

design codes use BEM method yet today, particularly because of its computational efficiency. The BEM is significantly accurate when handling with

attached flows in axial direction. However, it lacks to model the complex flow fields around the rotor when handling with stalled and unsteady flows, especially in rotor yaw [46, 49]. Therefore, BEM is used with some assumptions and correction models. Regardless, the validation studies have witnessed its good predictions for turbine loads and performance [42].

1.4 Performance of HAWT

1.4.1 Turbulence and unsteadiness

The wind turbines in open-air experience unsteady, three-dimensional and strong turbulent flows, as they operate in atmospheric boundary layer known as surface layer. In this layer, the frictional forces and obstacles cause delay in wind, which result variations in wind speed and direction. In addition, the existence of seas and large lakes contribute circulatory motions to air masses. The level of wind instability decreases with increase in height from the ground surface, as the effects driven with interaction of earth surface get weaker [75]. The decline of shear effects allow the increase in wind speed. For wind energy applications, the wind shear is described by a power law profile, expressed as

$$u(z_2) = u(z_1)\left(\frac{z_2}{z_1}\right)^{\alpha}, \tag{1.7}$$

where $u(z_2)$ is the mean wind inflow velocity at height z_2 and $u(z_1)$ the mean wind inflow velocity at height z_1. The parameter α is the shape factor defined empirically based on local conditions of the location [41]. Collectively, the wind behavior at any location depends on; the stability of atmospheric boundary layer, the height from ground surface and the geographic conditions including landscape roughness and surrounding obstructions [75]. More precisely, the wind fields are the complex and unsteady structures with fluctuating properties in time and space. In addition, the wind turbine wake is one more factor, which adds up to the turbulence in wind farms. The observations manifest 5 to 25% increase in turbulence level in the wake of a wind turbine [76]. The higher turbulence level and the wake velocity deficit in wind farms, lead to increased dynamic loads on blades and reduced power production, respectively [77]. To comprehend this complex wind dynamics and integrate for corresponding effects into a wind turbine design, is one of the major challenges in present wind energy research and engineering.

In order to classify the wind situations, it is usual in engineering practice to use the turbulence intensity, expressed as the ratio of inflow standard

deviation σ_u to mean inflow $\langle u \rangle$ [78]. The relation reads

$$T_i = \frac{\sigma_u}{\langle u \rangle}, \tag{1.8}$$

where T_i is the turbulence intensity. The turbulence is believed to be the instability of laminar flow, which represents a smooth travel of fluid particles. The transition from laminar to turbulent flow can be determined from a well-known parameter defined as the ratio of inertial to viscous forces of the fluid. This dimensionless parameter is termed as Reynolds number, expressed as [79]

$$Re = \frac{UD}{\nu}, \tag{1.9}$$

where U is the mean flow velocity, D the characteristic length scale of the flow and ν the kinematic viscosity. In laminar flow (low Reynolds numbers), the wind may have regular and stable behavior; however, in turbulent flow (high Reynolds numbers), the wind fluctuations have irregular and chaotic behavior in time and space [80].

Another property of the turbulence is the intermittency caused by extreme wind events. The intermittency represents the large velocity gradients in turbulence that reflects strong non-Gaussian tails in the probability density functions (PDFs) of the velocity differences $\delta u_\tau(t) = u(t+\tau) - u(t)$ at time lag τ [81] as shown in Figure 1.12. The observations manifest strong intermittent behavior of wind in turbulent flows [78, 82].

The intermittent behavior of the turbulence is not limited to atmospheric wind only, but have influence on the resulting torque, thrust and power output of the turbine also [82]. This is obvious from torque estimations by Mücke *et al.* [78] shown in Figure 1.13. The figure shows the comparison between the PDFs of torque increment $Q_\tau(t) = Q(t+\tau) - Q(t)$, achieved with the measured atmospheric wind and the synthetic wind generated with continuous time random walk (CTRW) model. Nevertheless, the important characteristic here to show, is the intermittency in torque contributed by the atmospheric turbulent wind. This can be witnessed from heavy tailed PDF of the Q_τ for measured atmospheric wind inflow.

In turbulent flow, the local AOA and the wind speed at rotor blades change continuously, which contribute unsteady aerodynamic loads on the blades [51, 83]. Even small-scale turbulence leads to a persistent unsteadiness in wind flows approaching the rotor blades [14]. The degree of unsteadiness associated with the flow field and the turbine operating conditions can be determined using the relation [42]

$$k = \frac{\omega c}{2V}. \tag{1.10}$$

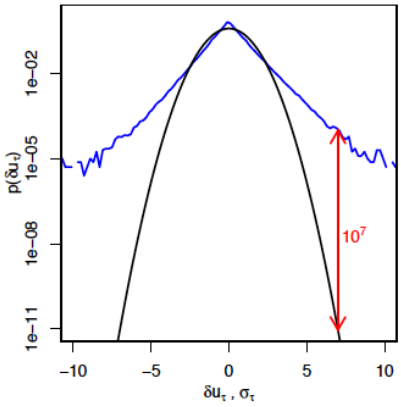

Figure 1.12: Comparison of a measured wind velocity increment $\delta u_\tau(t) = u(t+\tau) - u(t)$ PDF with a Gaussian PDF at same standard deviation for time lag $\tau = 3$s. The blue line represents the measurement PDF and black line the Gaussian PDF. The red arrow demonstrates their difference by a factor 10^7 at 7σ. The PDFs are normalized with their standard deviations. Taken from [82].

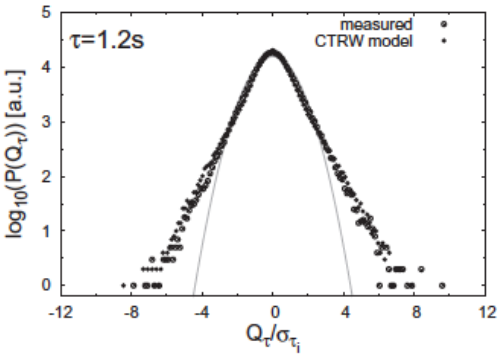

Figure 1.13: PDFs of torque increment $Q_\tau(t) = Q(t+\tau) - Q(t)$ for measured atmospheric wind inflow and CTRW model generated wind inputs for time lag $\tau = 1.2$s. The torque estimations are performed with FAST. The open circles represent the Q_τ PDF by measurements, solid points Q_τ PDF by CTRW model and grey line the corresponding Q_τ Gaussian PDF. The PDFs are normalized with their standard deviations. Taken from [78].

Here, the dimensionless parameter k represents the reduced frequency which defines the level of unsteadiness to the flow, ω the characteristic

physical frequency of the flow (circular frequency), $\frac{1}{2}c$ the airfoil semi-chord length and V the resultant local flow velocity at blade element. The equation (1.10) gives the information about the relationship between reduced frequencies and the unsteady disturbances to a flow. In connection to values of k, the flow types can be described as $k = 0$ represents a steady flow, $0 < k \leq 0.05$ a quasi-steady flow, $0.05 < k \leq 0.2$ an unsteady flow and $k \geq 0.2$ a strongly unsteady flow [84].

The large variations in wind velocity at short time scales can have substantial effect on the wind turbine's extreme alternating loads [78, 83]. The fluctuating loads cause variability in the turbulence spectrum as well as response statistics of the turbine [85]. The extreme wind events and the resulting loads compose a major challenge for wind turbine development and optimization. In particular, the build up and dissemination of the extreme loads through rotor aerodynamics yet need to be well understood. The cost optimized wind turbines with minimal usage of material and relatively flexible structures can subject to increased loads due to increased response to turbulent inflow, wind shear and tower shadow effect [83].

The wind shear can result a very complex wake structure at downstream of the wind turbine rotor with considerable irregularities including generation of stream-wise vorticities and non-periodicities. Moreover, the wind shear leads to uneven pressure variations on blade surfaces which cause extreme fluctuations in thrust and power produced by the turbine. Under such fluctuations, the turbine may face critical structural and vibrational problems, which could be harmful for wind turbine life [86]. Therefore, while designing a wind turbine, it is very essential to consider as many physical factors as possible. In particular, the three-dimensional flow features, span-wise dependency and viscosity effects are the most important physical effects, which need to be included in a correct and effective way [73].

1.4.2 Dynamic stall

In aerodynamics, stall is a condition where lift begins to decrease with increase in AOA beyond a certain point. Stall behavior originates at large AOAs, where flow separates over upper surface of the airfoil before leaving the trailing edge. The stall could also occur unexpectedly during a sudden blow of wind. The flow separation causes wake[2] to flow over upper surface of the airfoil, which leads to substantial decrease in lift force and increase in drag force [14]. For aircrafts, stall condition is considered hazardous; however, for wind turbines, this has been used to limit the maximum power output to avoid the generator overloading as well as increased forces on

[2]Disturbed flow (mostly turbulent)

blades in high wind speeds [4, 13]. In relation to unsteady flows over the airfoils, stall investigation is one of the important and usual aspects to consider. The typical AOA range of stall occurrence is $8^\circ - 20^\circ$ depending on the Reynolds number and geometry of the airfoil [79].

Stall behavior is grouped into two categories; the static and the dynamic stall. The static stall represents the stall occurrence in stationary state of the airfoil and the dynamic stall represents the stall occurrence in moving state (rapid change in AOA) of the airfoil. The dynamic stall can occur on any airfoil or lifting surface under time-dependent pitching, plunging or any other type of motion [42]. The physics of flow separation and stall evolution in dynamic stall differ from process manifested in static stall for same airfoil [87]. Stall in dynamic case occurs at higher AOAs than static case. The aerodynamic force coefficients in dynamic stall can largely exceed the maximum values compared to achieved in static stall; see Figure 1.14.

In unsteady flow, the fast variations in AOA lead to dynamic stall effect, which results substantial enlargement in the lift dynamics; compare [87, 88, 89, 90]. The dynamic stall is a viscous effect on airfoil properties, which generates rotating motion of the fluid particles on the blade surfaces during stall [91]. More simply, in dynamic stall, a strong vortex generates and detaches from the leading edge, and convects over upper surface of the airfoil; see Figure 1.14. The phenomenon causes rapid increase in lift generation in start, and ends with drastic decrease in lift as vortex leaves the trailing edge [87, 88, 89]. This behavior forms hysteresis loops in the force coefficients (as can be seen in Figures 1.14 and 1.15) with cyclic pressure loads, which are unforeseen by the usual lift and drag data achieved at steady AOAs [92]. The Figure 1.15 presents the comparison of steady lift coefficient to dynamic lift coefficient at different levels of unsteadiness k, and identifies that the level of unsteadiness has considerable impact on the lift dynamics. The higher the degree of unsteadiness, the higher the impact on lift dynamics [89].

It is obvious that the dynamic stall is a complex aerodynamic phenomenon, in particular because of its nonlinear behavior and dependency on parameters such as pitching frequency and pitching amplitude of the airfoil [79]. The dynamic stall effect is studied very widely; however, most of the studies are limited to wind tunnel experiments for two-dimensional (2D) oscillating (in pitch) airfoils. The investigations for other types of motions, such as plunging oscillations and constant angular rate (ramp) have not been given sufficient consideration. For proper understanding of dynamic stall involving nonlinear physics of much importance, it is very desirable to examine different modes of forcing. Investigation of one type of forcing may be insufficient to understand the nonlinear behavior of the

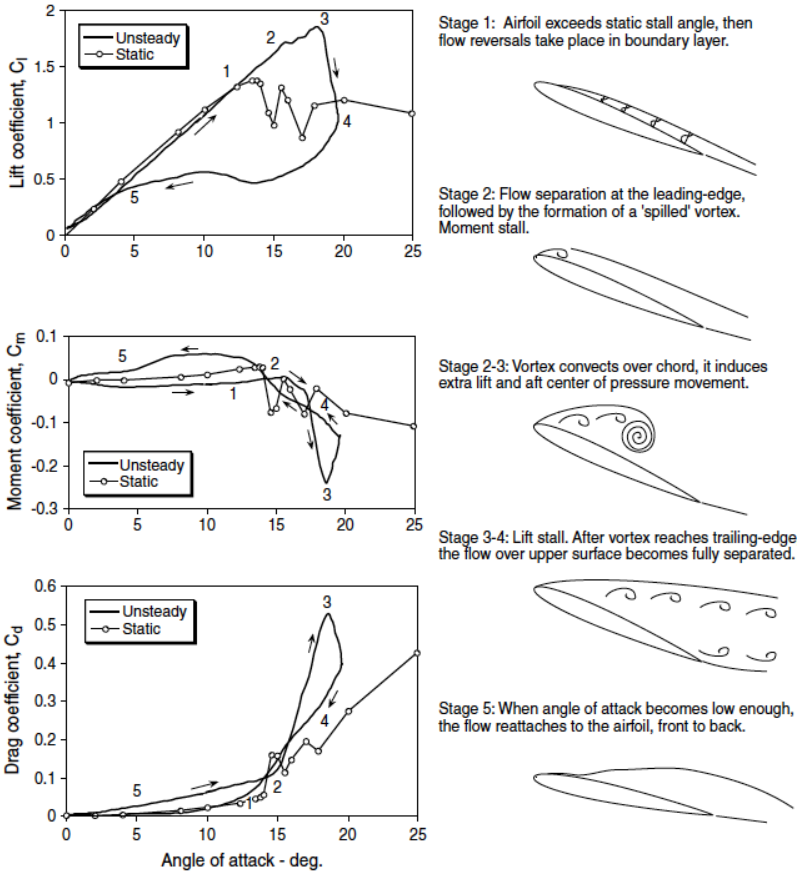

Figure 1.14: Unsteady flow physics and resulting forces for a 2D airfoil in dynamic stall. Taken from [42].

problem [42].

Today, several dynamic stall models do exist, which can be used for wind turbine load analysis. These are based on empirical and semi-empirical methods [79]. The empirical models such as *UTRC* α*, A, B* and *Boeing-Vertol 'Gamma' Function* use force measurements from 2D oscillating airfoils performed in wind tunnels and try to re-synthesize the measured forces using some functional relationships. The latter type of models are very rare and currently being used by helicopter community in particular. The semi-empirical models such as *Beddoes's Time Delay Method*, *Gangwani's Method*, *Johnson's Method*, *ONERA*, *Beddoes-*

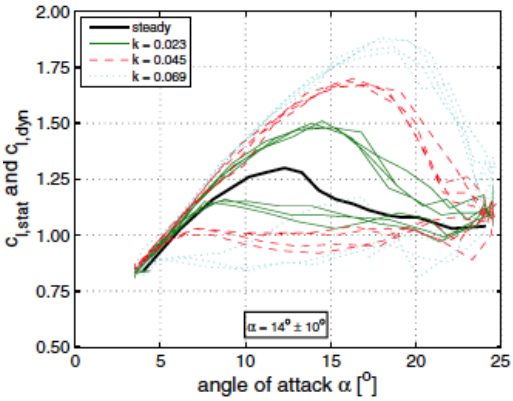

Figure 1.15: Comparison of steady C_L with dynamic C_L at different levels of unsteadiness k for NACA 4415 airfoil. Taken from [89].

Leishman's Method etc., use the sets of linear and nonlinear equations for lift, drag and pitching moments to represent the essential physics. The nonlinear equations may use several empirical coefficients obtained mostly through unsteady airfoil measurements [42].

Although, literature review witnesses the wide study of problem; however, the theoretical progress is somewhat slow on this [79]. In addition, the accuracy of the developed models is also question mark yet particularly in deep stall regime. Still further research and significant improvements in dynamic stall modeling are essential especially in mentioned regime [89].

1.5 Stochastic processes

The wind turbines operate in complex and unsteady wind fields that possess random variations in time and space; see Section 1.4. Thus, the resulting aerodynamic forces on the wind turbine blades appear to be dynamic and random. The systems involving random variability can be termed as stochastic systems and are modeled using stochastic differential equations. The dynamics of such systems is mostly based on fluctuations observed in time.

The stochastic processes can be grouped into two basic categories; one, which represents a sequence of random variables in time domain and the other, which represents a random field in space. The stochastic processes in time domain used to describe the diverse phenomenon such as fluctuating stock market prices or thermal fluctuations of a physical system, whereas

the stochastic processes in space domain describe the systems such as static images or random landscapes.

The stochastic processes can describe the systems from macroscopic to microscopic degrees of freedom. The complex systems are comprised of large number of microscopic subsystems with inconsistent behavior on fast time scales; so called fast dynamics or fluctuations, usually treated as random variables [93]. The systems involving considerable degrees of freedom, are generally described by low dimensional macroscopic order parameter equations, and the effect of microscopic degrees of freedom is considered through dynamical noise (fluctuations) [94, 95]. The dynamical noise is added as superposition to trajectory generated through deterministic dynamical system [93].

Moreover, a stochastic process can be a purely random process, a Markov process or a general process [96]. A process can be termed purely random, if it does not depend on the values of variable in earlier states. It is purely a memoryless process. The statistical description of such process in terms of conditional PDF can be described as

$$p(x_n,t_n|x_{n-1},t_{n-1};...;x_1,t_1) = p(x_n,t_n), \tag{1.11}$$

where $p(A|B)$ is the probability of A happening in the given condition B. The Markov process depends only on the latest value of random variable in earlier state and its conditional PDF reads

$$p(x_n,t_n|x_{n-1},t_{n-1};...;x_1,t_1) = p(x_n,t_n|x_{n-1},t_{n-1}). \tag{1.12}$$

The general process depends on more than the current state and its conditional PDF can not be simplified. Following the Bayes' rule, general conditional PDF can be expressed as

$$p(x_n,t_n|x_{n-1},t_{n-1};...;x_1,t_1) = \frac{p(x_n,t_n;...;x_1,t_1)}{p(x_{n-1},t_{n-1};...;x_1,t_1)} \tag{1.13}$$

with $t_n > t_{n-1} > ... > t_1$.

The application of a particular class of stochastic processes depends on the type and behavior of the process to be described. Here, the discussion would be limited to stochastic processes, which best describe the system under investigation. As discussed earlier, the atmospheric wind is highly turbulent and intermittent, thus, contributes highly dynamic forces on the interacting structures or devices such as wind turbines. The behavior of such highly dynamic forces can be described by the class of stochastic processes such as nonlinear Langevin processes, expressed by the stochastic differential equation [96]

$$\frac{dx(t)}{dt} = D^{(1)}(x) + \sqrt{D^{(2)}(x)}\,\Gamma(t). \tag{1.14}$$

Here $D^{(1)}(x)$ is the deterministic part, also termed as drift function and $\sqrt{D^{(2)}(x)}\,\Gamma(t)$ the stochastic part, which is multiple of the square root of the diffusion function $D^{(2)}(x)$ and the Langevin force $\Gamma(t)$.

The Langevin force $\Gamma(t)$ drives the random fluctuations and diffusion function $D^{(2)}(x)$ fixes the amplitude of stochastic fluctuations. The Langevin force $\Gamma(t)$ is a Gaussian white noise with mean $\langle\Gamma(t)\rangle = 0$ and variance $\langle\Gamma^2(t)\rangle = 2$. The statistical properties of the Gaussian white noise are shown in Figure 1.16.

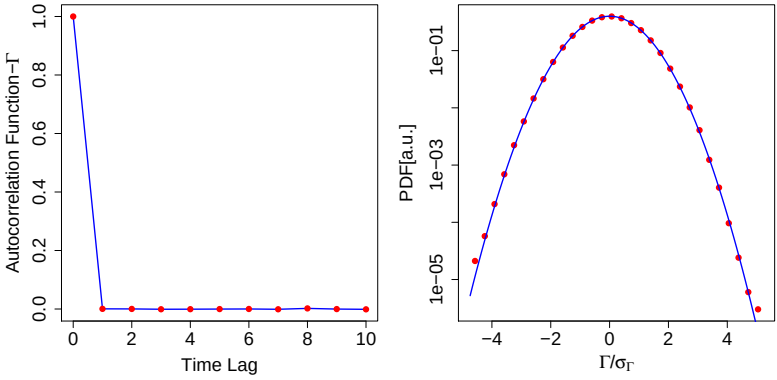

(a) (b)

Figure 1.16: Properties of the Gaussian white (δ-correlated) noise. (a) Autocorrelation function and (b) Gaussian PDF normalized with standard deviation.

Although, the Langevin process described here, is in one-dimensional embedding, the approach can be applied in high dimensional embedding straightforward; see Section 2.2.2.

The Langevin process equation (1.14) because of its random characteristics of the Langevin force, can initiate different values at different realizations, and could be time consuming to obtain the stable values. As an alternate, the probability density of stochastic variable can be estimated using Fokker-Plank or Kolmogorov equation, which for a given set of drift and diffusion functions provides a unique solution. The expression reads [96]

$$\frac{\partial}{\partial t}p(x,t) = \left[-\frac{\partial}{\partial x}D^{(1)}(x) + \frac{1}{2}\frac{\partial^2}{\partial x^2}D^{(2)}(x)\right]p(x,t), \tag{1.15}$$

where the drift $D^{(1)}(x)$ and diffusion $D^{(2)}(x)$ functions can be reconstructed

directly from measured data [97, 98]. These are the first two Kramers-Moyal expansion coefficients, which can be derived as [99]

$$D^{(n)}(x)_{n=1,2} = \frac{1}{n!}\lim_{\tau\to 0}\frac{1}{\tau}M^{(n)}(x,\tau), \tag{1.16}$$

$$M^{(n)}(x,\tau)_{n=1,2} = \langle (x(t+\tau)-x(t))^n\rangle|_{x(t)=x}, \tag{1.17}$$

where $M^{(1)}(x,\tau)$ and $M^{(2)}(x,\tau)$ are the first and second conditional moments, respectively.

The process described by the Langevin equation (1.14) is a Markov process with a Gaussian distributed white noise [96]. For a Markov process, it is essential to fulfil the conditional PDF criteria described by equation (1.12). The Markovian property is destroyed, when stochastic force $\Gamma(t)$ in process given by equation (1.14) is no longer δ-correlated [96]. Such processes are termed as non-Markovian processes and their analysis is limited to deterministic part of the process dynamics [99].

The Langevin equation (1.14) applies to continuous processes, while the observed time series are described by the finite sampling rates. Therefore, the Langevin equation (1.14) has to be reduced to discrete form (Itô sense), which reads [93, 99]

$$x(t+\tau) = x(t) + \tau D^{(1)}(x) + \sqrt{\tau D^{(2)}(x)}\,\Gamma'(t), \tag{1.18}$$

where $\Gamma'(t)$ is the fluctuating quantity corresponding to independent Gaussian distribution with zero mean and variance 2; as described earlier. The process dynamics described by equation (1.18) can be illustrated as shown in Figure 1.17.

The equation (1.16) for an ideal time series with a sufficient temporal resolution, may reconstruct the process dynamics accurately [99]; however, for a real time series, where sampling frequency might be too small, the estimations through (1.16) may suffer from finite sampling rates[3] [99, 100, 101]. In this case, for corresponding corrections, the conditional moments given by equation (1.17), can be replaced with finite-τ approximations as [99, 102]

$$M^{(1)}(x,\tau) \approx \tau D^{(1)}(x), \tag{1.19}$$

$$M^{(2)}(x,\tau) \approx 2\tau D^{(2)}(x) + \tau^2 (D^{(1)}(x))^2. \tag{1.20}$$

The conditional moments are derived from Fokker-Plank equation up to a specified order of τ. For further details; see Gottschall and Peinke [99] and Friedrich *et al.* [102].

[3] i.e. information on smaller time scales may be disregarded [99].

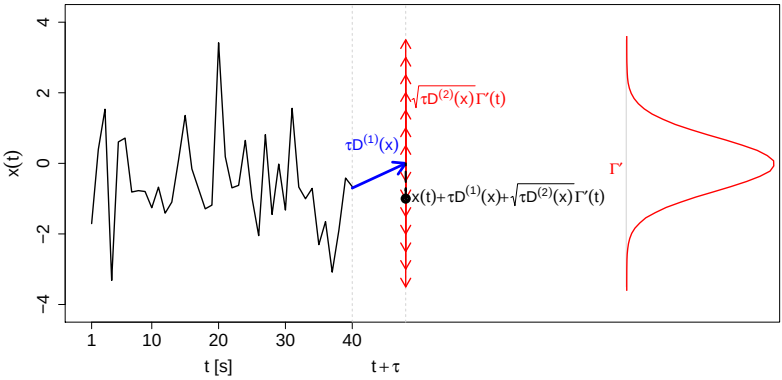

Figure 1.17: Example showing the process dynamics reconstructed by the Langevin approach in discrete form. Blue arrow denotes the dynamics of deterministic part and red arrows with Gaussian white noise represent the dynamics of stochastic part. Solid black circle represents one realization x at time $t+\tau$.

Similar effects can also be observed in the estimations through equation (1.16) in the presence of external measurement noise superimposed on the time series [99, 103]. The measurement noise is either already present in some complex systems or generated by the complex system itself or given by the measuring process, and corresponds to an inevitable experimental condition. In this case, instead of $x(t)$, the process can be observed as [103]

$$y(t) = x(t) + \sigma\zeta(t), \tag{1.21}$$

where term $\sigma\zeta(t)$ refers to a superimposed Gaussian distributed noise with $\langle\zeta(t)\rangle = 0$ and $\langle\zeta(t_1)\zeta(t_2)\rangle = \delta(t_1 - t_2)$, and σ the amplitude of noise. In this condition, it is essential to quantify $\sigma\zeta(t)$ and its impact on the reconstruction of coefficients given by equation (1.17).

1.6 Aims and objectives

The increasing size of wind turbines require increased consideration to design issues. The larger the turbine size, the larger the aerodynamic loads. To ensure the structural integrity of wind energy converters (WECs), comprehensive analysis of loads is necessary. The existing load analysis tools given in Section 1.3.3, which are mostly based on engineering and CFD techniques, still have several shortcomings in different forms. For exam-

ple, CFD is still expensive and time consuming, engineering methods still use traditional static lookup tables for airfoil characteristics to quantify the loads on blades.

In comparison to CFD, engineering methods are in excessive practice, being inexpensive and efficient in computational terms. The engineering methods use aerodynamic packages such as AeroDyn that by employing classical BEM or dynamic stall models provide incomplete information on the blade loads, thereby neglecting the local force fluctuations. The main reason behind this limitation is the reliance of such models on tabulated static airfoil data. The traditional Beddoes-Leishman's dynamic stall model being partially dependent on latter approach, contributes some limited dynamical load information. In this study we focus on the local aerodynamic forces at the rotor blade, which stem from direct interaction of the wind field with the WEC.

The main objectives of this thesis include the proper description and characterization of the lift and drag dynamics under turbulent wind inflow conditions, particularly at high-frequency. The goal is to model the dynamic lift and drag response for an airfoil exposed to unsteady wind inflow using a stochastic approach described in Section 1.5. The model aims to replace the traditional static table lookup approach used by aerodynamic models to achieve the forces on blades with additional loading information in shape of local force dynamics. This could provide an advance approach to enhance the dynamic load models for wind turbine design improvement.

Bibliography

[1] V. Fthenakis, H. C. Kimb. Land use and electricity generation: A life-cycle analysis. *Renewable and Sustainable Energy Reviews*, 13: 465–1474, 2009.

[2] *The World Wind Energy Association half-year report 2012*. World Wind Energy Association-WWEA, 2012.

[3] *Global wind report-Annual market update 2012*. Technical report, Global Wind Energy Council, Brussels, Belgium, April 2013.

[4] P. J. Schubel and R. J. Crossley. Review: Wind Turbine Blade Design. *Energies*, 5:3425–3449, 2012.

[5] *Wind Power Development*. Available online: http://www.telosnet.com/wind, accessed on 24 May 2013.

[6] *Windside*. Available online: http://www.windside.com/, accessed on 27 May 2013.

[7] *Wind turbines*. Available online: http://www.englishecoenergy.com/, accessed on 27 June 2013.

[8] D. G. Hull. *Fundamentals of Airplane Flight Mechanics*. Springer, Berlin, Germany, 2007.

[9] T. Ackermann and L. Söder. An overview of wind energy-status 2002. *Renewable and Sustainable Energy Reviews*, 6:67–128, 2002.

[10] D. Fink. *Small wind turbine basics*. Energy self sufficiency newsletter part 2, August 2005.

[11] R. Dominy, P. Lunt, A. Bickerdyke and J. Dominy. Self-starting capability of a darrieus turbine. *Proceedings of the IMechE part A: Journal of power and energy*, 221:111–120, 2007.

[12] M. M. Duquette and K. D. Visser. Numerical implications of solidity and blade number on rotor performance of horizontal-axis wind turbines. *Journal of Solar Energy Engineering, Transactions ASME*, 125:425–432, 2003.

[13] E. Hau. *Wind Turbines: Fundamentals, Technologies, Application, Economics*. Springer, Berlin, Germany, 2006.

[14] T. Burton, D. Sharpe, N. Jenkins and E. Bossanyi. *Wind Energy Handbook, Second Edition*. John Wiley & Sons, Chichester, UK, 2011.

[15] *Technical Application Papers No. 13 Wind power plants*. ABB, 2011.

[16] R. Gasch and J. Twele. *Wind Power Plants*. Solarpraxis, Berlin, Germany, 2002.

[17] A. N. Gorban, A. M. Gorlov and V. M. Silantyev. Limits of the turbine efficiency for free fluid flow. *Journal of Energy Resources Technology, Transactions of the ASME*, 123:311–317, 2001.

[18] M. A. Yurdusev, R. Ata and N. S. Cetin. Assessment of optimum tip speed ratio in wind turbines using artificial neural networks. *Energy*, 31:2153–2161, 2006.

[19] L. J. Vermeer, J. N. Sørensen and A. Crespo. Wind turbine wake aerodynamics. *Progress in Aerospace Sciences*, 39:467–510, August–October 2003.

[20] *Wind turbines airfoil aerodynamics*. Available online: http://science.howstuffworks.com/environmental/green-science/wind-power3.htm, accessed on 13 June 2013.

[21] M. Kühn. *Rotor Aerodynamics and Blade Element Momentum Theory*. Advanced Wind Energy Technology lecture notes, Carl von Ossietzky University of Oldenburg, 2013

[22] K. Kishinami, H. Taniguchi, J. Suzuki, H. Ibano, T. Kazunou and M. Turuhami. Theoretical and experimental study on the aerodynamic characteristics of a horizontal axis wind turbine. *Energy*, 30:2089–2100, August–September 2005.

[23] K. Y. Maalawi and M. A. Badr. A practical approach for selecting optimum wind rotors. *Renewable Energy*, 28:803–822, 2003.

[24] R. T. Griffiths. The effect of aerofoil characteristics on windmill performance. *Aeronautical Journal*, 81:322–326, 1977.

[25] R. P. J. O. M. van Rooij and W. A. Timmer. Roughness sensitivity considerations for thick rotor blade airfoils. *Journal of Solar Energy Engineering, Transactions ASME*, 125:468–478, 2003.

[26] P. Fuglsang and C. Bak. Development of the Risø wind turbine airfoils. *Wind Energy*, 7:145–162, 2004.

[27] C. Kong, J. Bang and Y. Sugiyama. Structural investigation of composite wind turbine blade considering various load cases and fatigue life. *Energy*, 30:2101–2114, 2005.

[28] J. J. Chattot. Optimization of wind turbines using helicoidal vortex model. *Journal of Solar Energy Engineering, Transactions ASME*, 125:418–424, 2003.

[29] P. Fuglsang and H. A. Madsen. Optimization method for wind turbine rotors. *Journal of Wind Energy Engineering and Industrial Aerodynamics*, 80:191–206, 1999.

[30] M. Jureczko, M. Pawlak and A. Mezyk. Optimization of wind turbine blades. *Journal of Materials Processing Technology*, 167:463–471, 2005.

[31] R. Gasch, J. Maurer and C. Heilmann. *Blade Geometry. Wind Power Plants (Fundamentals, Design, Construction and Operation), Second Edition*. Springer, Berlin, Germany, 2012.

[32] M. Hölling. *Wind-blade interaction*. PPRE, Wind Energy-I lecture notes, Carl von Ossietzky University of Oldenburg, 2013.

[33] *Wind turbine blade aerodynamics*. Available online: http://www.gurit.com/, accessed on 01 July 2013.

[34] T. K. Barlas and G. A. M. van Kuik. Review of state of the art in smart rotor control research for wind turbines. *Progress in Aerospace Sciences*, 46:1–27, 2010.

[35] *Smart Blade*. Available online: http://smart-blade.com/, accessed on 05 July 2014.

[36] *AdVanced Aerodynaic Tools for lArge Rotors (AVATAR)*. Available online: http://www.eera-avatar.eu/home/, accessed on 05 July 2014.

[37] T. Barlas. *Smart rotor blades and rotor control for wind turbines*. UpWind project report, Delft University Wind Energy Research Institute (DUWIND), the Netherlands, 2007.

[38] B. Marrant. *Smart Dynamic Rotor Control for Large Offshore Wind Turbines*. PhD research project (on going), Delft University of Technology, Faculty of Aerospace Engineering, the Netherlands, 2014.

[39] T. Barlas and M. Lackner. The Application of Smart Structures for Large Wind Turbine Rotor Blades. *Proceedings of the 50th IEA Topical Expert Meeting*, Delft University of Technology, the Netherlands, 2006.

[40] S. Thor. The Application of Smart Structures for Large Wind Turbine Rotor Blades. *Proceedings of the 56th IEA Topical Expert Meeting*, Sandia National Labs, USA, 2008.

[41] G. Pechlivanoglou. *Passive and active flow control solutions for wind turbine blades*. PhD thesis, Technical University of Berlin, Germany, 2013.

[42] J. G. Leishman. Challenges in modeling the unsteady aerodynamics of wind turbines. *Wind Energy*, 5:85–132, 2002.

[43] H. Shel. Review of the Present Status of Rotor Aerodynamics. *Wind Energy*, 1:46–69,1998.

[44] A. T. Conlisk. Modern Helicopter Rotor Aerodynamics. *Progress in Aerospace Sciences*, 37:419–476, 2001.

[45] G. .J. W. van Bussel. *The Aerodynamics of Horizontal Axis Wind Turbine Rotors Explored with Asymptotic Expansion Methods*. PhD thesis, Delft University of Technology, the Netherlands, 1995.

[46] T. Sant. *Improving BEM-Based Aerodynamic Models in Wind Turbine Design Codes*. PhD thesis, Delft University Wind Energy Research Institute (DUWIND), the Netherlands, 2007.

[47] B. Montgomerie and S. E. Thor. Aerodynamics for Wind Turbines. *Summary of IEA R&D Wind -16th Joint Action Symposium*, Boulder USA, May 2003.

[48] J. Sumner, C. S. Watters, and C. Masson. CFD in Wind Energy: The Virtual Multiscale Wind Tunnel. *Energies*, 3:989–1013, 2010.

[49] K. Åhlund. *Investigation of the NREL NASA/Ames Wind Turbine Aerodynamics Database*. Scientific report FOI-Rñ1243ñSE, Swedish Defence Research Agency, Stockholm, Sweden, June 2004.

[50] C. E. Lynch. *Advanced CFD methods for wind turbine analysis*. PhD thesis, School of Aerospace Engineering, Georgia Institute of Technology, USA, 2011.

[51] M. O. .L. Hansen and H. A. Madsen. Review Paper on Wind Turbine Aerodynamics. *Journal of Fluids Engineering*, 133:114001, 2011.

[52] P. J. Moriarty and A. C. Hansen. *AeroDyn Theory Manual*. Technical report NREL/EL-500-36881, National Renewable Energy Laboratory, Golden, Colorado, USA, January 2005.

[53] J. M. Jonkman and M. L. Buhl Jr. *FAST User's Guide*. Technical report NREL/EL-500-38230, National Renewable Energy Laboratory, Golden, Colorado, USA, August 2005.

[54] D. J. Laino and A. C. Hansen. *User's Guide to the Computer Software Routines AeroDyn Interface for ADAMS*. Technical report prepared for NREL under subcontract No. TCX-9-29209-0, University of Utah, Salt Lake City, USA, September 2001.

[55] S. Mulski. SIMPACK Multi-Body Simulation. *Wind and Drivetrain Conference*, SIMPACK AG, Hamburg, Germany, September 2012.

[56] A. C. Hansen and D. J. Laino. *USER'S GUIDE to the Wind Turbine Dynamics Computer Programs YawDyn and AeroDyn for ADAMS*. Technical report XAF-4-14076-02, University of Utah, Salt Lake City, USA, August 1998.

[57] M. L. Buhl Jr. and A. Manjock. *A Comparison of Wind Turbine Aeroelastic Codes Used for Certification*. Conference paper NREL/CP-500-39113, National Renewable Energy Laboratory, Golden, Colorado, USA, January 2006.

[58] M. Kühn. *Dynamics and Design Optimization of Offshore Wind Energy Conversion Systems*. PhD thesis, Delft University Wind Energy Research Institute (DUWIND), the Netherlands, 2001.

[59] S. Øye. *FLEX5 User Manual*. Technical report, Danske Techniske Hogskole, 1999.

[60] GL. Garrad Hassan. *Wind Turbine Design Software*. Available online: http://www.gl-garradhassan.com/en/Software.php, accessed on 30 May 2013.

[61] V. A. Vasilis and S. G. Voutsinas. A General Aerodynamic and Structural Prediction Tool for Wind Turbines. *European union wind energy conference*, Dublin, Ireland, 1997.

[62] T. J. Larsen and A. M. Hansen. *How 2 HAWC2, the user's manual*. Technical report ISSN 0106-2840, Risø National Laboratory, Denmark, December 2007.

[63] B. Visser. The aeroelastic code FLEXLAST. *State of the Art of Aeroelastic Codes for Wind Turbine Calculations 28th meeting of experts*, 161–166, Lyngby, Denmark, 1996.

[64] C. Lindenburg. *PHATAS Release "NOV-2003" and "APR-2005" USER'S MANUAL*. Technical report ECN-I–05-005, Energy Research Centre of the Netherlands, May 2005.

[65] H. Ganander and B. Olsson. *VIDYN simuleringsprogram för horisontalaxlade vindkraftverk*. Technical report TG-R-98-14, Teknikgruppen AB, 1998.

[66] A. Björck. *AERFORCE: Subroutine package for unsteady Blade Element Momentum calculations*. Technical report FFA TN 2000-07, Aeronautical Research Institute of Sweden, 2000.

[67] K. W. McAlister, O. Lambert and D. Petot. *Application of the ONERA model of dynamic stall*. Technical report NASA TR 84-A-3, National Aeronautics and Space Administration, 1984.

[68] A. Björck. *DYNSTALL: Subroutine package with a dynamic stall model*. Technical report FFAP-V-110, Aeronautical Research Institute of Sweden, 2000.

[69] H. Snel. Heuristic modelling of dynamic stall characteristics. *European Wind Energy conference*, 429–433, Dublin Castle, Ireland, 1997.

[70] T. G. van Engelen and H. Braam. *TURBU Offshore, computer program for frequency domain analysis of horizontal axis offshore wind turbines*. Technical report ECN-C–04-079, Energy Research Centre of the Netherlands, September 2004.

[71] P. Passon and M. Kühn. State-of-the-art and Development Needs of Simulation Codes for Offshore Wind Turbines. *Offshore Conference*, Copenhagen, 2005.

[72] A. Ahlström. *Aeroelastic simulation of wind turbine dynamics*. PhD thesis, department of mechanics, KTH, Stockholm, Sweden, 2005.

[73] J. Johansen, H. A. Madsen, M. Gaunaa and C. Bak. Design of a Wind Turbine Rotor for Maximum Aerodynamic Efficiency. *Wind Energy*, 12:261–273, 2009.

[74] B. Dalpé and C. Masson. Numerical Study of Fully Developed Turbulent Flow Within and Above a Dense Forest. *Wind Energy*, 11: 503–515, 2008.

[75] F. D. Bianchi, H. D. Battista and R. J. Mantz. *Wind Turbine Control Systems - Principles, Modelling and Gain Scheduling Design*. Springer, London, UK, 2007.

[76] C. Sicot, P. Devinant, T. Laverne, S. Loyer and J. Hureau. Experimental Study of the Effect of Turbulence on Horizontal Axis Wind Turbine Aerodynamics. *Wind Energy*, 9:361–370, 2006.

[77] B. Sanderse, S. P. van der Pijl and B. Koren. Review of computational fluid dynamics for wind turbine wake aerodynamics. *Wind Energy*, 14:799–819, 2011.

[78] T. Mücke, D. Kleinhans and J. Peinke. Atmospheric turbulence and its influence on the alternating loads on wind turbines. *Wind Energy*, 14:301–316, 2011.

[79] W. Medjroubi. *Numerical Simulation of Dynamic Stall for Heaving Airfoils Using Adaptive Mesh Techniques*. PhD thesis, University of Oldenburg, Germany, 2011.

[80] E. Giacomazzi, C. Bruno and B. Favini. Fractal modelling of turbulent mixing. *Combustion Theory and Modelling*, 3:637–655, 1999.

[81] A. D. Staicu. *Intermittency and turbulence*. PhD thesis, University of Technology Eindhoven, 2002.

[82] M. Wächter, H. Heißelmann, M. Hölling, A. Morales, P. Milan, T. Mücke, J. Peinke, N. Reinke and P. Rinn. The Turbulent Nature of the Atmospheric Boundary Layer and its Impact on the Wind Energy Conversion Process. *Journal of Turbulence*, 13, 2012.

[83] B. S. Kallesøe. A low-order model for analyzing effects of blade fatigue load control. *Wind Energy*, 9:421–436, 2006.

[84] T. Sebastian and M. A. Lackner. Characterization of the unsteady aerodynamics of offshore floating wind turbines. *Wind Energy*, 16: 339–352, 2013.

[85] K. Saranyasoontorn and L. Manuel. On the propagation of uncertainty in inflow turbulence to wind turbine loads. *Wind Engineering and Industrial Aerodynamics*, 96:503–523, 2008.

[86] N. Sezer-Uzol and O. Uzol. Effect of steady and transient wind shear on the wake structure and performance of a horizontal axis wind turbine rotor. *Wind Energy*, 16:1–17, 2013.

[87] J. G. Leishman. *Principles of Helicopter Aerodynamics, Second Edition*. Cambridge University Press, Cambridge, New York, USA, 2006.

[88] D. M. Eggleston and F. S. Stoddard. *Wind turbine engineering design*. Van Nostrand Reinhold Company, New York, USA, July 1987.

[89] J. G. Holierhoek, J. B. deVaal, A. H. van Zuijlen and H. Bijl. Comparing different dynamic stall models. *Wind Energy*, 16:139–158, 2013.

[90] G. Wolken-Möhlmann, P. Knebel, S. Barth and J. Peinke. Dynamic lift measurements on a FX79W151A airfoil via pressure distribution on the wind tunnel walls. *Journal of Physics: Conference Series*, 75: 012026, 2007.

[91] H. Snel. Review of Aerodynamics for Wind Turbines. *Wind Energy*, 6:203–211, 2003.

[92] D. A. Sepra. *Wind Turbine Technology*. The American Society of Mechanical Engineers, 215–282, New York, 1994.

[93] R. Friedrich, J. Peinke, M. Sahimi and M. R. R. Tabar. Approaching complexity by stochastic methods: From biological systems to turbulence. *Physics Reports*, 506:87–162, 2011.

[94] H. Haken. *Information and self-organization - A macroscopic approach to complex systems, Third Edition*. Springer, Berlin, Germany, 2010.

[95] C. Honisch and R. Friedrich. Estimation of Kramers-Moyal coefficients at low sampling rates. *Physical Review E*, 83:066701, 2011.

[96] H. Risken. *The Fokker-Planck Equation, Second Edition*. Springer, Berlin, Germany, 1996.

[97] S. Siegert, R. Friedricha and J. Peinke. Analysis of data sets of stochastic systems *Physics Letters A*, 243:275-280, 1998.

[98] R. Friedrich and J. Peinke. Description of a Turbulent Cascade by a Fokker-Planck Equation *Physical Review Letters*, 78:863-866, 1997.

[99] J. Gottschall and J. Peinke. On the definition and handling of different drift and diffusion estimates. *New Journal of Physics*, 10:083034, 2008.

[100] M. Ragwitz and H. Kantz. Indispensible finite time corrections for Fokker-Planck equations from time series data. *Physical Review Letters*, 87:254501, 2001.

[101] P. Sura and J. Barsugli. A note on estimating drift and diffusion parameters from time series. *Physics Letters A*, 305:304-311, 2002.

[102] R. Friedrich, C. Renner, M. Siefert and J. Peinke. Comment on Indispensable Finite Time Corrections for Fokker-Planck Equations from Time Series Data. *Physical Review Letters*, 89:149401, 2002.

[103] F. Böttcher, J. Peinke, D. Kleinhans, R. Friedrich, P. G. Lind and M. Haase. Reconstruction of Complex Dynamical Systems Affected by Strong Measurement Noise. *Physical Review Letters*, 97:090603, 2006.

Chapter 2

Stochastic modeling of lift and drag dynamics

The content presented in this chapter is published as "M. R. LUHUR, J. PEINKE, J. SCHNEEMANN and M. WÄCHTER. Stochastic modeling of lift and drag dynamics under turbulent wind inflow conditions, *Wind Energy*, 2014. doi: 10.1002/we.1699". Here, Figure 2.1 in Section 2.2.1 and Figure 2.5 in Section 2.2.4 are added for more information to the reader on airfoil geometry and easy understanding of model optimization scheme, respectively. Footnote 1 is also appended for same reason. These are not included in the original publication.

Abstract We present a new approach to model the complex dynamics of aerodynamic forces on an airfoil in turbulent inflow conditions. Our ansatz is based on stochastic differential equations and aims at replacing traditional lookup table methods used in wind turbine simulation systems by the effective response dynamics of lift and drag forces. The parameters of the model are derived directly from empirical data. Measurements were taken in the closed loop wind tunnel of the University of Oldenburg for an airfoil FX 79-W-151A. The turbulent inflow was generated using a fractal square grid as it is possible to generate in this way wind speed fluctuations with similar statistics as observed in nature. Forces were measured using two strain gauge force sensors at two end points of the vertically installed airfoil. The modeling is done by applying a stochastic approach on the measured data. By estimating the first two Kramers-Moyal coefficients, a first-order stochastic differential equation called the Langevin equation is obtained. The stochastic model achieved through this approach is extended to account for oscillation effects contained in lift and drag dynamics that probably stem from unsteady aerodynamic effects. The results are optimized by applying a χ^2 test on the probability density functions (PDFs) of model and measurements. With the knowledge of the Langevin equation synthetic time series are generated. Their stationary PDFs as well as

conditional PDFs show good agreement with the actual measurements. A comparison of classical averaging and the stochastic approach shows that stochastic analysis achieves additional insight into the local dynamics of lift and drag forces.

2.1 Introduction

Wind turbines are permanently exposed to turbulent atmospheric flows with their well-known complex statistics and gusty behavior [1, 2, 3]. Furthermore, they are subjected to ground boundary layer effects [4, 5, 6], directional and spatial variations in wind shear and tower interaction effects [1]. This complex nature of wind fields has great impact on the operation of wind energy converters (WECs) imposing different risks especially in terms of highly dynamic mechanical loads [7, 8]. Namely extreme wind events and the respective loads induced on WECs constitute a major challenge for wind turbine development and optimization. The emergence and propagation of these extreme loads from the wind inflow through rotor aerodynamics, drive train and power electronics is still not fully understood. In this paper, we focus on the local aerodynamic forces at the rotor blade, which stem from direct interaction of the wind field with the WEC, and the characterization and modeling of their dynamics.

Unsteady aerodynamic loads stimulate structural vibrations that can contribute to fatigue problems [9] and fast variations in the angle of attack (AOA) leading to the well-known dynamic stall effect, which can result in substantial enlargement of the lift dynamics; compare the works of Eggleston and Stoddard [10], Leishman [11] and Wolken-Möhlmann *et al.* [12]. Dynamic stall is a viscous effect on the airfoil characteristics in stalled conditions, which encourages transient forces at larger amplitude [13]. These viscous forces create rotating motion of the fluid particles (vortices) on the blade surfaces during the flow separation [14]. Additional to dynamic stall situations, pronounced unsteady aerodynamic forces can also be generated in fully attached flow on the lifting surfaces in unsteady inflow [1]. These effects are exhibited as amplitude and phase variations in the aerodynamic forces compared to quasi-steady conditions. In addition, the flow compressibility has also potential effects on unsteady aerodynamic forces in terms of amplitude and phase effects compared to incompressible flow [1]. Several studies exist on lift and drag forces at airfoils in steady low-turbulence inflow [15, 16, 17], but the complexity of turbulent inflow experienced in open-air applications is yet to be comprehended fully. To understand these complex flows and integrate the corresponding effects into a wind turbine design is one of the major challenges in current wind energy research and

engineering.

To model the aerodynamic loads on wind turbine rotors, various mathematical models exist which include blade element momentum (BEM) methods, free wake vortex methods, acceleration potential methods and computational fluid dynamics (CFD) techniques [1, 18, 19, 20, 21]. Recently, a stochastic approach has been reported to model the unsteady effects at static stall stemming from the self-induced turbulent wake of an airfoil [22]. The aerodynamic forces can be calculated by either CFD or engineering methods, which, from a performance point of view, are the methods of choice [23]. While some examples of very good agreements with experiments have been published during the last years in particular for simple inflow and stiff rotors [9], CFD computations are still excessively expensive and time consuming [24]. For CFD to include more effects and reduce computational time, even more powerful computer systems are required. Thus, most computational studies of wind turbine aerodynamics still continue using the classical BEM theory because of its simplicity and computational efficiency [9].

To obtain aerodynamic loads, different wind turbine design codes such as FAST [25], YawDyn [26], ADAMS [27], SIMPACK [28], DHAT [29] and FLEX5 [30] use aerodynamic packages such as AeroDyn [31] to obtain distributed loads on the wind turbine blades. AeroDyn uses different models to perform aerodynamic calculations for aeroelastic simulations of horizontal axis wind turbines. These include the BEM wake theory, generalized dynamic wake (GDW) theory, dynamic stall model and the tower shadow model. The BEM wake theory is a well-known classical approach used by different wind turbine designers with various corrections, while the GDW theory is a more advanced approach that is useful especially for modeling skewed and unsteady wake dynamics. The dynamic stall model is based on the semi-empirical Beddoes-Leishman model important for yawed wind turbines. These models accept two types of wind inputs: first, the hub-height wind and second, the full field turbulence, obtained from either measurements or simulations. The hub-height wind contains either steady or time varying wind data, whereas the full field turbulence corresponds to the local wind components changing in time and space. The full field turbulence is created by the TurbSim program [32, 33].

Nevertheless, the approach of AeroDyn and comparable aerodynamic models essentially consists of lookup tables that contain static characteristics for an airfoil at constant AOAs [31, 34]. Even special types of CFD, namely actuator disc and actuator line models, use tabulated airfoil data such as BEM to estimate the aerodynamic loads [9]. In dynamic stall model, the static airfoil coefficients are modified based on the AOA and

its rate of variation. The models in AeroDyn do not consider the local dynamics of lift and drag coefficients and thus lack information on the system dynamics.

In this paper, we propose a new alternative that replaces the traditional table lookup method by a simple stochastic equation that provides the lift and drag forces with complete local dynamics. Moreover, we show that such stochastic equation can be derived from experimental data. Since the concept of this paper is to present the basic features of this approach, we neglect for simplicity additional effects such as tower shadow, vertical wind shear, yawed inflow and aeroelastic effects. The scope of this paper is to derive the dynamic response behavior of lift and drag from the measured time series especially at high frequency and to model these dynamics using a stochastic approach. The future aim is to integrate the model under investigation into an aerodynamic model such as AeroDyn based on the BEM theory, which then could be combined with WEC models such as FAST or other similar models to achieve a stochastic rotor model.

The paper consists of three main sections. First, there is the description of the methodology in Section 2.2 followed by the details of measurements and the modeling approach applied. Then the comparison of model and measurement results is given in Section 2.3. At the end, a conclusion section is added summarizing the outcome and outlook of the work.

2.2 Methodology

The methodology consists of four steps. In the first step, wind tunnel tests have been carried out to obtain the time series of unsteady forces acting on an airfoil under turbulent inflow conditions. The measurements have been taken directly by two force sensors installed on the airfoil. In the second step, from the dynamically observed lift and drag signals, a stochastic equation (Langevin equation [35]) in terms of drift and diffusion functions is reconstructed. The drift and diffusion functions are improved using an inverse parabolic interpolation optimization scheme [36] in connection with a χ^2 test based on model and measurement probability density functions (PDFs) as proposed by Kleinhans *et al.* [37, 38]. Then both optimized functions are inserted into the Langevin equation to define the basic model. In the third step, an extension to the basic model has been introduced to account for oscillation effects (probably caused by unsteady aerodynamics) found in lift and drag time series. Finally in the last step, an overall optimization approach is applied again in form of a χ^2 test based on PDFs of extended model and measurement. The purpose of final optimization was to incorporate the correct amount of additional effects covered in the model

extension. Each step is discussed in the following three sections in detail.

2.2.1 Wind tunnel measurements

The lift and drag force measurements have been taken in the closed loop wind tunnel of the University of Oldenburg on an airfoil FX 79-W-151A having a chord length of 0.2 m. The Wortmann FX 79-W-151A is a cambered airfoil without flaps for use on wind turbines [39, 40]. The geometrical details of FX 79-W-151A are given in Figure 2.1. No turbulator or similar device to force the turbulent transition has been used. The wind

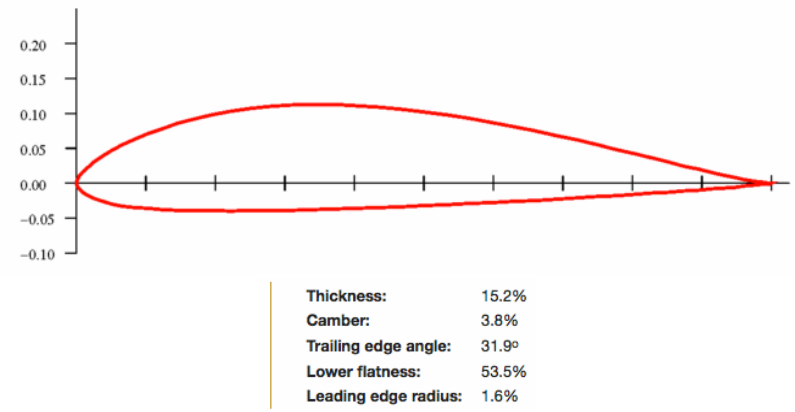

Figure 2.1: Geometrical details of airfoil FX 79-W-151A.

tunnel has a test section of 1 m width, 0.8 m height and 2.6 m length. The forces were measured at a sampling frequency of 1 KHz using two strain gauge force sensors mounted on two ends of the airfoil in span-wise direction as shown in Figure 2.2. The mean wind velocity was approximately 50 m/s leading to a Reynolds number of Re=7x10^5 based on the chord length. The wind tunnel was driven by steady power supply, all fluctuations of the wind velocities are caused by grid.

The turbulent inflow was generated using a fractal square grid as it generates wind speed fluctuations more similar to atmospheric flows than the wind speed fluctuations generated by classical square grids. The comparison of a classical square grid and fractal square grid inflow is shown in Figure 2.3 in terms of statistics of velocity increments $u_\tau = u(t+\tau) - u(t)$. The fractal square grid obeys a fractal square geometry, which generates intermittent inflows, i.e. the statistics of velocity increments show pronounced heavy tails, thus deviating from Gaussian statistics, for time lags

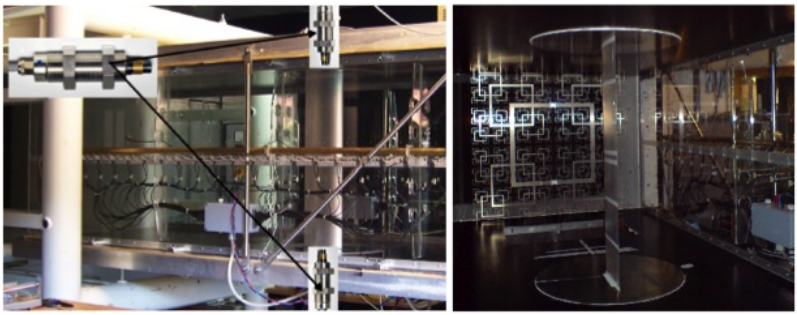

(a) (b)

Figure 2.2: View of the wind tunnel test section. (a) The position of the force sensors installed on the end points of the vertically mounted airfoil in the test section. (b) The position of the fractal square grid installed in front of the wind tunnel nozzle.

up to $\tau = 10$ s [42, 43] as shown in Figure 2.3(b). The classical square grid produces intermittent inflows for smaller time lags, but the PDFs converge to a Gaussian distribution for higher time lags (Figure 2.3(a)). The atmospheric turbulence is known to be intermittent even at much higher time lags [44] than 10 s.

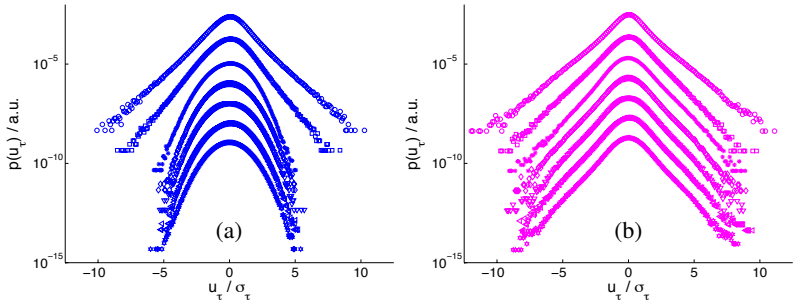

Figure 2.3: Normalized velocity increment PDFs for time lags $\tau = (0.033, 0.1, 1, 10, 10^2, 10^3, 10^4)$ ms in increasing sequence from top to bottom. The PDFs are shifted vertically for clarity. The PDFs are given in arbitrary units (a.u.). (a) 5 cm square grid, mean velocity = 42 m/s and (b) fractal square grid, mean velocity = 48 m/s [41].

It is worth to note that in recent years, the investigations made on wind tunnel generated turbulence using multi-scale grids by Krogstad and Davidson [45, 46] lead to controversial findings compared to multi-scale exper-

iments performed by Hurst and Vassilicos [47]. The main debatable findings reported by Hurst and Vassilicos [47] include the production of fully developed homogeneous turbulence without distinguishing between near and far fields behind the grids and the exponential decay of energy in case of the fractal square grid. Nevertheless, the investigations made by George and Wang [48] and Oberlack and Khujadze [49, 50] proposed the model of homogenous turbulence with exponential decay of energy for the fractal square grid as observed by Hurst and Vassilicos [47]. Moreover, the study of Krogstad and Davidson [45, 46] did not include the same class of fractal square grid, which is used for present measurements.

For our investigations, the fractal square grid has the nice property to generate intermittent turbulent fluctuations on many length scales even for steady operating conditions of the wind tunnel. In particular, the turbulent flow generated by the fractal square grid is an efficient method to generate small-scale wind statistics [41, 44, 47, 51, 52] similar to those observed in nature. In our case, the turbulence intensity generated with fractal square grid was 4.6% obtained by using the relation

$$T_i = \frac{\sigma_u}{\langle u \rangle}, \tag{2.1}$$

where T_i is the turbulence intensity, σ_u the standard deviation of the wind speed and $\langle u \rangle$ the mean wind speed. Further details of the measurement can be found in work of Schneemann *et al.* [41], and information on the Strouhal number as an additional parameter is given in Section 2.3.2. The dynamics of the generated forces at an airfoil are typically in the range of the flow-over time (chord length/wind speed), which is, for our flow conditions, around a few milliseconds, for a real wind turbine is in the range of 0.1 s. In Figure 2.3, it is shown that for the time of millisecond scales, the velocity fluctuations measured as corresponding increments become quite Gaussian for a classical grid, where for the fractal square grid, we find the desired pronounced intermittent behavior.

The installed force sensors offer two measuring axes, the X-axis and Y-axis (Figure 2.4) [53]. Thus, the acting force can be decomposed into X and Y components. Here, the sensors measure the forces perpendicular and parallel to the wind inflow. The perpendicular forces represent the lift force, whereas the parallel forces represent the drag force. From measured forces, the lift and drag coefficients are calculated as follows [41, 54]:

$$C_L = \frac{F_L}{qA}, \tag{2.2}$$

$$C_D = \frac{F_D}{qA}, \tag{2.3}$$

where F_L is the lift force, F_D the drag force, A the area of the airfoil and q the inflow dynamic pressure measured in the pre-chamber (before the grid). The dynamic pressure varies with respect to time, most likely due to periodic separation and blockage effects.

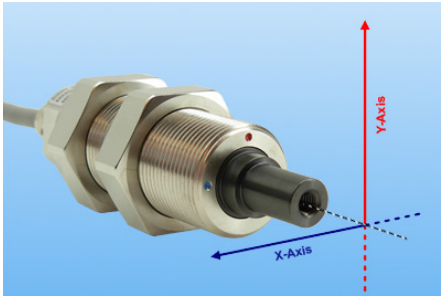

Figure 2.4: Illustration of the force sensor measuring axes indicated by red and blue dots (color online). The measuring axes are perpendicular to each other [53].

The calibration of the force sensors for the current measurements was performed via balances. However, the same sensors were calibrated by Schneemann *et al.* [41] by comparing mean lift data achieved through force measurements with mean lift data obtained through wind tunnel wall pressure measurements. In addition, the mean lift curves from wind tunnel wall pressure measurements and force measurements at the airfoil were compared with reference data provided by Althaus [55], which also showed good correspondence [41].

2.2.2 Stochastic modeling of lift and drag dynamics

Since the wind is highly dynamic by nature, the resulting lift and drag forces are dynamic in nature, too. The commonly used standard approach is based on averaging procedure with standard deviations resulting in static lift and drag curves, which neglects much information about the real dynamics of the system. A stochastic approach is proposed not only for modeling but also to access and extract most of the information available in the lift and drag dynamics in terms of a dynamic response model. The approach is applied in one-dimensional and two-dimensional embedding.

One-dimensional modeling approach

The approach is based on the Langevin process used to model the complex statistics by means of stochastic dynamics. The Langevin equation, cf.

to the work of Risken [35], is a first-order stochastic differential equation based on drift and diffusion functions coupled with a noise term.

$$\frac{dX(t)}{dt} = D^{(1)}(X) + \sqrt{D^{(2)}(X)}\,\Gamma(t), \tag{2.4}$$

where $\Gamma(t)$ is a Gaussian white noise termed as Langevin force [35] with mean value $\langle\Gamma(t)\rangle = 0$ and variance $\langle\Gamma^2(t)\rangle = 2$. Since the statistics of the turbulence, i.e. the PDF of the turbulent wind fluctuations $u'(t) = u(t) - \langle u\rangle$ is Gaussian but correlated, it can be approximated only roughly by Langevin noise. On the other hand, only few time scales interact dynamically (in a non- equilibrium sense) with the airfoil. We therefore expect only a short time scale window of dynamic turbulence airfoil interaction, which we approximate by Langevin noise. Also, this approach has been successfully applied to a number of turbulence-driven systems; see Friedrich *et al.* [56]. If, in a statistical sense, higher-order effects are of interest, the Langevin noise $\Gamma(t)$ can be replaced by noisy time series having the fine structures of turbulence, such as multifractal time series.

The $D^{(1)}(X)$ and $D^{(2)}(X)$ are the drift and diffusion functions, also known as first and second Kramers-Moyal coefficients for $X(t)$, which can be estimated from actual measured signal using the relation [57, 58, 59]

$$D^{(n)}(X,\alpha) = \lim_{\tau\to 0}\frac{1}{n!\,\tau}\langle(X(t+\tau) - X(t))^n\rangle|_{X(t)=X;\alpha}, \tag{2.5}$$

where X denotes the lift and drag coefficients, α the fixed AOA, $n = 1$ for the drift function and $n = 2$ for the diffusion function. To calculate the drift and diffusion functions, the measured lift and drag time series are separated into bins, and equation (2.5) is applied for $X(t) = X$ in each bin. In this way, these two functions can be estimated for lift and drag time series separately for each AOA. Here, we consider the case where the mean AOA α is a slowly varying quantity, besides the fluctuations caused by the turbulent inflow conditions.

The $D^{(1)}(X)$ reflects the deterministic part of the system and estimates the mean change or mean time derivative of $X(t)$ in each bin, whereas $D^{(2)}(X)$ quantifies the amplitude of the stochastic fluctuations. In this way, the Langevin equation models the trajectory of the state variable $X(t)$ with quantified stochastic fluctuations. In equation (2.4), the Langevin equation is defined in its continuous form; however, for the computer routine, it is used in discretized form as

$$X(t+\tau_o) = X(t) + \tau_o D^{(1)}(X(t)) + \sqrt{\tau_o D^{(2)}(X(t))}\,\Gamma(t), \tag{2.6}$$

where τ_o is the integration time step typically taken as $\tau_o = 1/f_s$ [42]. f_s corresponds to the sampling frequency of the actual measurements. Providing any initial value for $X(t)$ between minimum and maximum values of the actual measurements of the dynamics, one can iterate and obtain a new signal from the equation (2.6).

Two-dimensional modeling approach

Besides being applied in the one-dimensional approach, the Langevin approach is applied in two-dimensional embedding also with the aim to find out if it may deliver better results than one-dimensional approach. In this context, the general n-dimensional Langevin equation reads [60, 61]

$$\frac{dX_i(t)}{dt} = D_i^{(1)}(\mathbf{X},t) + \sum_{j=1}^{n} \left[\sqrt{D^{(2)}(\mathbf{X},t)}\right]_{ij} \Gamma_j(t), \quad i = 1,...n \tag{2.7}$$

where $n = 2$ for our case. In this way, here, $\mathbf{X}(t)$ represents the two-dimensional (i.e. lift and drag coefficients) stochastic state variable vector. The same explanations like in one-dimensional Langevin approach apply for drift and diffusion functions. The difference only is, in the two-dimensional embedding, the drift and diffusion functions depend on $\mathbf{X}$. The $\Gamma_j(t)$ is the δ-correlated Gaussian noise. The drift and diffusion functions for equation (2.7) are estimated as the limit of conditional moments [59]

$$D_i^{(1)}(\mathbf{X},\alpha) = \lim_{\tau\to 0} \frac{1}{\tau} \langle X_i(t+\tau) - x_i(t)\rangle|_{X(t)=X;\alpha}, \tag{2.8}$$

$$D_{ij}^{(2)}(\mathbf{X},\alpha) = \frac{1}{2} \lim_{\tau\to 0} \frac{1}{\tau} \langle (X_i(t+\tau) - x_i(t))(X_j(t+\tau) - x_j(t))\rangle|_{X(t)=X;\alpha}. \tag{2.9}$$

The numerical estimation of the condition of the moments is subjected to the approximation of $\mathbf{X}(t)\ \varepsilon\ U(x)$, for a sufficiently small neighborhood U of fixed value x. These conditional moments can be estimated directly from measured data sets in a parameter free way.

Drift and diffusion optimization

In general, results of the direct estimation from equations (2.5), (2.8) and (2.9) may suffer from different sources of errors such as finite sampling and additional measurement noise [58, 62]. In statistical sense, the validity of the results obtained from Langevin equations (2.4) and (2.7) strongly depend on the correct estimation of the drift and diffusion functions. Alternatively, to perform the correct $\lim_{\tau\to 0}$, an optimization approach is applied

to obtain correct drift and diffusion functions, which define the best possible model of the system under investigation [38]. The approach is based on χ^2 test applied in terms of PDFs of both model and measurement

$$\chi^2 = \sum_i \frac{(p_{model,i} - p_{measure,i})^2}{(p_{model,i} + p_{measure,i})}, \tag{2.10}$$

where p_{model} and $p_{measure}$ are the stationary PDFs of model and measurement, respectively. The χ^2 test quantifies the difference between the PDFs of model [i.e. equations (2.4) and (2.7)] and measurement. This provides the information about how good the model and the measurements are close to each other. In one way, it is the direct assessment of model quality, i.e. the lower the χ^2 value, the better the model coincides with actual measurements. To calculate the PDFs of the model, an analytical solution to the Langevin equation, i.e. the stationary solution to the Fokker Planck equation [35], is used here.

$$p_{(X_{model})} = \frac{N}{D^{(2)}_{(X_{model})}} \exp\left[\int^{X_{model}} \frac{D^{(1)}(y)}{D^{(2)}(y)} dy\right], \tag{2.11}$$

where N is a normalization factor. The equation expresses that the model signal is completely defined by the behavior of drift and diffusion functions. Thus, the proper estimation of these functions is crucial to obtain correct model. In order to find out the best drift and diffusion function values in an automatic way, the χ^2 test was coupled with an inverse parabolic interpolation[1] optimization scheme. The algorithm [36] reads

$$x = b - \frac{1}{2}\frac{(b-a)^2[f(b)-f(c)] - (b-c)^2[f(b)-f(a)]}{(b-a)[f(b)-f(c)] - (b-c)[f(b)-f(a)]}, \tag{2.12}$$

where x is the estimated abscissa value of new point, which accounts for diffusion function and its ordinate value accounts for χ^2 value in our case. The a, b and c are the abscissa values of the three randomly selected points, and $f(a)$, $f(b)$ and $f(c)$ are the respective ordinate values of three points along the parabolic line.

The algorithm works in a way that it discards one point after each iteration and decides for a new set of three points for next iteration such as the point with minimum ordinate value is always in the middle of the three points. Hence, it is the minimum ordinate value that decides for which

[1] Although it is a parabolic interpolation, as the aim here is to find an abscissa rather than an ordinate; therefore, in technical terms, the method is called an inverse parabolic interpolation [36].

fourth point is to be discarded. The algorithm continues for several iterations until the best value for x is obtained.

In our case, the abscissa x is the diffusion function and χ^2 the corresponding ordinate value for this, which means algorithm finds out that value of diffusion function where χ^2 is minimum. Thereafter, the algorithm automatically stops functioning as the points coincide with each other.

2.2.3 Extension to basic model

The basic model (in one-dimensional and two-dimensional embedding) described so far shows good matching with the actual measurements in terms of lift and drag coefficient time series as well as the stationary PDFs . However, to gain deeper insight into the underlying process, the conditional PDF $p(X(t+\tau)|X(t))$ has to be considered, as it contains the complete information on the process described by Langevin equations (2.4) and (2.7). In our case, the basic model does not reproduce the conditional PDFs satisfactorily for all time lags τ.

The main challenge was to extend the model for out-of-phase oscillations (out-of-phase in case of lift and drag) with variable periods observed in lift and drag coefficient time series. Moreover, an amplitude modulation of the oscillation (breathing) is also found along the lift and drag coefficient time series; see Figure 2.10. The physical reasons behind the oscillation phase shift and breathing are discussed in Section 2.3.2. Satisfactory results are obtained by the following extension:

$$X_{model}(k) = X_{langevin}(k) + A\sin\left(\frac{2\pi k}{T}\right)\exp\left[\left(\frac{-k'}{k_o}\right)^S\right], \tag{2.13}$$

where $X_{langevin}$ is the result obtained from equation (2.4) or (2.7), A the constant to fix the oscillation amplitude of lift and drag coefficient, k the discrete time variable and T the most dominant oscillation period obtained by computing the autocorrelation function (ACF) of lift and drag coefficient time series. The exponential function in the equation controls the increase and decrease in the oscillation amplitude along the lift and drag time series, where k_o is half the average breathing length occurring along the time series, $k' = (k \mod k_o)$ and S is described as

$$S = \begin{cases} +1, & \text{for } (2n)k_o < k \leq (2n+1)k_o \\ -1, & \text{for } (2n+1)k_o < k \leq 2(n+1)k_o, \end{cases} \tag{2.14}$$

where $n = 0, 1, 2, 3....$

2.2.4 Final model optimization

In order to fix the additional effects into the basic model to obtain the final extended model, an overall optimization approach is applied as shown in flow chart Figure 2.5. This is also based on χ^2 test applied on PDFs of extended model and actual measurements. This optimization is based on modification in optimum diffusion function, constant A and half the breathing length k_o until the minimum χ^2 value is achieved. To check the quality of model results, finally the χ^2 value is compared with the intrinsic standard error estimated as [2]

$$S_{Error} = \sum_i \frac{\sqrt{N_i}}{N_{Total}}, \tag{2.15}$$

where N_i is the number of counts in the i^{th} bin and N_{Total} the size of the sample.

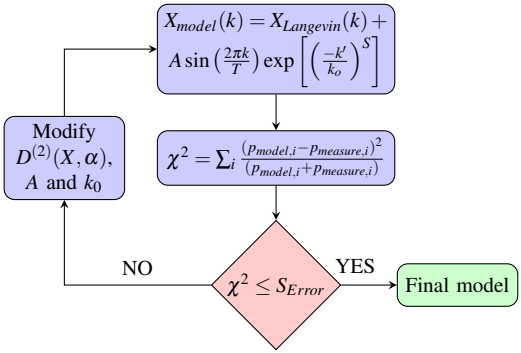

Figure 2.5: Model optimization flow chart.

2.3 Results

2.3.1 Stochastic lift and drag model

Depending on the dynamic behavior of the lift and drag, the stochastic approach as explained in Section 2.2 is applied. As an example, detailed results are presented for two AOAs, 11° and 28°, demonstrating the pre-stall (slightly below stall) and deep stall regimes, respectively; see Figure 2.16. Similar results are obtained for other AOAs also ranging from 0° to 30°.

Drift and diffusion functions

By the one-dimensional Langevin approach, the drift $D^{(1)}(X,\alpha)$ and diffusion $D^{(2)}(X,\alpha)$ functions are estimated using equation (2.5). The approach is applied on $C_{Lmeasure}(t)$ and $C_{Dmeasure}(t)$ time series. In order to avoid errors [58, 62], both functions are optimized through an optimization scheme described in Section 2.2.2.

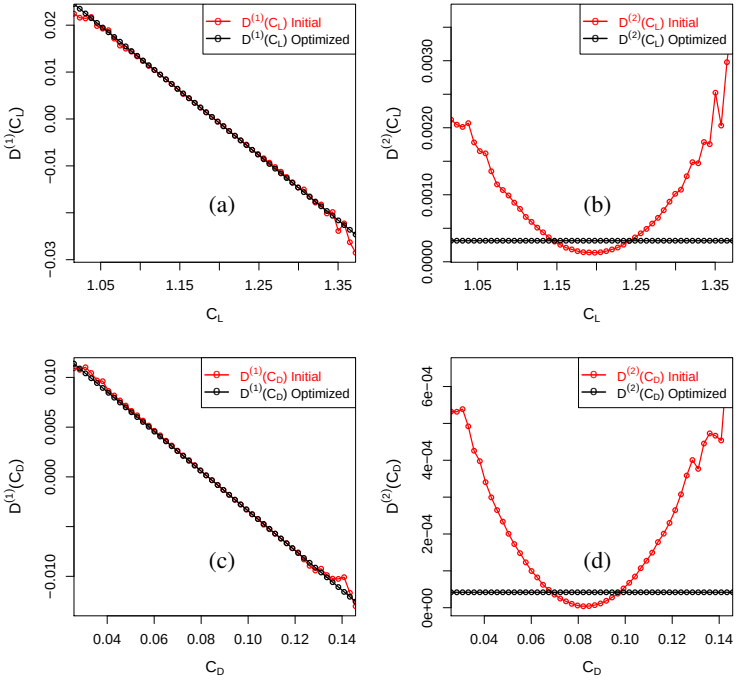

Figure 2.6: Drift and diffusion functions for C_L and C_D for AOA 11° by one-dimensional Langevin approach. Red lines represent the initial estimated values, whereas black lines the optimized values (color online). (a) C_L drift function, (b) C_L diffusion function, (c) C_D drift function and (d) C_D diffusion function.

The optimization basically consists of a quadratic modification of $D^{(2)}(X,\alpha)$, and the value found is constant in X rather than quadratic, which also corresponds to the Gaussian shape of the stationary PDFs. The spurious quadratic contributions to $D^{(2)}(X,\alpha)$ are believed to be the consequences of finite sampling errors [58]. The $D^{(1)}(X,\alpha)$ optimization here is just linear fit through the actual data passing through the stable fix point

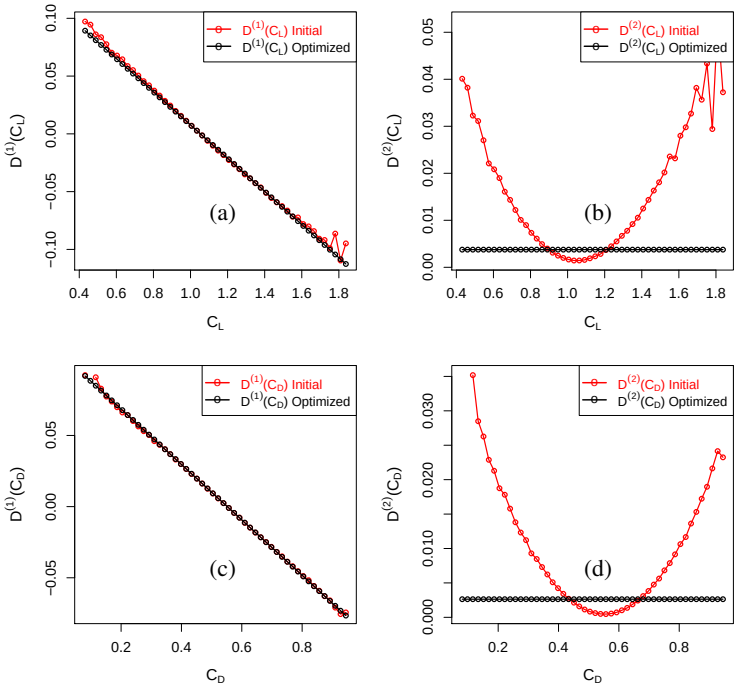

Figure 2.7: Drift and diffusion functions for C_L and C_D for AOA 28° by one-dimensional Langevin approach. Red lines represent the initial estimated values, whereas black lines the optimized values (color online). (a) C_L drift function, (b) C_L diffusion function, (c) C_D drift function and (d) C_D diffusion function.

where drift function is zero. The optimized values of drift and diffusion functions for this case for AOAs 11° and 28° are shown in Figures 2.6 and 2.7 respectively, which can be parameterized as

$$D^{(1)}(X,\alpha) = m(X - X_o), \tag{2.16}$$

$$D^{(2)}(X,\alpha) = \beta. \tag{2.17}$$

Here m is the slope of drift function, X the lift or drag coefficient, X_o the stable fix point in X where drift function is zero and β the constant diffusion function. Equations (2.16) and (2.17) stand for the estimation of the drift and diffusion functions for the system under investigation. The obtained equations (2.16) and (2.17) reflect that the system corresponds to Ornstein-Uhlenbeck process [35, 63].

By the two-dimensional Langevin approach, the drift $D_i^{(1)}(\mathbf{X},\alpha)$ and diffusion $D_{ij}^{(2)}(\mathbf{X},\alpha)$ functions are estimated using equations (2.8) and (2.9), respectively. Similarly, as in the one-dimensional embedding case, the approach is applied on $C_{Lmeasure}(t)$ and $C_{Dmeasure}(t)$ time series, and the functions are optimized for the errors. The approach is applied for same two AOAs 11° and 28°, and the obtained drift and diffusion functions are shown in Figures 2.8 and 2.9, respectively.

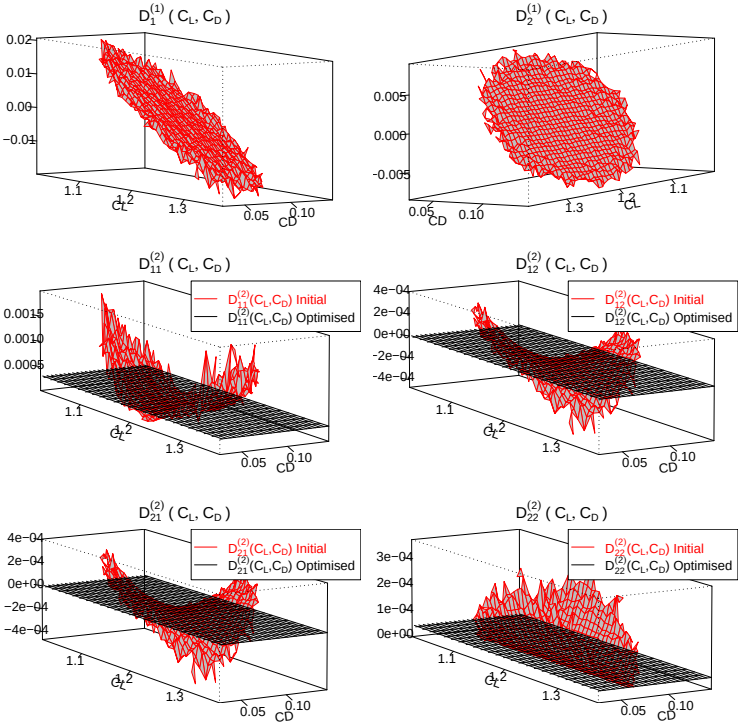

Figure 2.8: Drift and diffusion functions for C_L and C_D in two-dimensional embedding for AOA 11°. Red represents the initial estimated values, whereas black the optimized values (color online).

The results from Figures 2.8 and 2.9 reflect that the drift functions $D_i^{(1)}(\mathbf{X},\alpha)$ are independent in terms of C_L and C_D. Additionally, like in the one-dimensional case, the optimized diffusion functions $D_{ij}^{(2)}(\mathbf{X},\alpha)$ are found to be constant in $\mathbf{X}$ rather than quadratic, and the reason for spurious quadratic contributions is the same errors.

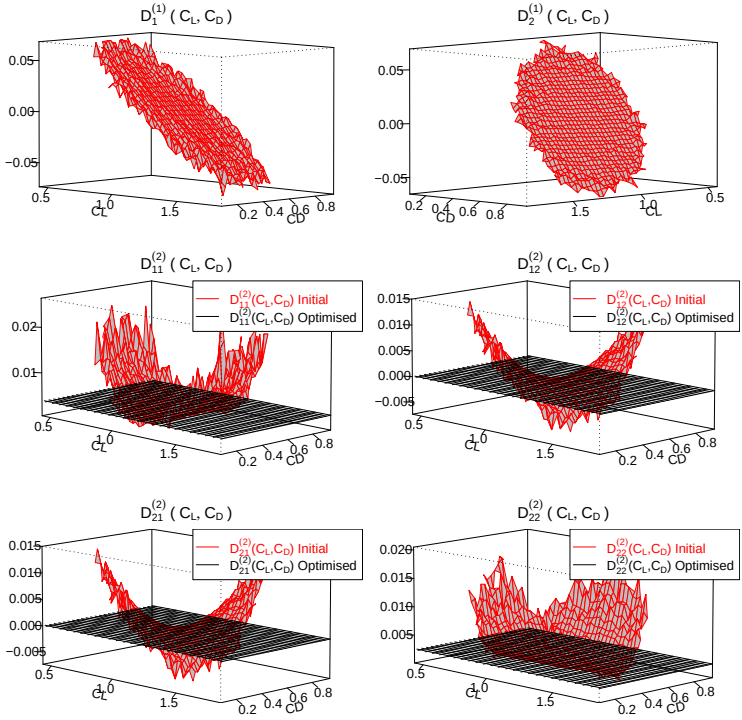

Figure 2.9: Drift and diffusion functions for C_L and C_D in two-dimensional embedding for AOA 28°. Red represents the initial estimated values, whereas black the optimized values (color online).

At the end, both the one-dimensional and two-dimensional Langevin approaches delivered similar results to each other. Therefore, for the basic stochastic model, either of these two approaches can be used. We proceed using the one-dimensional Langevin approach for the basic model considering its simplicity and less computation time. The results presented in this paper for the final model are therefore based on one-dimensional approach with extension in form of equation (2.13).

2.3.2 Final model results

Based on optimized drift and diffusion functions, when solved in time, the Langevin equation (2.4) together with the extension using equation (2.13) can model measurement time series $C_{Lmeasure}(t)$ and $C_{Dmeasure}(t)$.

The necessity for the extension term in equation (2.13) is believed to stem from unsteady aerodynamic effects, which contribute oscillations with both amplitude and phase variations in unsteady aerodynamic forces [1]; see time series of Figure 2.10. Additionally, the flow compressibility effects [1] also have potential influence on unsteady aerodynamic forces in terms of amplitude and phase variations compared to incompressible flow. In unsteady flow, these effects occur not only in dynamic stall but also in absence of dynamic stall. At low AOAs under unsteady attached flow conditions, moderate amplitude and phase changes can occur in unsteady aerodynamic forces; however, in case of increase in effective reduced frequencies, much larger effects may be generated on both the amplitude and phase in particular [1]. The amplitude of the fluctuations is proportional to AOA, i.e. the higher the AOA, the higher the amplitude of fluctuations. This is most probably due to vortex shedding in connection with unsteady detached flow over the airfoil [22].

To incorporate these additional effects, the optimized value of diffusion function $D^{(2)}(X,\alpha)$ for Langevin equation (2.4) is reduced up to about 67% in case of lift and 77% in case of drag for both AOAs. The oscillation periods for lift and drag coefficients in equation (2.13) for AOA 11°are taken as 30 ms and 23.9 ms, respectively. Similarly, in case of AOA 28°, these are taken as 32 ms for lift and 25.5 ms for drag. These are the most dominant oscillation periods obtained by considering the ACFs of lift and drag coefficient time series; see Figure 2.11. Besides this high-frequency oscillation, we see in time signals in Figure 2.10 a low-frequency modulation of the amplitude, which we denote in the following as a breathing mode. The breathing length is taken as an average of the randomly distributed breathing length occurring along the lift and drag coefficient time series. The values used here as breathing length for AOA 11° are 600 ms for lift and 420 ms for drag coefficient. Similarly, for AOA 28°, these are taken as 580 ms for lift and 610 ms for drag coefficient. In this way, in case of AOA 11°, for lift $k_o = 300$ ms and for drag $k_o = 210$ ms, i.e. half of the breathing length apply for equation (2.13). Similarly in case of AOA 28°, for lift $k_o = 290$ ms and for drag $k_o = 305$ ms. The value of A is used to fix the appropriate oscillation amplitude for model time series and is decided on the basis of minimum χ^2 value.

Figure 2.10 shows the model and measurement time series for AOAs 11° and 28°. Both the modeled and measured time series for lift and drag coefficient show a good qualitative agreement of the characteristics and the dominant amplitudes for both AOAs. The modeled and measured signals reflect complex fluctuations due to effects caused by turbulence and viscous unsteady aerodynamic response of the airfoil. As the AOA 28° belongs to

the deep stall regime (see Figure 2.16), larger magnitudes of force fluctuations are observed at AOA 28° compared to AOA 11° as expected.

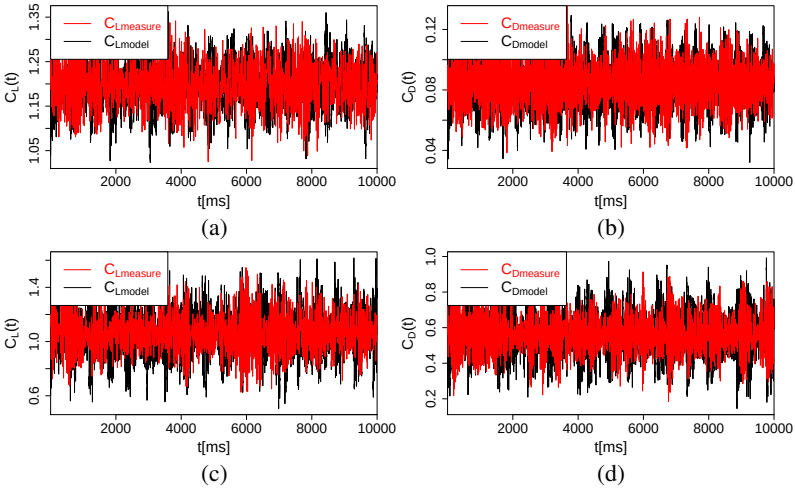

Figure 2.10: Excerpt of lift and drag coefficient time series for model and measurements for AOAs 11° and 28°. Red represents the measurements and black the model (color online). (a) $C_{Lmeasure}(t)$ and $C_{Lmodel}(t)$ for AOA 11°, (b) $C_{Dmeasure}(t)$ and $C_{Dmodel}(t)$ for AOA 11°, (c) $C_{Lmeasure}(t)$ and $C_{Lmodel}(t)$ for AOA 28°, and (d) $C_{Dmeasure}(t)$ and $C_{Dmodel}(t)$ for AOA 28°.

From a stochastic model, it cannot be expected to obtain exactly the same signal in each realization. Rather, the method aims to reproduce correct statistics. The right selection of breathing lengths for the C_L and C_D signals improves the matching of model and measurement time series.

In order to compare the behavior of model and measurements in more detail, the phase-space trajectories for AOA 11° are shown in Figure 2.11(c). The modeled trajectory shows good agreement with the actual measurements. While in each simulation it adopts a different shape due to the stochasticity; however, the form is close to the measurements. The short excerpts of C_L and C_D time series are presented in Figure 2.11(a) for measurements and Figure 2.11(b) for model results, respectively, to show the phase shift in oscillations of C_L and C_D. The figures show that the model reproduces well matching phase shifts in the oscillations of C_L and C_D with the actual measurements. For a more detailed view on the phase shifts in the oscillations of C_L and C_D, Figures 2.11(d,e) present the respective ACFs for the measurements and the model results. It can be seen that the behav-

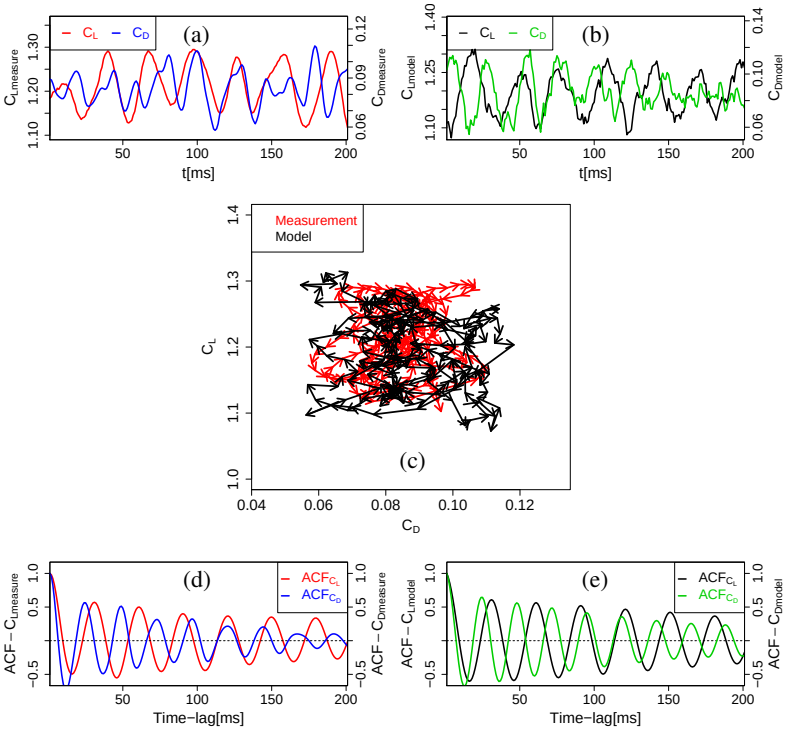

Figure 2.11: Model and measurement phase-space trajectories for AOA 11°. Short excerpts of time series and AFCs are added to illustrate the phase shift between C_L and C_D. (a) Short excerpts of C_L and C_D measurement time series, (b) short excerpts of C_L and C_D model time series, (c) model and measurement phase-space trajectories for C_L and C_D (lengths of trajectories are in ms), (d) ACFs for C_L and C_D measurement, and (e) ACFs for C_L and C_D model.

ior of the ACFs, especially the phase relation of C_L and C_D, is very similar between measurements and model results.

However, for better description of the oscillating mechanism of C_L and C_D further, a dimensionless parameter, the so-called Strouhal number, is considered, which is defined as:

$$St = \frac{fc}{u}, \tag{2.18}$$

where St is the Strouhal number, f the frequency of the vortex shedding, c the airfoil chord length and u the wind velocity. The St is estimated

for measured data at Reynolds number of Re=7x10^5 considering the most dominant frequencies observed for C_L and C_D signals; see Figure 2.17. The obtained values for C_L and C_D are $0.122 \leq St \leq 0.135$ and $0.153 \leq St \leq 0.174$, respectively, for AOAs 0° to 30°. In the stall regime, the St is slightly lower than in the attached flow regime. Similar St even for small AOAs were found for oscillating airfoils [64, 65, 66, 67, 68]. As our investigations are carried out with fixed mean AOA but with turbulent inflow, therefore, we expect that the local turbulent velocity fluctuations in the inflow will lead to similar effects like moving airfoils.

To show the similarity of the modeled and the measured data, we compare their statistics. The stationary PDFs shown in Figure 2.12 clearly demonstrate that the modeled and measured signals for both AOAs 11° and 28° yield almost similar statistics except maximum C_L values in (c). Looking at the tails of the PDFs, deviations between the statistics of modeled and measured data can be seen. This part of the statistics is of special interest as the extreme events are counted. On the other hand, one has to take into account that only few events are counted here, and thus, a large uncertainty arises. From the application, it has to be decided up to which amplitude precise results are needed, and depending on this, correspondingly long measurements have to be performed to obtain reliable statistical conclusions. The stationary PDFs of the signals are based on one-point statistics [2] and contain all the related statistical information such as mean value and the standard deviation. For better approximation, a Gaussian fit is added as a solid line through model and measured signal PDFs. Further, the quantitative comparison for this is also given in Section 2.3.3.

Although both the model and the actual measurements correspond well in terms of one-point statistical properties; however, in addition, the conditional PDFs $p(X(t+\tau)|X(t))$ are crucial to check as they contain the full information expressed by Langevin equation (2.4). The model in the existing extended state reproduces the conditional PDFs well for all time lags τ as the limitation discussed earlier (i.e. the lift and drag out-of-phase variable sinusoidal oscillation with breathing behavior along the lift and drag time series) has been covered in the form of equation (2.13). Since t is used for the continuous time, whereas our extended model is based on discrete time series, thus, it is replaced by k in equation (2.13). The results in terms of conditional PDFs for model and actual measurements for AOAs 11° and 28° at time lags $\tau = 5$ and 20 ms are shown in Figures 2.13 and 2.14, respectively, displayed as probability isolines.

The model and measurement conditional PDFs are illustrated in overlayed form for better comparison. As an example, the results for two time lags $\tau = 5$ and 20 ms are presented here. Because of the sinusoidal os-

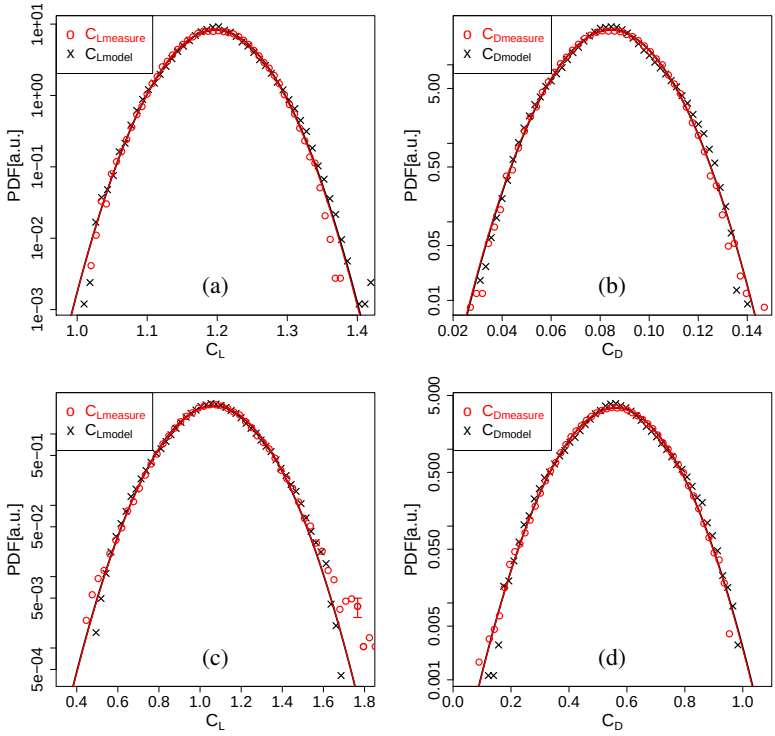

Figure 2.12: Stationary PDFs of lift and drag coefficient for AOAs 11° and 28°. The PDFs are given in arbitrary units (a.u.). Red represents the actual measurements and black the model (color online). A Gaussian PDF is added as a solid line through model and measurement signals. (a) PDF $C_{Lmeasure}$ and C_{Lmodel} for AOA 11°, (b) PDF $C_{Dmeasure}$ and C_{Dmodel} for AOA 11°, (c) PDF $C_{Lmeasure}$ and C_{Lmodel} for AOA 28°, and (d) PDF $C_{Dmeasure}$ and C_{Dmodel} for AOA 28°.

cillation effects present in lift and drag [taken into account in equation (2.13)], the conditional PFDs orientation changes as a function of a time lag. This can be easily observed by comparing illustrations of conditional PDFs at $\tau = 5$ ms with 20 ms for same AOAs. The comparison of model and measured data conditional PDFs for lift and drag coefficients suggests good similarity in the form of probability isolines. However, to show the internal statistical properties, two cuts through the conditional PDFs $p(X(t+\tau)|X(t))$ at $\tau = 20$ ms for fixed values of $X(t)$ are provided as an example in Figure 2.13. The PDFs of cuts show that the model reproduces

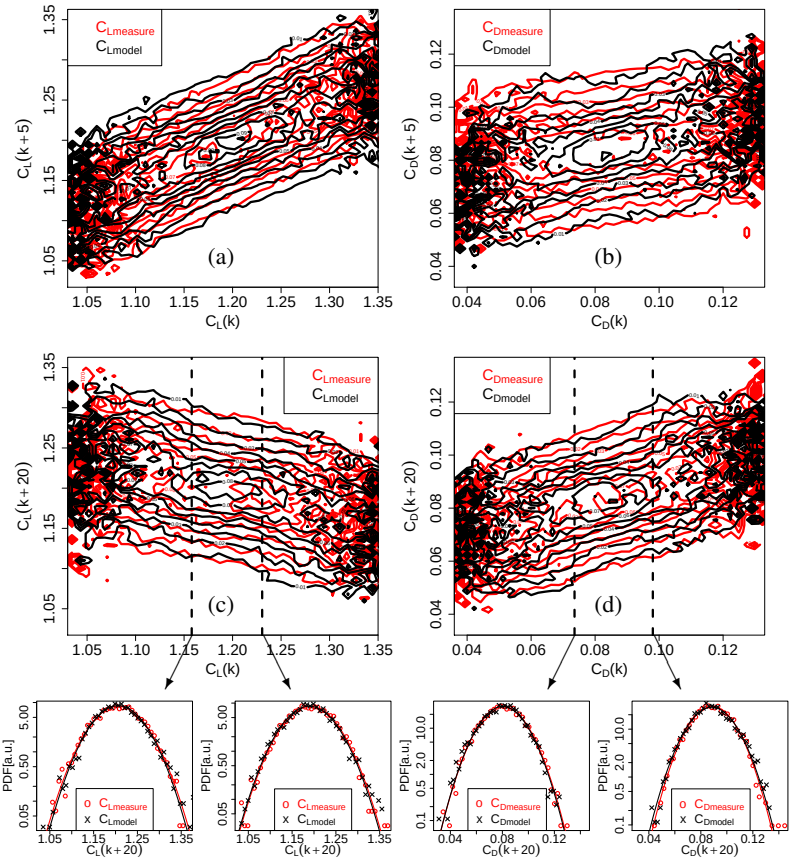

Figure 2.13: C_L and C_D conditional PDFs for time lags $\tau = 5$ and 20 ms, AOA 11°. Red denotes the actual measurements and black the model (color online). PDFs are shown as probability isolines. The levels of the isolines correspond to a factor of 2 in the probabilities. (a) C_L measurement and model at $\tau = 5$ ms, (b) C_D measurement and model at $\tau = 5$ ms, (c) C_L measurement and model at $\tau = 20$ ms, and (d) C_D measurement and model at $\tau = 20$ ms. Additionally, for (c) and (d), two one-dimensional cuts are shown for $p(X(t+\tau)|X(t))$ at $\tau = 20$ ms for fixed values of $X(t)$. The red circles denote the measurements and black crosses the model. The solid lines are added as Gaussian PDFs through the respective signals. The PDFs of cuts are given in arbitrary units (a.u.).

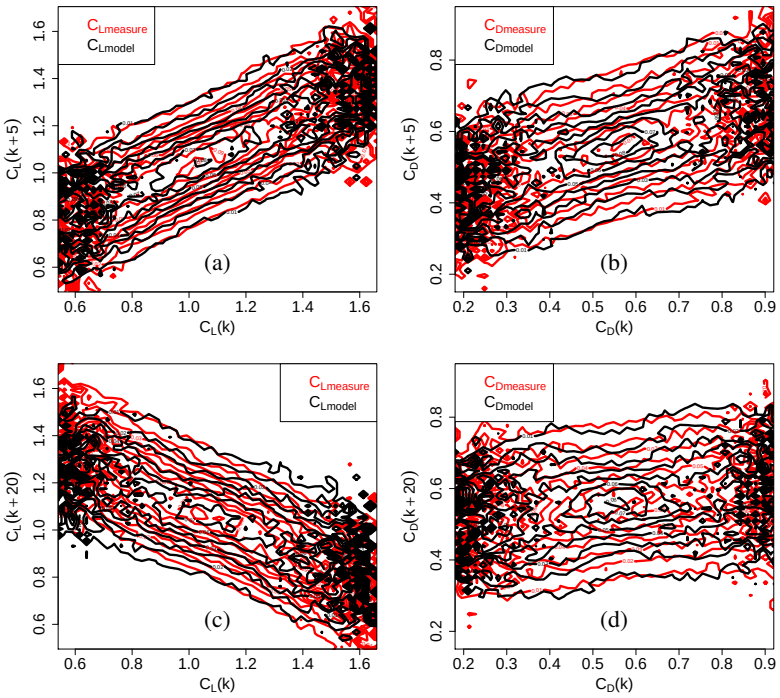

Figure 2.14: C_L and C_D conditional PDFs for time lags $\tau = 5$ and 20 ms, AOA 28°. Red represents the measurements and black the model (color online). PDFs are shown as probability isolines. The levels of the isolines correspond to a factor of 2 in the probabilities. (a) C_L measurement and model at $\tau = 5$ ms, (b) C_D measurement and model at $\tau = 5$ ms, (c) C_L measurement and model at $\tau = 20$ ms, and (d) C_D measurement and model at $\tau = 20$ ms.

the similar statistics to actual measurements for both C_L and C_D at $\tau = 20$ ms.

2.3.3 Quantitative comparison

Besides graphical comparison, the quantitative comparison for the selected AOAs as an example is given in Table 2.1. For the quantitative comparison, the final optimized value of χ^2 from equation (2.10) is compared with intrinsic standard error (statistical error) obtained through equation (2.15). The given values are for 15 simulations for C_L and C_D for each AOA. The

values stand for χ^2 and statistical error in terms of their mean for 15 simulations.

Table 2.1: Quantitative comparison of model and measurements for AOAs 11° and 28°.

AOA	Coefficient	Mean χ^2	Mean S_{Error}
11°	C_L	0.018	0.018
11°	C_D	0.032	0.018
28°	C_L	0.090	0.018
28°	C_D	0.080	0.018

In our case, the χ^2 value is the direct measure of the difference between two data sets describing their relationship. Here, model and measurements are taken as two data sets. The comparison of χ^2 with standard error demonstrates the quality of results. The obtained χ^2 values in case of AOA 11° are smaller than the χ^2 values for AOA 28°, which describe better results for AOA 11° than AOA 28°. The quantitative comparison in terms of χ^2 with statistical error shows that the χ^2 values in case of AOA 11° are close to the statistical error, yet a bit larger in case of drag coefficient. The comparison for AOA 28° shows the larger χ^2 values than the intrinsic statistical error for both lift and drag coefficients. A similar kind of difference is found for other AOAs such as these two AOAs (i.e. for some AOAs, the χ^2 is found larger and for some less or close to the statistical error). This difference is mainly stemming from the breathing length taken here on average basis, which in reality is randomly distributed along the lift and drag coefficient time series of actual measurements. By taking the breathing length in a random way like measurements, the results may be improved further. For best quality, χ^2 value should be in order or less (in magnitude) than the standard error, therefore, still the model needs some minor corrections especially in terms of breathing length.

2.3.4 Comparison of model and measurements for AOAs 0° to 30°

Applying the same approach, the modeling is performed for AOAs ranging from 0° to 30°. The detailed results have been presented for two AOAs as an example to avoid the repetition of similar illustrations and make the paper easy to understand. The conditional PDFs $p(X(t+\tau)|X(t))$ for more time lags τ to show have also been avoided for the same reason. The results for all AOAs ranging from 0° to 30° are summarized and presented in Figures 2.15 and 2.16.

Figure 2.15 shows the slope (for drift function) and the optimized diffusion function for C_L and C_D for AOAs 0° to 30° derived without model

terms for oscillation and breathing. The slope for C_L increases on average for AOAs 0° to 15° and then decreases for rest of the higher AOAs as the stall region becomes dominant on the system leading to decrease in C_L; see Figure 2.16. On the other hand, the slope for C_D first decreases on average for AOAs 0° to 9° for attached flows and then starts increasing onwards (as the flow separation starts) up to AOA 15°. Thereafter, beyond AOA 15°, the slope for C_D decreases like for C_L where the stall region becomes dominant on the system, causing significant increase in C_D.

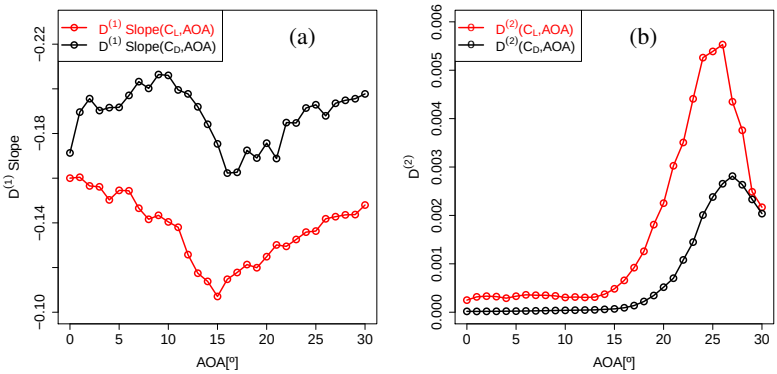

Figure 2.15: Slope of drift function and optimized diffusion function for AOAs 0° to 30° derived without model terms for oscillation and breathing. Red represents the curves for C_L model and black for C_D model (color online). (a) C_L and C_D slope for drift function, and (b) C_L and C_D diffusion function.

In case of diffusion function for C_L, there is very slight fluctuation (i.e. increase and decrease) for AOAs 0° to 15°, and then there is dramatic increase up to AOA 26° and rapid decrease after 26° up to 30°. This is mainly because the region between AOAs 15° and 30° is highly dynamic because of increased flow separation over the suction side of airfoil. In case of C_D, initially, there is very slight and linear increase in diffusion function for AOAs 0° to 17°, and then there is significant increase up to AOA 27° and later rapid decrease up to 30°.

It is important to mention here that the model in the extended form for most of the AOAs uses about 33% and 23% of the optimized diffusion function for C_L and C_D, respectively. However, for some AOAs, the fraction changes for both C_L and C_D depending mainly on the size of breathing length and its random way of occurrence along the time series. The amount of reduction in diffusion function allows to fix the additional effects into

the model in form of the extension part in equation (2.13). The slope for drift function remains unchanged for both C_L and C_D. The drift slope and diffusion function values shown here apply for measured AOAs. The intermediate values can be obtained by interpolation.

Figure 2.16 shows the summary of final model results for AOAs 0° to 30° in terms of static lift and drag curves with dynamic drift function. In this illustration, the dynamics of the model results for each AOA is compared with actual measurements. Additionally, the comparison of stochastic approach with classical averaging procedure is also presented.

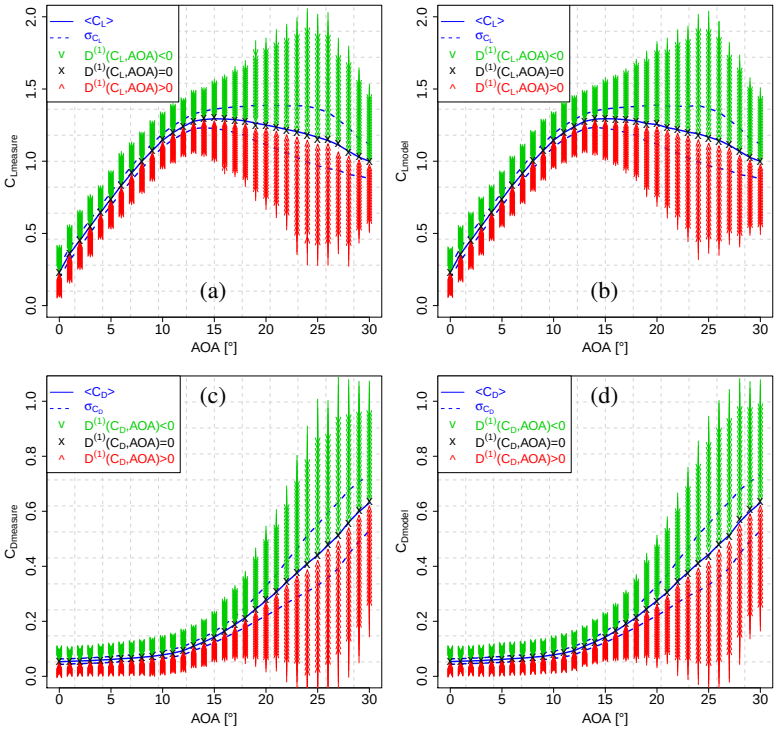

Figure 2.16: Static lift and drag coefficient curves with dynamic drift function for model and measurements for AOAs 0° to 30° (color online). The solid blue lines represent the mean C_L and C_D curves, whereas the dashed blue lines represent the standard deviation from the mean C_L and C_D curves. The red and green arrows denote the positive and negative drift functions for C_L and C_D trying to move towards the black crosses, which represent the stable fixed points where the drift function is zero. (a) C_L measurement, (b) C_L model, (c) C_D measurement and (d) C_D model.

In the classical averaging procedure, the static lift and drag curves of an airfoil are defined and characterized in the form of mean and standard deviation of lift and drag signals over each AOA. The lift and drag coefficients are obtained using equations (2.2) and (2.3), respectively. The standard deviation demonstrates the fluctuation of lift and drag coefficients from the mean. The drift function is obtained through Langevin approach using equation (2.5), which provides the complete map of the local dynamics of the lift and drag coefficients for each AOA. The red arrows indicate a deterministic increase of lift and drag coefficients over the time, and green arrows denote a deterministic decrease of lift and drag coefficients over the time. The black crosses represent the stable fix points where the drift function is zero, matching the common mean lift and drag curves. The comparison of approaches suggests that the stochastic approach gives more insight in terms of C_L and C_D local dynamics by expressing complete response map over each AOA, whereas the usual averaging approach only determines the fluctuations from the mean in terms of standard deviation and disregards the dynamical information.

In particular, these findings show that for small values of AOA, the decreasing slope of the drift function will lead to a reduced damping of the noise, i.e. increase the fluctuations in C_L and C_D. For larger AOAs, the rapid increase of the diffusion term causes further increase in C_L and C_D fluctuations . Thus, we can interpret the results of our analysis as a transition of a stable flow situation (small AOA), which loses the stability (approaching AOA 15°), and then a transition to an unstable flow situation takes place (AOA $>$ 15°) marked by a rapid increase of the noise, measured as diffusion term.

The comparison of model and actual measurements for AOAs 0° to 30° through both ways show good agreement. In case of classical averaging approach, the model and measurement mean and standard deviation curves for both lift and drag coefficients look very similar to each other. The stable fix points (the black crosses) obtained through stochastic approach follow the mean lift and drag curves and correspond well for both model and measurements for lift and drag coefficient curves. These could be called Langevin lift and drag curves based on the approach used. The local dynamics in the form of drift function represent also very good agreement between model and actual measurements except some minor offset at stall region in case of lift and drag models.

2.3.5 Aerodynamic interaction between inflow and airfoil response

Because of the strong oscillations in lift and drag forces, as discussed earlier, the aerodynamic interaction between the turbulent inflow and the airfoil response has been investigated. Wind inflow measurements were performed using a hot-wire probe in the test section behind the fractal square grid. Power spectral density (PSD) of inflow velocity is compared with C_L and C_D in Figure 2.17 for the example AOA of 28°. Similar spectra are observed for the whole range of AOAs under investigation. The PSD of the velocity is shifted in y-direction for clarity of presentation.

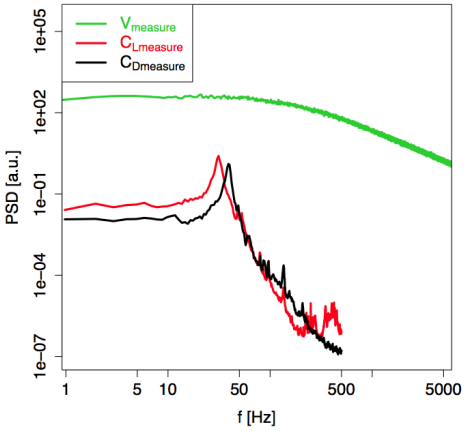

Figure 2.17: Power spectral densities (PSDs) of inflow velocity, C_L and C_D. Green represents the PSD of turbulent wind inflow generated by fractal square grid (note the -5/3 decay for frequencies higher than 200Hz), red that of C_L and black the C_D, respectively, for AOA 28° (color online). PSDs are given in arbitrary units (a.u.).

The comparison of the spectra shows that the wind inflow signal is free of pronounced periodicity. The spectrum is a quite unstructured broad band noise and shows the Kolmogorov spectral decay with the -5/3 power law for frequencies higher than 200Hz. On the other hand, the PSDs of C_L and C_D show mainly the dominating peaks at $f = 31.25$ Hz and $f = 39.2$ Hz, respectively. These peaks together with smaller maxima at higher frequencies can most probably be addressed to unsteady aerodynamic effects like those discussed in Section 2.3.2. Further physical reasons and details for the difference in the frequencies of C_L and C_D are unclear to us and deserve further investigations of these aerodynamic instabilities on the background of

high Reynolds numbers and noisy turbulent environment. In our stochastic model ansatz, we simply took care of these different oscillations by using different frequencies.

2.4 Conclusion

For an advanced dynamic characterization of lift and drag forces on wind turbine airfoils, a stochastic model for the dynamics of C_L and C_D has been developed. As a first example, an airfoil FX 79-W-151A has been investigated. Dynamic measurements of lift and drag forces were performed in a wind tunnel. Turbulent inflow with an intensity of 4.6% was generated by a fractal square grid to mimic typical intermittent velocity fluctuations commonly known for free field wind situations. From these measurements, the parameters of the stochastic model have been derived for AOAs ranging from 0° to 30°. The results are summarized in Figure 2.16 comprising static lift and drag curves with dynamic drift functions based on classical averaging and stochastic approaches, respectively. Additional to the standard procedure, the stochastic approach offers further insight in terms of the local dynamics of C_L and C_D described by the dynamic model in equation (2.13).

In the existing state, i.e. Langevin equation together with extension, the model reproduces well matching C_L and C_D time series, stationary PDFs and conditional PDFs $p(X(t+\tau)|X(t))$ for all time lags τ. For illustration, detailed results have been presented for two AOAs selected as examples of pre-stall and deep stall regimes. However, the quantitative comparison still suggests some minor improvements in the model as the obtained χ^2 is larger than the statistical error for some AOAs. This could be achieved by minor corrections especially to the breathing length, which is taken on an average basis in equation (2.13), whereas the actual breathing length appears to be randomly distributed along the lift and drag time series. This could also improve the visual matching of model time series with actual measurements.

We would like to stress that in this study, only one example airfoil has been studied in an exemplary flow situation, in order to develop and demonstrate the method and its application. Each airfoil possesses different dynamics, and therefore, drift and diffusion functions will in principle differ for different airfoils. In addition, these functions are also expected to differ for different turbulence parameters and to be influenced by further effects such as tower interaction. Moreover, the additional effects covered in the form of the extension to the basic model are also expected to differ in these cases. Hence, for future developments, more airfoils need to be tested under

different, realistic conditions. From these measurements, additional model parameters can be derived as described in this paper.

The model is being developed to provide a proper description and characterization of dynamic lift and drag forces under turbulent inflow conditions, which could help to extract more detailed and complete dynamical loading information acting on the wind turbine blades. Aerodynamic models such as AeroDyn [31] and other similar codes use traditional lookup tables that contain static C_L and C_D data for fixed AOAs, and therefore, lack information on the system dynamics at small time scales. The proposed model is an alternative that is aimed to replace the traditional lookup tables in aerodynamic codes and provide numerically the C_L and C_D with local dynamics that can lead to an improved rotor design under unsteady wind inflow. In a further step, an aerodynamic model integrated with the model under investigation shall be combined with a WEC model such as FAST [25] to provide a stochastic rotor model.

We would like to thank Patrick Milan and Wided Medjroubi for helpful discussions. Also, we would like to thank the referees for their comments and suggestions that helped to improve the paper. M. R. Luhur kindly acknowledges financial support by Quaid-e-Awam University of Engineering, Sciences and Technology, Nawabshah, Pakistan.

Bibliography

[1] J. G. Leishman. Challenges in modeling the unsteady aerodynamics of wind turbines. *Wind Energy*, 5:85–132, 2002.

[2] A. Morales, M. Wächter and J. Peinke. Characterization of wind turbulence by higher order statistics. *Wind Energy*, 15(3):391–406, 2012.

[3] F. Böttcher, S. Barth and J. Peinke. Small and large scale fluctuations in atmospheric wind speeds. *Stochastic Environmental Research and Risk Assessment*, 12:299–308, 2007.

[4] J. Vindel, C. Yague and J. M. Redondo. Structure function analysis and intermittency in the atmospheric boundary layer. *Nonlinear Processes in Geophysics*, 15:915–929, 2008.

[5] N. Troldborg, J. N. Sørensen, R. Mikkelsen and N. N. Sørensen. A simple atmospheric boundary layer model applied to large eddy simulations of wind turbine wakes. *Wind Energy*, 17(4):657–669, 2014.

[6] J. C. Kaimal and J. J. Finnigan. *Atmospheric Boundary Layer Flows. Their Structure and Measurement*. Oxford University Press, New York, 1994.

[7] H. Long, J. Wu, F. Mattew and P. Tavner. Fatigue analysis of wind turbine gearbox bearings using SCADA data and Miner's rule. *Scientific Proceedings of EWEA*, Brussels, Belgium, 2011.

[8] T. Mücke, D. Kleinhans and J. Peinke. Atmospheric turbulence and its influence on the alternating loads on wind turbines. *Wind Energy*, 14:301–316, 2011.

[9] M. O. .L. Hansen and H. A. Madsen. Review Paper on Wind Turbine Aerodynamics. *Journal of Fluids Engineering*, 133:114001, 2011.

[10] D. M. Eggleston and F. S. Stoddard. *Wind turbine engineering design*. Van Nostrand Reinhold Company, New York, USA, July 1987.

[11] J. G. Leishman. *Principles of Helicopter Aerodynamics, Second Edition*. Cambridge University Press, Cambridge, New York, USA, 2006.

[12] G. Wolken-Möhlmann, P. Knebel, S. Barth and J. Peinke. Dynamic lift measurements on a FX79W151A airfoil via pressure distribution on the wind tunnel walls. *Journal of Physics: Conference Series*, 75: 012026, 2007.

[13] R. Pereira, G. Schepers and M. D. Pavel. Validation of the Beddoes-Leishman dynamic stall model for horizontal axis wind turbines using MEXICO data. *Wind Energy*, 16:207–219, 2013.

[14] H. Snel. Review of Aerodynamics for Wind Turbines. *Wind Energy*, 6:203–211, 2003.

[15] P. Fuglsang, I. Antoniou, K. S. Dahl and H. A. Madsen. *Wind tunnel tests of the FFA-W3-241, FFA-W3-301 and NACA 63-430 airfoils*. Scientific report Risø-R-1041(EN), Risø National Laboratory, Denmark, December 1998.

[16] P. Fuglsang, K. S. Dahl and I. Antoniou. *Wind tunnel tests of the Risø-A1-18, Risø-A1-21 and Risø-A1-24 airfoils*. Scientific report Risø-R-1112(EN), Risø National Laboratory, June 1999.

[17] W. A. Timmer and R. P. J. O. M. van Rooij. Summary of the Delft University wind turbine dedicated airfoils. *Journal of Solar Energy Engineering, Transactions ASME*, 125:488–496, 2003.

[18] T. Sant. *Improving BEM-Based Aerodynamic Models in Wind Turbine Design Codes*. PhD thesis, Delft University Wind Energy Research Institute (DUWIND), the Netherlands, 2007.

[19] L. J. Vermeera, J. N. Sørensen and A. Crespo. Wind turbine wake aerodynamics. *Progress in Aerospace Sciences*, 39:467–510, August–October 2003.

[20] A. T. Conlisk. Modern Helicopter Rotor Aerodynamics. *Progress in Aerospace Sciences*, 37:419–476, 2001.

[21] H. Snel. Review of the Present Status of Rotor Aerodynamics. *Wind Energy*, 1:46–69,1998.

[22] F. Bertagnolio, F. Rasmussen, N. N. Sørensen, J. Johansen and H. A. Madsen. A stochastic model for the simulation of wind turbine blades in static stall. *Wind Energy*, 13:323–338, 2010.

[23] K. Åhlund. *Investigation of the NREL NASA/Ames Wind Turbine Aerodynamics Database*. Scientific report FOI-Rñ1243ñSE, Swedish Defence Research Agency, Stockholm, Sweden, June 2004.

[24] B. Montgomerie and S. E. Thor. Aerodynamics for Wind Turbines. *Summary of IEA R&D Wind -16th Joint Action Symposium*, Boulder USA, May 2003.

[25] J. M. Jonkman and M. L. Buhl Jr. *FAST User's Guide*. Technical report NREL/EL-500-38230, National Renewable Energy Laboratory, Golden, Colorado, USA, August 2005.

[26] D. J. Laino and A. C. Hansen. *User's Guide to the Wind Turbine Dynamics Computer Program YawDyn*. Technical report prepared for NREL under subcontract No. TCX-9-29209-01, University of Utah, January 2003.

[27] D. J. Laino and A. C. Hansen. *User's Guide to the Computer Software Routines AeroDyn Interface for ADAMS*. Technical report prepared for NREL under subcontract No. TCX-9-29209-0, University of Utah, Salt Lake City, USA, September 2001.

[28] S. Mulski. SIMPACK Multi-Body Simulation. *Wind and Drivetrain Conference*, SIMPACK AG, Hamburg, Germany, September 2012.

[29] M. L. Buhl Jr. and A. Manjock. *A Comparison of Wind Turbine Aeroelastic Codes Used for Certification*. Conference paper NREL/CP-500-39113, National Renewable Energy Laboratory, Golden, Colorado, USA, January 2006.

[30] S. Øye. *FLEX5 User Manual*. Technical report, Danske Techniske Hogskole, 1999.

[31] P. J. Moriarty and A. C. Hansen. *AeroDyn Theory Manual*. Technical report NREL/EL-500-36881, National Renewable Energy Laboratory, Golden, Colorado, USA, January 2005.

[32] N. D. Kelley and B. J. Jonkman. *Overview of the TurbSim Stochastic Inflow Turbulence Simulator*. Technical report NREL/TP-500-41137, National Renewable Energy Laboratory, April 2007.

[33] B. J. Jonkman and L. Kilcher. *TurbSim User's Guide*. Technical report, National Renewable Energy Laboratory, September 2012.

[34] G. Weinzierl. *A BEM Based Simulation-Tool for Wind Turbine Blades with Active Flow Control Elements*. Diploma thesis, Technical University of Berlin, Germany, April 2011.

[35] H. Risken. *The Fokker-Planck Equation, Second Edition*. Springer, Berlin, Germany, 1996.

[36] W. H. Press, S. A. Teukolsky, W. T. Vetterling and B. P. Flannery. *Numerical Recipes in C The art of scientific computing*. Cambridge University Press, New York, USA, 1992.

[37] D. Kleinhans, R. Friedrich, M. Wächter and J. Peinke. Markov properties in presence of measurement noise. *Physical Review E*, 76:041109, 2007.

[38] D. Kleinhans, R. Friedrich, A. Nawroth and J. Peinke. An iterative procedure for the estimation of drift and diffusion coefficients of Langevin processes. *Physics Letters A*, 346:42–46, 2005.

[39] D. Althaus. *Niedriggeschwindigkeitsprofile*. Friedr. Vieweg & Sohn Verlags gesellschaft mbH, Braunschweig/Weisbaden, Germany, 1996.

[40] F. X. Wortmann. *Airfoil Profiles for Wind Turbines*. Universität Stuttgart, Institute of Aerodynamics and Gas Dynamics, IAG 78-9.

[41] J. Schneemann, P. Knebel, P. Milan and J. Peinke. Lift measurements in unsteady flow conditions. *Scientific Proceedings of EWEC*, Warsaw, Poland, 2010.

[42] J. Schneemann, P. Milan, M. R. Luhur, P. Knebel and J. Peinke. Lift measurements in turbulent flow conditions. *Scientific Proceedings of DEWEK*, Bremen, Germany, 2010.

[43] R. E. Seoud and J. C. Vassilicos. Dissipation and decay of fractal-generated turbulence. *Physics of Fluids*, 19:105108, 2007.

[44] F. Böttcher, C. Renner, H. P. Waldl and J. Peinke. On the Statistics of Wind Gusts. *Boundary-Layer Meteorology*, 108:163–173, 2003.

[45] P. A. Krogstad and P. A. Davidson. Near-field investigation of turbulence produced by multi-scale grids. *Physics of Fluids*, 24:035103, 2012.

[46] P. A. Krogstad and P. A. Davidson. Freely decaying homogeneous turbulence generated by multi-scale grids. *Journal of Fluid Mechanics*, 680:417–434, 2011.

[47] D. Hurst and J. C. Vassilicos. Scalings and decay of fractal-generated turbulence. *Physics of Fluids*, 19:035103, 2007.

[48] W. K .George and H. Wang. The exponential decay of homogeneous turbulence. *Physics of Fluids*, 21:025108, 2009.

[49] M. Oberlack and G. Khujadze. Fractal-generated turbulent scaling laws from a new scaling group of the multi-point correlation equation. *Advances in Turbulence XII, Springer Proceedings in Physics*, 132: 681-684, 2009.

[50] M. Oberlack and G. Khujadze. Fractal-generated turbulent scaling laws from a new scaling group of the multi-point correlation equation. *Progress in Turbulence III, Springer Proceedings in Physics*, 131:13-19, 2009.

[51] R. Stresing, J. Peinke, R. E. Seoud and J. C. Vassilicos. Defining a New Class of Turbulent Flows. *Physical Review Letters*, 104:194501, 2010.

[52] N. Mazellier and J. C. Vassilicos. Turbulence without Richardson–Kolmogorov cascade. *Physics of Fluids*, 22:075101, 2010.

[53] *Radial force sensor with 2 measuring axis*. Available online: http://www.honigmann.com/k16/Multi-axis-force-sensors.html, accessed on 15 July 2013.

[54] M. R. Luhur, J. Schneemann, P. Milan and J. Peinke. Stochastic modeling of lift dynamics in turbulent inflows. *Seminar Proceedings of EAWE*, Trondheim, Norway, 2010.

[55] D. Althaus and F. X. Wortmann. *Stuttgarter Profilkatalog I* Vieweg, 1981.

[56] R. Friedrich, J. Peinke, M. Sahimi and M. R. R. Tabar. Approaching complexity by stochastic methods: From biological systems to turbulence. *Physics Reports*, 506:87–162, 2011.

[57] S. Siegert, R. Friedrich and J. Peinke. Analysis of data sets of stochastic systems. *Physics Letters A*, 243:275–280, 1998.

[58] J. Gottschall and J. Peinke. On the definition and handling of different drift and diffusion estimates. *New Journal of Physics*, 10:083034, 2008.

[59] A. N. Kolmogorov. Über die analytischen methoden in der wahrscheinlichkeitsrechnung. *Mathematische Annalen*, 140:415–458, 1931.

[60] M. Siefert, A. Kittel, R. Friedrich and J. Peinke. On a quantitative method to analyse dynamical and measurement noise. *Europhysics Letters*, 61:466–472, 2003.

[61] M. Siefert and J. Peinke. Reconstruction of the deterministic dynamics of stochastic systems. *International Journal of Bifurcation and Chaos*, 14:2005–2010, 2004.

[62] F. Böttcher, J. Peinke, D. Kleinhans, R. Friedrich, P. G. Lind and M. Haase. Reconstruction of Complex Dynamical Systems Affected by Strong Measurement Noise. *Physical Review Letters*, 97:090603, 2006.

[63] C. Honisch and R. Friedrich. Estimation of Kramers-Moyal coefficients at low sampling rates. *Physical Review E*, 83:066701, 2011.

[64] W. Shyy and Y. Lian. *Computational Investigation of Unsteady Low-Reynolds Number Aerodynamics for Micro Air Vehicles*. Scientific report FA9550-06-1-049, University of Michigan, 2007.

[65] W. Ren, H. Hu, H. Liu and J. C. Wu. An Experimental Investigation on the Asymmetric Wake Formation on an Oscillating Airfoil. *51st AIAA Aerospace Sciences Meeting including the New Horizons Forum and Aerospace Exposition*, Grapevine, Texas, 7-10 January 2013.

[66] M. L. Yu, H. Hu and Z. J. Wang. Experimental and Numerical Investigation on the Asymmetric Wake Vortex Structures around an Oscillating Airfoil. *50th AIAA Aerospace Sciences Meeting including the New Horizons Forum and Aerospace Exposition*, Nashville, Tennessee, 9-12 January 2012.

[67] M. L. Yu, H. Hu and Z. J. Wang. A Numerical Study of Vortex-Dominated Flow around an Oscillating Airfoil with High-Order Spectral Difference Method. *48th AIAA Aerospace Sciences Meeting including the New Horizons Forum and Aerospace Exposition*, Orlando, Florida, 4-7 January 2010.

[68] W. Medjroubi, B. Stoevesandt and J. Peinke. Wake classification of heaving airfoils using the spectral/hp element method. *Journal of Computational and Applied Mathematics*, 236:3774–3782, 2012.

Chapter 3

Local force dynamics on a rotor blade element

The content presented in this chapter is published as "M. R. LUHUR, J. PEINKE and M. WÄCHTER. Stochastic modeling of lift and drag dynamics to obtain aerodynamic forces with local dynamics on rotor blade under unsteady wind inflow, *Mehran University Research Journal of Engineering & Technology*, 33(1):39-48, 2014". Here, Footnote 1 is added for further information to the reader that is not included in the original publication.

Abstract This contribution provides the development of a stochastic lift and drag model for an airfoil FX 79-W-151A under unsteady wind inflow based on wind tunnel measurements. Here we present the integration of the stochastic model into a well-known standard blade element momentum (BEM) model to obtain the corresponding aerodynamic forces on a rotating blade element. The stochastic model is integrated as an alternative to static tabulated data used by the classical BEM. The results show that in comparison to the classical BEM, the BEM integrated with stochastic approach additionally reflects the local force dynamics, and therefore provides more information on the aerodynamic forces that can be used by wind turbine simulation codes.

3.1 Introduction

The dynamic nature of the wind contributes to the complex operation of wind turbines being exposed to turbulent atmospheric air-flows having well-known complex statistics and gusty behavior [1, 2, 3]. The operation of wind turbines in such environment leads to several risks especially in terms of highly dynamic mechanical loads [4, 5]. Several studies exist on placing an airfoil into a steady low-turbulence inflow and observing the

lift and drag properties at constant angles of attack (AOAs) [6, 7, 8, 9]; however, the complexity of open-air turbulent flows is yet to be perceived fully.

The blade aerodynamics under turbulent wind conditions changes profoundly compared to steady low-turbulence flows. In unsteady flow the fast variations in AOA can lead to well-known dynamic stall effect resulting in significant increase in lift dynamics; compare [10, 11, 12].

To estimate the aerodynamic forces on wind turbine rotor blades several engineering and computational fluid dynamics (CFD) techniques exist today [1, 13, 14, 15, 16]. However, from performance point of view, still engineering methods are the leading choice over CFD [17]. CFD yet needs more powerful computers to achieve acceptable computational time [18]. Still most wind turbine aerodynamic computations are performed with standard BEM method due to its simplicity and computational efficiency in particular [18].

Nevertheless, most of the aerodynamic models use tabulated static data for airfoils at constant AOAs [19, 20] to estimate the forces on wind turbine blades, and therefore lack the information on local force dynamics.

In this work, a stochastic model of the lift and drag dynamics is integrated into a classical BEM as an alternative to static airfoil data table to obtain the aerodynamic forces with complete local dynamics. The model evaluates the lift and drag forces numerically as function of AOA. The stochastic forces are obtained for a rotating blade element and compared with the results obtained with classical BEM (with the use of static airfoil data table). The model is being developed to extract and provide the detailed local loading information on the wind turbine blades, which could lead to an optimum rotor design under turbulent wind conditions. The final goal is to achieve an aerodynamic model like AeroDyn [19] based on stochastic approach. Later, it could be combined with a wind energy converter model to obtain a stochastic rotor model.

The paper is structured as follows. Section 3.2 describes the lift and drag modeling approach. Section 3.3 explains the calculation of rotor normal and tangential forces for a blade element in the context of classical and stochastic BEM methods. Section 3.4 presents the results from both the classical and stochastic BEM approaches. Finally Section 3.5 concludes the outcome.

3.2 Stochastic lift and drag model

The stochastic modeling of lift and drag dynamics is consisting of two steps. First, measurements have been performed in a wind tunnel to obtain

the airfoil data. Second, a stochastic approach is applied with an optimization scheme to model the lift and drag dynamics.

3.2.1 Measurements

The measurements have been performed in a closed loop wind tunnel of Oldenburg University for an airfoil FX 79-W-151A having chord length of 0.2m. The wind tunnel has a test section of 1m wide, 0.8m high and 2.6m long. The turbulent inflow was generated using a fractal square grid having closer characteristics to natural wind [21, 22]. The lift and drag forces were measured directly using two strain gauge force sensors fixed at the end points of an airfoil in span-wise direction as shown in Figure 3.1. The mean wind velocity and Reynolds number were 50m/s and $7\text{x}10^5$, respectively. Further details of the measurements can be found in [22].

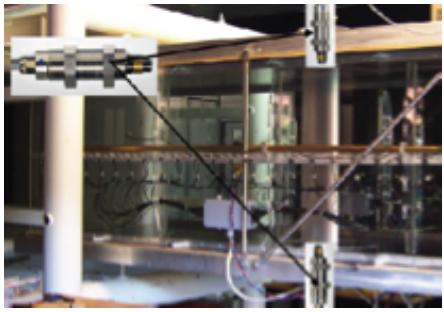

Figure 3.1: View of the wind tunnel test section. Black arrows show the position of force sensors installed at the end points of the vertically mounted airfoil in the test section.

3.2.2 Stochastic Modeling

The lift and drag coefficients are modeled using a stochastic approach, which extracts most of the information available in the system dynamics. The coefficients of lift and drag are calculated from measured data using the relations [22]

$$C_L = \frac{F_L}{qA}, \tag{3.1}$$

$$C_D = \frac{F_D}{qA}, \tag{3.2}$$

where F_L is the lift force, F_D the drag force, q the inflow dynamic pressure and A the area of the airfoil.

The stochastic approach is applied on the measured time series of lift and drag coefficients using a first order stochastic differential equation called the Langevin equation, cf. [23]. The approach is based on drift and diffusion functions coupled with a noise term. It models the complex statistics by means of random numbers. The approach reads

$$\frac{dX(t)}{dt} = D^{(1)}(X) + \sqrt{D^{(2)}(X)}\,\Gamma(t), \tag{3.3}$$

where $\Gamma(t)$ is a Gaussian white noise termed as Langevin force [23] with mean value of $\langle\Gamma(t)\rangle = 0$ and variance $\langle\Gamma^2(t)\rangle = 2$. It is an uncorrelated statistical noise obeying the probability density function (PDF) of normal distribution.

The $D^{(1)}(X)$ and $D^{(2)}(X)$ are the drift and diffusion functions, also known as first and second Kramers-Moyal coefficients for $X(t)$. The drift and diffusion functions can be estimated from measured time series using the relation [24, 25, 26]

$$D^{(n)}(X,\alpha)_{n=1,2} = \lim_{\tau\to 0}\frac{1}{n!\tau}\langle(X(t+\tau)-X(t))^n\rangle|_{X(t)=X;\alpha}, \tag{3.4}$$

where X represents the lift and drag coefficients, α the fixed AOA, $D^{(1)}(X,\alpha)$ the drift function and $D^{(2)}(X,\alpha)$ the diffusion function. The drift function represents the deterministic part of the system and estimates the mean time derivative of the $X(t)$, whereas the diffusion function quantifies the amplitude of the stochastic fluctuations.

The direct estimation of $D^{(1)}(X,\alpha)$ and $D^{(2)}(X,\alpha)$ from equation (3.4) may suffer from different sources of errors like finite sampling deviations, additional measurement noise etc. [26, 27]. The Langevin equation (3.3) is mainly dependent on these two functions, which means quality of results strongly depend on the correct estimation of drift and diffusion functions. For this purpose, an optimization approach based on χ^2 test is applied on PDFs of the model and measured data. The χ^2 value is obtained as

$$\chi^2 = \sum_i \frac{(p_{model,i} - p_{measure,i})^2}{(p_{model,i} + p_{measure,i})}, \tag{3.5}$$

where p_{model} and $p_{measure}$ are the stationary PDFs of model and measured data, respectively. The χ^2 test quantifies the difference between the model and measured data sets. The lower the difference, the better the quality of the results. Since the Langevin equation (3.3) is random by nature due to involvement of the noise term, so it would be time consuming to get the stable values by numerical simulation. As an alternative, the stationary

PDF of the Langevin equation is used, which is known in its analytical form [23]

$$p(X_{model}) = \frac{N}{D^{(2)}(X_{model})} \exp\left[\int^{X_{model}} \frac{D^{(1)}(y)}{D^{(2)}(y)} dy\right], \tag{3.6}$$

where N is a normalization factor.

For best estimation of drift and diffusion functions in an automatic way, the optimization approach described in equation (3.5), is coupled with an interval sectioning procedure based on the inverse parabolic interpolation [1] algorithm [28]. The analytical expression for the algorithm is

$$x = b - \frac{1}{2}\frac{(b-a)^2[f(b)-f(c)] - (b-c)^2[f(b)-f(a)]}{(b-a)[f(b)-f(c)] - (b-c)[f(b)-f(a)]}, \tag{3.7}$$

where x is the abscissa value of new estimated point and accounts for diffusion function here. The corresponding ordinate value of this new point is the χ^2 value. The a, b, and c are the abscissa values of the three randomly selected points and $f(a)$, $f(b)$ and $f(c)$ are the respective ordinate values of the three points along the parabolic line. The algorithm works in a way that it discards one point after each iteration and decides for a new set of three points for next iteration like the point with minimum ordinate value is always in the middle of the three points. The algorithm continues for several iterations until the best value for x is obtained, thereafter stops functioning automatically as the points coincide with each other.

The basic model (equation (3.3)) has been extended to incorporate for additional effects to reproduce satisfactory conditional PDFs $p(X(t+\tau)|X(t))$ for all time lags τ. These additional effects include out of phase lift and drag coefficients oscillation and the amplitude modulation (breathing) observed in the lift and drag coefficients time series. The extended model reads [29]

$$X_{model}(k) = X_{Langevin}(k) + A\sin\left(\frac{2\pi k}{T}\right)\exp\left[\left(\frac{-k'}{k_o}\right)^S\right], \tag{3.8}$$

where $X_{Langevin}$ is the result obtained from equation (3.3), A the constant to fix the oscillation amplitude for lift and drag coefficients, k the discrete time variable and T the most dominant oscillation period observed in the measured data time series. The exponential function in the equation controls the amplitude modulation of the oscillation along the lift and drag time

[1] Basically it is a parabolic interpolation, since purpose here is to find out an abscissa rather than an ordinate; thus, from technical point of view, the method is termed as an inverse parabolic interpolation [28].

series, where k_o is half the length of average breathing, $k' = (k \bmod ko)$ and S is described as

$$S = \begin{cases} +1, & \text{for } (2n)k_o < k \leq (2n+1)k_o \\ -1, & \text{for } (2n+1)k_o < k \leq 2(n+1)k_o, \end{cases} \tag{3.9}$$

where $n = 0, 1, 2, 3....$

To correct for extension in equation (3.8), once again an optimization approach is repeated. This time the stationary PDFs for model used in equation (3.5) are taken from results of equation (3.8), and the final obtained value of χ^2 is compared with intrinsic standard error to verify the quality of results. The relation for intrinsic standard error reads [2]

$$S_{Error} = \sum_i \frac{\sqrt{N_i}}{N_{Total}}, \tag{3.10}$$

where N_i is the number of counts in the i^{th} bin and N_{Total} the size of the sample. For the best quality of the model, the χ^2 value is to be in order or less (in magnitude) than the standard error. Further details of the described model can be found in [29].

3.3 Estimation of the rotor normal and tangential forces

The rotor normal and tangential forces are estimated for a blade element using the classical and stochastic BEM approaches. In classical BEM the static airfoil data table (which contains mean lift and drag coefficients as function of AOA obtained by measurements) is used as an input, whereas in stochastic BEM the model equation (3.8) is integrated into BEM. The BEM model taken here is described in following section.

3.3.1 BEM model

The rotor blade element forces are estimated with a well-accepted standard BEM model used in aerodynamic model AeroDyn of the National Renewable Energy Laboratory [19]. To determine the aerodynamic forces, it is necessary to first calculate the inflow angle to obtain the effective AOA on the rotating blade element. The expressions in this context are [19, 30]

$$tan\phi = \frac{V(1-a)}{\omega r(1+\acute{a})} = \frac{(1-a)}{\lambda_r(1+\acute{a})}, \quad \lambda_r = \frac{\omega r}{V} \tag{3.11}$$

$$V_{Total} = \sqrt{V^2(1-a)^2 + \omega^2 r^2 (1+\acute{a})^2}, \tag{3.12}$$

$$\alpha = \phi - \theta, \tag{3.13}$$

where ϕ is the flow angle, v the relative speed, α the AOA and θ the pitch angle. The flow angle ϕ is the angle between the relative speed and plane of the rotation, whereas the AOA α is the angle between the relative speed and chord of the blade element. The parameter V is the mean upstream wind velocity, ω the blade rotational speed and r the local radius of the blade element. The λ_r is the local tip speed ratio (TSR), whereas the a and $\acute{a}$ are the axial and tangential induction factors, respectively. The a is the amount of reduction in axial wind speed when approaching the blade and $\acute{a}$ the amount of rotational acceleration to blade because of the induced wake rotation. The terms $V(1-a)$ and $\omega r(1+\acute{a})$ are the effective axial wind and tangential blade speeds, respectively.

Once the v, ϕ and α are estimated, the thrust and torque distribution around an annulus having width dr can be calculated as

$$dT = \frac{1}{2} B \rho v^2 C_n c(r) dr, \tag{3.14}$$

$$dQ = \frac{1}{2} B \rho v^2 C_t c(r) r dr, \tag{3.15}$$

where dT and dQ are the thrust and torque produced by the element in the annulus, B the number of blades, ρ the air density and $c(r)$ the local chord length. The C_n and C_t are the normal and tangential force coefficients, which can be estimated from the relations

$$C_n = C_L cos\phi + C_D sin\phi, \tag{3.16}$$

$$C_t = C_L sin\phi - C_D cos\phi, \tag{3.17}$$

where C_L and C_D are the lift and drag coefficients, which are taken as function of α either from static airfoil data table (in case of classical BEM) or estimated through model equation (3.8) (in case of stochastic BEM).

To initialize the algorithm, induction factors can be guessed in start, which in our case are taken as $a = \frac{1}{3}$ and $\acute{a} = 0$. Later, the algorithm finds true values by iterative process using the relations given below. The axial induction factor is calculated by either relation suggested in basic BEM or modified Glauert correction model [31]. The basic BEM theory is effective up to axial induction factor of 0.4, which in other words up to thrust coefficient of 0.96. This assigns an upper limit for the validity of basic BEM theory. Beyond this point, the wake breaks down and turbulent mixing occurs leading to highly transient and unpredictable state. In this state, the far

wake propagates towards the upstream and causes an increase in turbulence violating the basic assumptions of the BEM theory. This causes deceleration of the flow behind the rotor, but the thrust continues to increase on the rotor [19]. To counter balance for this effect, Buhl [31] introduced a relation by modifying Glauert correction model [32] to compute for axial induction factor when $a > 0.4$. Higher axial induction means higher loading on the blade and vice versa. The loading condition in this context can be determined by

$$C_T = 1 + \frac{\sigma(1-a)^2 C_n}{sin^2\phi}, \quad \sigma = \frac{Bc(r)}{2\pi r} \tag{3.18}$$

where C_T is the thrust coefficient used in equation (3.19) to estimate the axial induction factor by modified Glauert correction model and σ the local solidity. When $C_T > 0.96F$ (for F see equation (3.23)), the blade element is said to be highly loaded and the new axial induction factor will be estimated using modified Glauert correction model. Otherwise, in case of $C_T \leq 0.96F$, the basic BEM method will be applied to estimate the axial induction factor. The relations used to calculate the true axial and tangential induction factors read

$$a = \begin{cases} \frac{18F-20-3\sqrt{C_T(50-36F)+12F(3F-4)}}{36F-50}, & \text{if } C_T > 0.96F \\ \left[1+\frac{4Fsin^2\phi}{\sigma C_n}\right]^{-1}, & \text{if } C_T \leq 0.96F \end{cases} \tag{3.19}$$

$$\acute{a} = \left[-1 + \frac{4Fsin\phi cos\phi}{\sigma C_t}\right]^{-1}, \tag{3.20}$$

where F is the loss factor that represents the tip and root losses in combination, which can be evaluated as

$$F_{Tip} = \frac{2}{\pi} cos^{-1} \exp\left[-\frac{B}{2}\frac{R_{Tip}-r}{rsin\phi}\right], \tag{3.21}$$

$$F_{Root} = \frac{2}{\pi} cos^{-1} \exp\left[-\frac{B}{2}\frac{r-R_{Root}}{rsin\phi}\right], \tag{3.22}$$

$$F = F_{Tip} F_{Root}. \tag{3.23}$$

The set of equations described in this section are iteratively solved for estimation of true axial and tangential induction factors. The process is repeated continuously (starting from equation (3.11)) until the condition expressed in equation (3.25) is fulfilled.

$$\begin{aligned} dif &= |a_{new} - a_{old}| \\ d\acute{i}f &= |\acute{a}_{new} - \acute{a}_{old}|, \end{aligned} \tag{3.24}$$

$$Condition \Rightarrow \begin{cases} Continue, & \text{if } Tol < dif \text{ and } d\acute{i}f \\ Stop, & \text{if } Tol \geq dif \text{ and } d\acute{i}f, \end{cases} \tag{3.25}$$

where Tol is the acceptable tolerance. The calculation converges to a tolerance value of 10^{-5} in our case.

3.4 Results

The results are presented for the rotor normal and tangential force coefficients acting on a blade element achieved with the classical and stochastic BEM approaches. The force coefficients are obtained for AOAs $0-25^{\circ}$ using equations (3.16-3.17). This is done by varying TSR to change the inflow angle. The blade element is assumed to rotate at a local radius of $r = 10$ m and pitch angle $\theta = 3^{\circ}$. The local chord length and annular thickness are taken as $c(r) = 0.2$ m and $dr = 0.8$ m, respectively. Moreover, at this preliminary stage, the root and tip losses are ignored, i.e. $F = 1$.

The results for the normal and tangential force coefficients are summarized in Figures 3.2-3.3, respectively. The Figure 3.2(a) and Figure 3.3(a) show the $C_{n,static}$ and $C_{t,static}$ curves as function of AOA obtained with classical BEM. The Figure 3.2(b) and Figure 3.3(b) represent the $C_{n,model}$ and $C_{t,model}$ curves with local dynamics as function of AOA obtained with stochastic BEM.

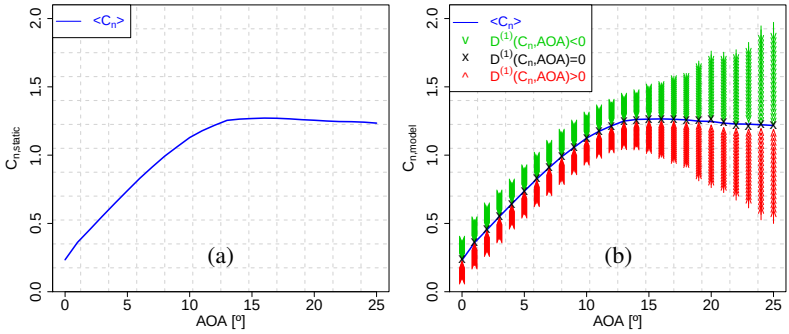

Figure 3.2: Normal force coefficient curves (color online). (a) $C_{n,static}$ curve obtained with classical BEM. (b) $C_{n,model}$ curve with local dynamics obtained with stochastic BEM. The solid blue line represents the mean $C_{n,model}$ curve. The red and green arrows demonstrate the positive and negative drift function for $C_{n,model}$ trying to move towards the stable fix points; the black crosses, where drift function is zero.

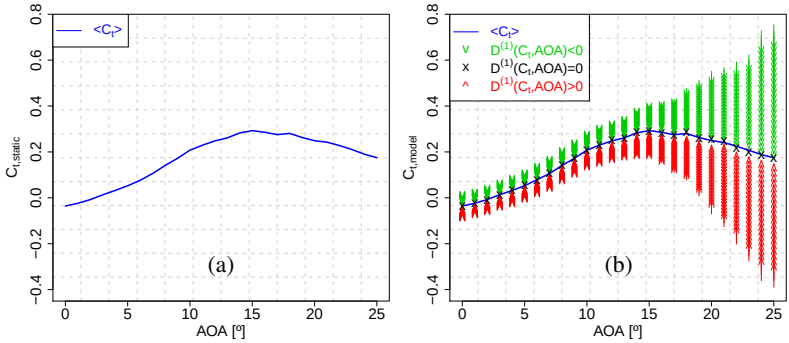

Figure 3.3: Tangential force coefficient curves (color online). (a) $C_{t,static}$ curve obtained with classical BEM. (b) $C_{t,model}$ curve with local dynamics obtained with stochastic BEM. The solid blue line represents the mean $C_{t,model}$ curve. The red and green arrows demonstrate the positive and negative drift function for $C_{t,model}$ trying to move towards the stable fix points; the black crosses, where drift function is zero.

In Figure 3.2(b) and Figure 3.3(b), the drift function obtained with equation (3.4) presents the full map of the local dynamics of the normal and tangential force coefficients for each AOA. Where, the red arrows display the deterministic increase of the normal and tangential force coefficients over the time and the green arrows display the deterministic decrease of same parameters over the time. The black crosses represent the stable fix points where drift function is zero matching the usual mean normal and tangential force coefficient curves. The curves consisting of stable fix points could be called the Langevin normal and tangential force coefficient curves based on the approach used.

The comparison of the classical and stochastic BEM approaches in terms of their contributed results in Figures 3.2-3.3 demonstrate that the classical BEM based on static tabulated airfoil data only provides the mean normal and tangential forces. In comparison to this, the BEM integrated with stochastic model brings additional insight by expressing complete map of the local force dynamics over the time. The mean curves of the normal and tangential force local dynamics show very good agreement with the mean curves obtained with the classical BEM. The Langevin force coefficient curves match almost perfectly with the mean curves of the normal and tangential force local dynamics.

3.5 Conclusions

A stochastic lift and drag model has been integrated into a standard BEM model to achieve the dynamic forces on a rotating blade element. The forces are obtained with local dynamics for AOAs $0 - 25^{\circ}$.

The comparison of the classical and stochastic BEM approaches demonstrate that the stochastic BEM brings additional insight by expressing complete map of the local force dynamics over the time. The classical BEM only provides the mean forces. The mean curves of the local force dynamics show very good agreement with the mean curves obtained with the classical BEM. The Langevin force curves shown in black crosses match almost perfectly with the mean curves of the local force dynamics.

The model is being developed to extract and provide the complete local loading information on the wind turbine blades, which could lead to an optimum rotor design under turbulent wind circumstances. The final goal is to achieve an aerodynamic model like AeroDyn [19] based on stochastic approach. Later, it could be combined with a wind energy converter model like FAST [33] or similar other model to obtain a stochastic rotor model.

The authors would like to thank Jörge Schneemann for access to his measured data. Also we would like to thank the referees for their helpful comments and suggestions for improvement of the paper.

Bibliography

[1] J. G. Leishman. Challenges in modeling the unsteady aerodynamics of wind turbines. *Wind Energy*, 5:85–132, September 2002.

[2] A. Morales, M. Wächter and J. Peinke. Characterization of wind turbulence by higher order statistics. *Wind Energy*, 15(3):391–406, April 2012.

[3] F. Böttcher, S. Barth and J. Peinke. Small and large scale fluctuations in atmospheric wind speeds. *Stochastic Environmental Research and Risk Assessment*, 12:299–308, 2007.

[4] H. Long, J. Wu, F. Mattew and P. Tavner. Fatigue analysis of wind turbine gearbox bearings using SCADA data and Miner's rule. *Scientific Proceedings of EWEA*, Brussels, Belgium, 2011.

[5] T. Mücke, D. Kleinhans and J. Peinke. Atmospheric turbulence and its influence on the alternating loads on wind turbines. *Wind Energy*, 14:301–316, 2011.

[6] J. L. Tangler and D. M. Somers. NREL Air Foil Families for HAWT's. *Scientific Proceedings of AWEA*, Washington DC, USA, January, 1995.

[7] P. Fuglsang, I. Antoniou, K. S. Dahl and H. A. Madsen. *Wind tunnel tests of the FFA-W3-241, FFA-W3-301 and NACA 63-430 airfoils*. Scientific report Risø-R-1041(EN), Risø National Laboratory, Denmark, December 1998.

[8] P. Fuglsang, K. S. Dahl and I. Antoniou. *Wind tunnel tests of the Risø-A1-18, Risø-A1-21 and Risø-A1-24 airfoils*. Scientific report Risø-R-1112(EN), Risø National Laboratory, June 1999.

[9] W. A. Timmer and R. P. J. O. M. van Rooij. Summary of the Delft University wind turbine dedicated airfoils. *Journal of Solar Energy Engineering, Transactions ASME*, 125:488–496, 2003.

[10] D. M. Eggleston and F. S. Stoddard. *Wind turbine engineering design*. Van Nostrand Reinhold Company, New York, USA, July 1987.

[11] J. G. Leishman. *Principles of Helicopter Aerodynamics, Second Edition*. Cambridge University Press, Cambridge, New York, USA, 2006.

[12] G. Wolken-Möhlmann, P. Knebel, S. Barth and J. Peinke. Dynamic lift measurements on a FX79W151A airfoil via pressure distribution on the wind tunnel walls. *Journal of Physics: Conference Series*, 75: 012026, 2007.

[13] T. Sant. *Improving BEM-based Aerodynamic Models in Wind Turbine Design Codes*. PhD thesis, Delft University Wind Energy Research Institute (DUWIND), the Netherlands, 2007.

[14] L. J. Vermeer, J. N. Sørensen and A. Crespo. Wind turbine wake aerodynamics. *Progress in Aerospace Sciences*, 39:467–510, August–October 2003.

[15] A. T. Conlisk. Modern Helicopter Rotor Aerodynamics. *Progress in Aerospace Sciences*, 37:419–476, 2001.

[16] H. Snel. Review of the present status of rotor aerodynamics. *Wind Energy*, 1:46–69, April 1998.

[17] K. Åhlund. *Investigation of the NREL NASA/Ames Wind Turbine Aerodynamics Database*. Scientific report FOI-Rñ1243ñSE, Swedish Defence Research Agency, Stockholm, Sweden, June 2004.

[18] M. O. L. Hansen and H. A. Madsen. Review Paper on Wind Turbine Aerodynamics. *Journal of Fluids Engineering*, 133:114001, 2011.

[19] P. J. Moriarty and A. C. Hansen. *AeroDyn Theory Manual*. Technical report NREL/EL-500-36881, National Renewable Energy Laboratory, Golden, Colorado, USA, January 2005.

[20] G. A. Weinzierl. *A BEM Based Simulation-Tool for Wind Turbine Blades with Active Flow Control Elements*. Diploma thesis, Technical University of Berlin, Germany, April 2011.

[21] R. E. Seoud and J. C. Vassilicos. Dissipation and decay of fractal-generated turbulence. *Physics of Fluids*, 19:105108, 2007.

[22] J. Schneemann, P. Knebel, P. Milan and J. Peinke. Lift measurements in unsteady flow conditions. *Scientific Proceedings of EWEC*, Warsaw, Poland, 2010.

[23] H. Risken. *The Fokker-Planck Equation, Second Edition*. Springer, Berlin, Germany, 1996.

[24] S. Siegert, R. Friedrich and J. Peinke. Analysis of data sets of stochastic systems. *Physics Letters A*, 243:275–280, 1998.

[25] A. N. Kolmogorov. Über die analytischen methoden in der wahrscheinlichkeitsrechnung. *Mathematische Annalen*, 140:415–458, 1931.

[26] J. Gottschall and J. Peinke. On the definition and handling of different drift and diffusion estimates. *New Journal of Physics*, 10:083034, 2008.

[27] F. Böttcher, J. Peinke, D. Kleinhans, R. Friedrich, P. G. Lind and M. Haase. Reconstruction of Complex Dynamical Systems Affected by Strong Measurement Noise. *Physical Review Letters*, 97:090603, 2006.

[28] W. H. Press, S. A. Teukolsky, W. T. Vetterling and B. P. Flannery. *Numerical Recipes in C The art of scientific computing*. Cambridge University Press, New York, USA, 1992.

[29] M. R. Luhur, M. Wächter and J. Peinke. Stochastic Modeling of Lift and Drag Dynamics under Turbulent Conditions. *Scientific Proceedings of EWEA*, Copenhagen, Denmark, 2012.

[30] T. Burton, D. Sharpe, N. Jenkins and E. Bossanyi. *Wind Energy Handbook, Second Edition*. John Wiley & Sons, Chichester, UK, 2011.

[31] M. L. Buhl Jr. *A new empirical relationship between thrust coefficient and induction factor for the turbulent windmill state*. Technical report NREL/TP-500-36834, National Renewable Energy Laboratory, Golden, Colorado, USA, August 2005.

[32] H. Glauert. *A General Theory of the Autogyro, Volume 1111 of Reports and Memoranda Edition*. British ARC, UK, 1926.

[33] J. M. Jonkman and M. L. Buhl Jr. *FAST User's Guide*. Technical report NREL/EL-500-38230, National Renewable Energy Laboratory, Golden, Colorado, USA, August 2005.

Chapter 4

Stochastic model integration into AeroDyn

The content presented in this chapter is submitted as "M. R. LUHUR, J. PEINKE, M. KÜHN and M. WÄCHTER. Stochastic model for aerodynamic force dynamics on wind turbine blades in unsteady wind inflow, *Journal of Computational and Nonlinear Dynamics*, 2014". Here, Footnotes 1-3 and Sections 4.6-4.7 are added for additional information to the reader, which are not included in the submitted paper.

Abstract The paper presents a stochastic approach to estimate the aerodynamic forces with local dynamics on wind turbine blades in unsteady wind inflow. This is done by integrating a stochastic model of lift and drag dynamics for an airfoil into the aerodynamic simulation software AeroDyn. The model is added as an alternative to the static table lookup approach in blade element momentum (BEM) wake model used by AeroDyn. The stochastic forces are obtained for a rotor blade element using full field turbulence simulated wind data input and compared with the classical BEM and dynamic stall models for identical conditions. The comparison shows that the stochastic model generates additional extended dynamic response in terms of local force fluctuations. Further, the comparison of statistics between the classical BEM, dynamic stall and stochastic models' results in terms of their increment probability density functions gives consistent results.

4.1 Introduction

Wind energy being safe, significant and fundamental for economical as well as social development is getting great interest and successfully penetrating the energy market today. According to Global Wind Energy Council 2012

projections, the power generation from wind is expected to reach twice the present global installed capacity by the end of 2017 [1].

In the success of modern wind energy, aerodynamic research has a significant role [2]. The aerodynamic models for wind turbines are used to study the acting loads on rotor blades in response to wind inflow. At present, various engineering as well as computational fluid dynamics (CFD) models exist to foresee the performance of wind turbines. In computational terms, the investigations suggest wide choice of engineering methods in particular the well-known blade element momentum (BEM) method [3, 4]. The high fidelity CFD is yet extremely costly [3] and needs faster and bigger memory computers to achieve acceptable computational efficiency [5]. For distributed loads on wind turbine rotor blades, the aerodynamic models are combined with dynamic analysis codes such as FAST [6], YawDyn [7], ADAMS/WT [8], SIMPACK [9], DHAT [10], FLEX5 [11] etc. The aerodynamic models used by these dynamic analysis codes or other similar codes are fundamentally based on simple lookup tables, which contain mean static characteristics for an airfoil at constant angles of attack (AOAs) [12, 13] and disregard the information on system local dynamics. Even the dynamic models such as Beddoes-Leishman dynamic stall model use static airfoil coefficients which are modified according to AOA and its rate of variation and mostly disobey the local force dynamics.

In this contribution, a new concept based on a stochastic approach has been integrated into the aerodynamic model AeroDyn [12] as an alternative to traditional table lookup method used by the classical BEM model. The concept represents a stochastic lift and drag model, which provides the lift and drag forces with local dynamics under unsteady wind inflow conditions. The model estimates the lift and drag coefficients numerically based on the local AOA [14]. The proposed approach thus is a stochastic alternative to the classical BEM and Beddoes-Leishman dynamic stall models.

The scope of this paper is to prove the concept by integrating the stochastic model into AeroDyn and showing that the newly developed concept extracts more load information on rotor blades compared to traditional approaches. A future aim is to achieve a complete stochastic rotor model, which could provide the full local loading information on blades in a stochastic sense, leading to an optimum rotor design. Such aerodynamic model could be combined with a wind energy converter (WEC) model to obtain a stochastic rotor model. It is necessary to mention here that this contribution is a primary step towards the final goal and for simplicity reasons disregards the tower shadow and other related effects at this stage.

The paper is structured such that Section 4.2 provides a short introduction to the AeroDyn, the input files and the elemental forces. Section

4.3 introduces the stochastic lift and drag model. Section 4.4 presents the stochastic model integration into AeroDyn and the results achieved by classical BEM, dynamic stall and stochastic model. The final Section 4.5 summarizes the outcome and outlook of the work.

4.2 AeroDyn

AeroDyn is an add-in software consisting a set of routines to execute aerodynamic computations for horizontal axis wind turbines (HAWTs). It can be interfaced with number of dynamic analysis codes in particular with FAST, SymDyn, YawDyn and ADAMS/WT to carry out the aeroelastic simulations. These aeroelastic simulation codes differ only in structural dynamics, the aerodynamic calculations are identical for them. AeroDyn has no stand alone executable functionality and is invoked by a dynamic analysis code. However, its separate aerodynamic forces output file for any element can be obtained by setting an option from "NOPRINT" to "PRINT" in AeroDyn primary input data file [15]. It creates one output file in one simulation time for one selected blade element only.

AeroDyn requires information about wind turbine geometry, blade element velocity, element location, airfoil aerodynamic data, operating conditions and wind input [12]. Based on given information, it computes the corresponding elemental aerodynamic forces and delivers to the aeroelastic simulation program to estimate the distributed forces on wind turbine blades. AeroDyn uses different models to perform aerodynamic calculations for aeroelastic simulations of HAWTs; however, for current computations, the BEM and dynamic stall models are used. The BEM model is a well-known classical approach used by different wind turbine designers with various corrections, whereas the dynamic stall model is based on the semi-empirical Beddoes-Leishman model which is especially important for yawed wind turbines. A detailed description of the classical BEM and dynamic stall models used for present computations can be found in *Moriarty and Hansen* [12]. The BEM model is used for estimation of the steady forces (with static table lookup approach) and the stochastic forces (with stochastic model addition).

4.2.1 AeroDyn input files

AeroDyn requires three input files to perform the aerodynamic calculations. These are, the primary data file, the airfoil data file and the wind file. Latter two are called through paths provided in primary data file. The primary

data file consists of different options of models for calculation of flow influence. Additionally, it carries the information on wind reference height (hub height), convergence tolerance for induction factors, air density, kinematic air viscosity, time interval for aerodynamic calculations, and the number of blade elements per blade. For each blade element it is provided with the location, twist, span and chord length. For more clarity of the element related parameters; see blade segment terminology given in Figure 4.1.

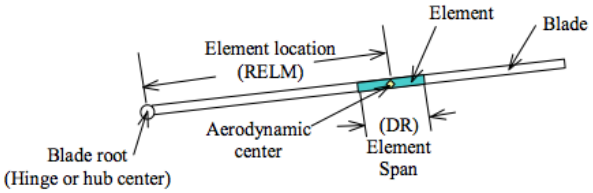

Figure 4.1: Blade segment nomenclature. Taken from [15].

The airfoil data file[1] contains two dimensional static airfoil characteristics. It carries lift, drag and pitching moment (optional) coefficients for range of AOAs. Besides, it comprises some additional parameters pertaining to dynamic stall model. The airfoil characteristics for intermediate AOAs are obtained by linear interpolation.

The wind files in AeroDyn are used in two formats, one the hub-height wind and other the full field turbulence, which are created by either measurements or simulations. The hub-height wind files are the simple ones containing either steady or time varying wind data. The full field turbulence is generated by TurbSim program [16, 17], which creates two files, one the binary wind data file and other the summary file. The created wind data corresponds to all three wind components changing in time and space. The wind is sampled at frequency of 20 Hz and the turbulence is generated by a square grid spread over the whole rotor area. The velocity components at each point of the square grid are provided as function of time. The components of velocity at each blade element are obtained with linear interpolation (in terms of averaging or smoothing) in time and space[12]. For more details; see [16, 17].

[1] In AeroDyn, for each element, a different (own) airfoil data file can also be used, which results in varying sectional properties along the blade span. However, it is necessary that all blades in rotor should have identical aerodynamics. Additionally, AeroDyn also allows the use of multiple airfoil data tables (containing in one file) for a blade element by using one optional parameter (such as local element Reynolds number, flap or aileron setting) in addition to AOA. This optional parameter is defined by the user [12].

4.2.2 Elemental forces

To determine the elemental forces on a rotating blade, the BEM method is applied on blade section as shown in Figure 4.2. The illustration shows the local velocities with flow angles and the acting forces on the element.

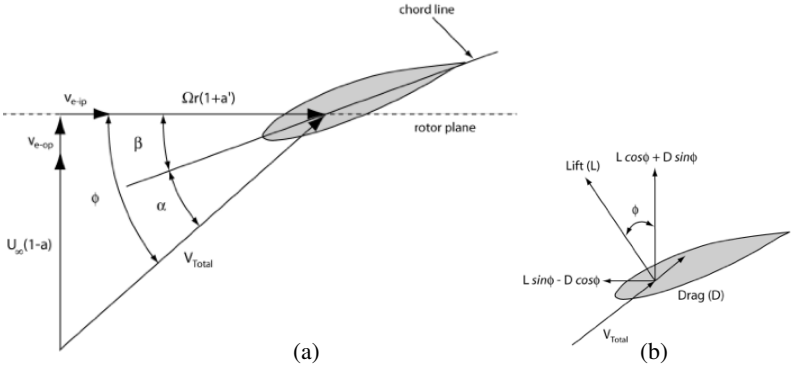

Figure 4.2: Scheme of force components on blade section. Angles are related to the plane of rotation. (a) Local velocities and flow angles on blade element and (b) local forces on blade element. Taken from [12].

In Figure 4.2(a), ϕ represents the flow angle, V_{Total} the relative speed, α the AOA and β the combination of pitch and twist angles. The flow angle ϕ is the angle between the relative speed and the plane of rotation, whereas the AOA α is the angle between the relative speed and the chord of the blade element. The parameter U_∞ denotes the free stream wind velocity, Ω the blade rotational speed and r the local radius of the blade element. The variables v_{e-op} and v_{e-ip} are the out-of-plane and in-plane element velocities, respectively, originating from blade structural deflections under pronounced rotation. When the blade rotational speed is very small, the latter velocities are ignored.

The terms $U_\infty(1-a)$ and $\Omega r(1+\acute{a})$ are the effective axial wind and tangential blade speeds, respectively. The parameters a and $\acute{a}$ are the axial and tangential induction factors, where a represents the amount of reduction in axial wind speed when approaching the blade and $\acute{a}$ the amount of rotational acceleration to the blade caused by induced wake rotation opposite to the rotor rotation [18].

The induction factors are estimated using an iterative process described in the flow chart Figure 4.3. After initialization, the algorithm iteratively finds values fulfilling the condition expressed for *Tol*. The parameter *Tol* is an acceptable tolerance allowed around the true values of axial and tan-

gential induction factors. The process repeats for each element. Once the induction factors, inflow angles and AOAs converged to their final values, the acting forces are estimated for the element.

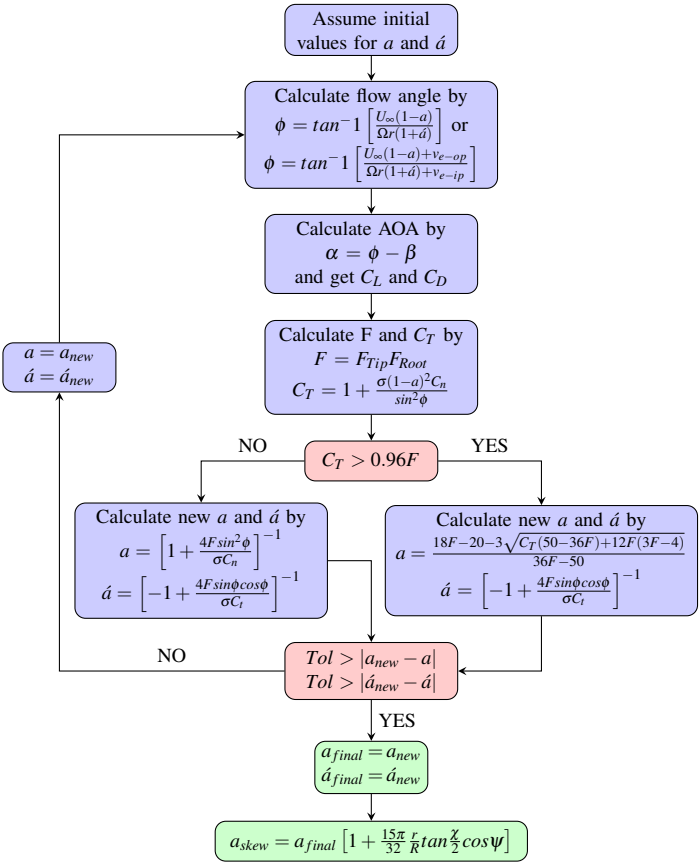

Figure 4.3: Flow chart to iterate for induction factors.

In flow chart Figure 4.3, the function F represents the tip and root loss correction factors[2] in combination, C_T the thrust loading on the element, σ the local solidity of the rotor, C_n the normal force coefficient and C_t

[2]For estimation of tip and root losses, AeroDyn uses Prandtl's model [20], where $F_{Tip} = \frac{2}{\pi}cos^{-1}\exp\left[-\frac{B}{2}\frac{R_{Tip}-r}{rsin\phi}\right]$ and $F_{Root} = \frac{2}{\pi}cos^{-1}\exp\left[-\frac{B}{2}\frac{r-R_{Root}}{rsin\phi}\right]$. By introducing Prandtl's correction model into BEM, reasonable accuracy can be achieved for most of the operating conditions. However, still it has limitations as the Prandtl's calculations are limited to optimum and stationary conditions. It ignores the wake expansion, which limits its validity for lightly loaded rotors. For definition of tip and root losses; see Section 4.6.

the tangential force coefficient. The parameter a_{skew} is the local element induction factor for skewed wake[3], R the blade radius, χ the wake angle and ψ the blade azimuth angle[4]. For more details and derivations of the relations given in flow chart Figure 4.3; see [12, 18, 19, 20, 21, 22, 23, 24, 25, 26].

4.3 Stochastic lift and drag model

A stochastic model of the lift and drag dynamics has been developed for an advanced characterization of forces on wind turbine airfoils under unsteady wind inflow. The model parameters are derived from dynamic measurements of lift and drag forces performed for FX 79-W-151A airfoil in a wind tunnel. The turbulent inflow with intensity of 4.6% was generated using a fractal square grid, which produces the flow with typical intermittent velocity fluctuations commonly known for free field wind situations; see [14]. The model extracts most of the information available in the system dynamics in terms of a dynamic response. The model reads [14]

$$X_{model}(k) = X_{langevin}(k) + A\sin\left(\frac{2\pi k}{T}\right)\exp\left[\left(\frac{-k'}{k_o}\right)^S\right], \tag{4.1}$$

where the first part of the equation represents the basic model and the second the extension which accounts for the oscillation effects with amplitude modulation (breathing) contained in the lift and drag time series. The parameter X represents the lift and drag coefficients, A the constant to fix the oscillation amplitude for lift and drag coefficients, k the discrete time variable and T the most dominant oscillation period of lift and drag coefficients. The exponential function in equation (4.1) controls the breathing of oscillation along the lift and drag time series, where k_o is half the average breathing length, $k' = (k \bmod k_o)$ and S is described as

$$S = \begin{cases} +1, & \text{for } (2n)k_o < k \leq (2n+1)k_o \\ \\ -1, & \text{for } (2n+1)k_o < k \leq 2(n+1)k_o, \end{cases} \tag{4.2}$$

where $n = 0, 1, 2, \ldots$.

The basic model $X_{langevin}(k)$ in equation (4.1) corresponds to a first order stochastic differential equation termed as Langevin equation, cf.[27],

[3] For more information on skewed wake effect; see Section 4.7

[4] The azimuth angle describes the blade angular position in one cycle measured in clockwise direction such that it is zero when the blade is pointing vertically downwards.

expressed in discrete form as

$$X(k+\tau) = X(k) + \tau D^{(1)}(X,\alpha) + \sqrt{\tau \tilde{F} D^{(2)}(X,\alpha)}\,\Gamma(k), \tag{4.3}$$

where $D^{(1)}(X,\alpha)$ and $D^{(2)}(X,\alpha)$ are the drift and diffusion functions, also known as first and second Kramers-Moyal coefficients. Here τ is the integration time step and α the mean AOA that varies slowly compared to the fluctuations caused by turbulent inflow conditions. The parameter $\tilde{F}$ is the correction factor for diffusion function to incorporate the model extension and $\Gamma(k)$ the Gaussian white noise termed as Langevin force [27] with mean value $\langle\Gamma(k)\rangle = 0$ and variance $\langle\Gamma^2(k)\rangle = 2$.

The $D^{(1)}(X,\alpha)$ reflects the deterministic part of the system, whereas $D^{(2)}(X,\alpha)$ quantifies the amplitude of the stochastic fluctuations. These functions for lift and drag coefficients are parameterized as [14]

$$D^{(1)}(X,\alpha) = m(X - X_o), \tag{4.4}$$

$$D^{(2)}(X,\alpha) = \beta. \tag{4.5}$$

Here m is the slope of drift function, X the lift or drag coefficient, X_o the stable fix point in X where drift function is zero and β the constant diffusion function. The optimized values for these parameters as function of mean AOAs are given in Tables 4.1 and 4.2. The intermediate values can be obtained by linear interpolation. For more details and validation of the model; see [14].

4.4 Model integration into AeroDyn

The stochastic lift and drag model described in Section 4.3 is integrated into AeroDyn to obtain aerodynamic forces with local dynamics on the rotating blade. The model is added in form of a routine based on model equation (4.1) as an alternate to static airfoil data files used by the classical BEM model in AeroDyn. The characteristics of model related parameters given in Tables 4.1 and 4.2 are imported as input files to the model routine. The axial and tangential induction factors are estimated (using mean lift and drag coefficients) through an iterative procedure described in Figure 4.3.

4.4.1 Numerical setup

Before starting the aerodynamic computations, the AeroDyn input files described in Section 4.2.1 are set up for intended options of computations. In

Table 4.1: C_L model parameters for AOAs 0° to 30°. The parameter m is the slope of drift function, C_{Lo} the stable fix point, β the optimized diffusion function, $\tilde{F}$ the correction factor for diffusion function to incorporate the model extension, A the constant to fix the oscillation amplitude, T the most dominant oscillation period and k_o half the average breathing length.

AOA	m	C_{Lo}	β	$\tilde{F}$	A	T	k_o
0°	−0.160	0.228	$2.50e-04$	0.329	0.092	30	300
1°	−0.160	0.355	$3.17e-04$	0.329	0.105	30	300
2°	−0.157	0.450	$3.32e-04$	0.330	0.109	30	300
3°	−0.156	0.547	$3.23e-04$	0.329	0.107	30	300
4°	−0.150	0.641	$2.90e-04$	0.329	0.101	30	300
5°	−0.155	0.735	$3.31e-04$	0.329	0.107	30	300
6°	−0.154	0.827	$3.59e-04$	0.330	0.113	30	300
8°	−0.142	0.996	$3.50e-04$	0.330	0.115	30	300
9°	−0.143	1.069	$3.37e-04$	0.330	0.114	30	300
10°	−0.140	1.141	$3.05e-04$	0.329	0.108	30	300
11°	−0.138	1.194	$3.14e-04$	0.330	0.113	30	300
12°	−0.126	1.236	$3.06e-04$	0.329	0.114	29.9	300
13°	−0.117	1.272	$3.12e-04$	0.498	0.104	29.75	300
14°	−0.114	1.286	$3.72e-04$	0.500	0.113	29.9	305
15°	−0.107	1.289	$4.84e-04$	0.500	0.136	30	300
16°	−0.115	1.286	$6.58e-04$	0.500	0.154	30.25	300
17°	−0.118	1.278	$9.21e-04$	0.500	0.175	30.5	305
18°	−0.121	1.270	$1.26e-03$	0.500	0.199	30.75	300
19°	−0.120	1.249	$1.81e-03$	0.330	0.290	31.25	300
20°	−0.125	1.238	$2.25e-03$	0.330	0.318	31.33	300
21°	−0.130	1.218	$3.03e-03$	0.330	0.348	32.5	300
22°	−0.129	1.199	$3.51e-03$	0.330	0.378	32.5	300
23°	−0.133	1.184	$4.41e-03$	0.330	0.415	32.5	300
24°	−0.136	1.164	$5.26e-03$	0.329	0.450	32.33	300
25°	−0.136	1.146	$5.39e-03$	0.330	0.460	32.35	300
26°	−0.142	1.122	$5.53e-03$	0.329	0.452	32.5	300
27°	−0.143	1.092	$4.35e-03$	0.329	0.410	32.15	300
28°	−0.144	1.053	$3.76e-03$	0.329	0.376	32	290
29°	−0.144	1.015	$2.49e-03$	0.329	0.302	31.8	285
30°	−0.148	0.983	$2.17e-03$	0.329	0.282	31.45	325

primary file the wind reference height, air density and air kinematic viscosity are taken as 42.7 m, 1.225 kg/m^3 and 1.464e^{-5} m^2/s, respectively.

The aerodynamic calculations are performed for a three-bladed rotor having radius of 13.76 m. The blade is divided into 10 equal segments along the radius. The local design specifications for each element are given in Table 4.3 containing the element nodal radius (from blade hub centre to the centre of element), twist angle, span and chord length. All three blades have the same distribution yielding identical aerodynamics for same pitch

Table 4.2: C_D model parameters for AOAs 0° to 30°. The parameter m is the slope of drift function, C_{Do} the stable fix point, β the optimized diffusion function, $\tilde{F}$ the correction factor for diffusion function to incorporate the model extension, A the constant to fix the oscillation amplitude, T the most dominant oscillation period and k_o half the average breathing length.

AOA	m	C_{Do}	β	$\tilde{F}$	A	T	k_o
0°	−0.171	0.052	$1.79e-05$	0.33	0.024	16	50
1°	−0.190	0.054	$1.67e-05$	0.33	0.022	16	48
2°	−0.196	0.055	$1.79e-05$	0.329	0.022	17	50
3°	−0.190	0.056	$1.90e-05$	0.33	0.023	17	50
4°	−0.192	0.058	$2.12e-05$	0.33	0.024	17.5	100
5°	−0.192	0.060	$2.24e-05$	0.33	0.025	18	105
6°	−0.197	0.060	$2.55e-05$	0.33	0.026	18.5	90
7°	−0.203	0.065	$2.86e-05$	0.23	0.030	23.8	95
8°	−0.200	0.068	$3.20e-05$	0.23	0.031	23.85	120
9°	−0.206	0.072	$3.56e-05$	0.23	0.032	23.85	120
10°	−0.206	0.077	$3.89e-05$	0.23	0.034	23.85	95
11°	−0.200	0.083	$4.19e-05$	0.23	0.036	23.9	210
12°	−0.198	0.092	$4.50e-05$	0.23	0.038	23.9	210
13°	−0.192	0.108	$4.89e-05$	0.23	0.039	23.9	210
14°	−0.184	0.123	$5.92e-05$	0.23	0.045	24	210
15°	−0.175	0.140	$6.89e-05$	0.23	0.050	24.15	210
16°	−0.162	0.162	$9.22e-05$	0.23	0.061	24.25	210
17°	−0.163	0.185	$1.37e-04$	0.23	0.074	24.5	210
18°	−0.172	0.210	$2.22e-04$	0.23	0.091	24.75	210
19°	−0.169	0.240	$3.45e-04$	0.23	0.114	25.25	210
20°	−0.176	0.270	$5.17e-04$	0.23	0.137	25.25	300
21°	−0.169	0.300	$7.03e-04$	0.23	0.157	26	210
22°	−0.185	0.336	$1.08e-03$	0.23	0.191	25.5	210
23°	−0.185	0.369	$1.45e-03$	0.23	0.217	25.66	210
24°	−0.191	0.402	$2.01e-03$	0.23	0.245	25.65	300
25°	−0.193	0.431	$2.38e-03$	0.23	0.278	25.65	300
26°	−0.188	0.467	$2.65e-03$	0.23	0.302	25.8	300
27°	−0.194	0.503	$2.81e-03$	0.23	0.301	25.5	300
28°	−0.195	0.552	$2.63e-03$	0.23	0.291	25.5	305
29°	−0.195	0.590	$2.33e-03$	0.23	0.271	25.3	250
30°	−0.198	0.623	$2.04e-03$	0.23	0.255	25.1	325

angle -1°. The elemental pitch can be obtained by adding the blade pitch angle to the element's local twist angle. The computations are carried out for all 10 elements; however, the results here are presented for element number 5 only to avoid the repetition of similar statistics.

Since the model is based on aerodynamic characteristics of an FX 79-W-151A, for comparison purpose the airfoil data file of AeroDyn is replaced with measured aerodynamic characteristics of this airfoil (for measurement details see [14]).

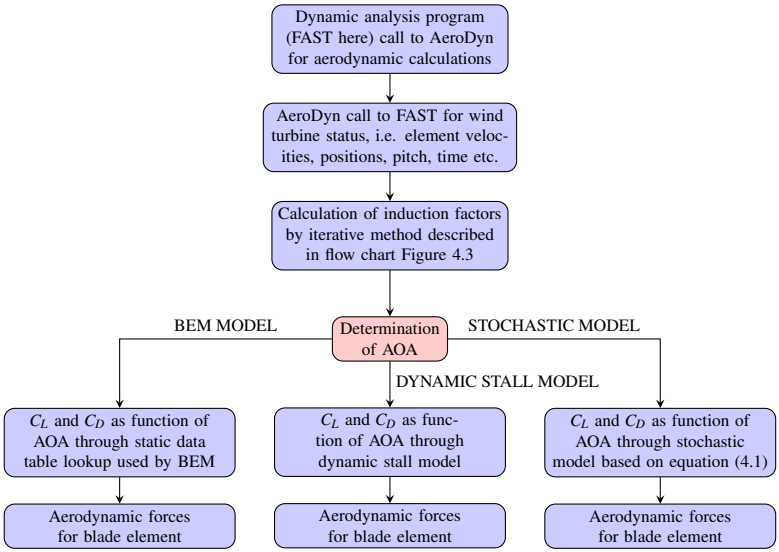

Figure 4.4: Flow chart for aerodynamic forces calculation.

Table 4.3: Blade local design parameters along the span. Taken from FAST archive (Test03_AD.ipt).

No. of element	Nodal radius [m]	Twist angle [°]	Element span [m]	Chord length [m]
1	1.81	5.80	1.26	0.86
2	3.07	5.20	1.26	1.05
3	4.33	4.66	1.26	1.15
4	5.58	3.73	1.26	1.12
5	6.84	2.64	1.26	1.05
6	8.10	1.59	1.26	0.98
7	9.36	0.73	1.26	0.89
8	10.61	0.23	1.26	0.78
9	11.87	0.08	1.26	0.65
10	13.13	0.03	1.26	0.49

For wind input, the full field turbulence simulated binary wind data file is used. The file represents all three components of the wind vector created with TurbSim program. The components are variable in time and space obtained at each element each moment by subroutine interpolations. A summary of the meteorological parameters of the wind data file is given in Table 4.4.

It has to be stressed that the model parameters have been derived from wind tunnel measurements in fractal square grid generated stationary turbulence, while the simulation uses synthetic turbulent inflow according to

Table 4.4: Meteorological boundary conditions of the wind data file. Taken from FAST archive.

Turbulence model used	: IEC von Karman
IEC standard	: IEC 61400-1 Ed. 2: 1999
Turbulence characteristic	: A
IEC turbulence type	: Normal turbulence model
Reference height (hub-height)	: 42.7 m
Reference wind speed (mean speed at hub-height)	: 12 m/s
Power law exponent	: 0.2
Surface roughness length	: 0.03 m
Interpolated hub-height turbulence intensity	: 15%

Table 4.4. To compensate at least partially for the different flow situations, the diffusion function of the basic model equation (4.3) is multiplied with a correction factor obtained by dividing synthetic wind input interpolated hub-height turbulence intensity with fractal square grid generated turbulence intensity. Due to the high complexity of turbulence, this can nevertheless not ensure completely comparable flow situations.

As described in Section 4.2, AeroDyn can not be operated independently, but has to be initiated by a dynamic analysis code. Here it is invoked by FAST, which uses a combined modal and multi-body dynamics representation. In FAST, the wind turbine blades and tower are modeled by applying the linear representation considering small deflections with mode shapes (degrees of freedom (DOF)) listed in Table 4.5 [6, 28]. FAST collects the basic information from its primary input file containing the details of wind turbine operating conditions and the basic geometry. For additional information such as blade properties, tower properties, furling properties, wind time histories and the aerodynamic characteristics, FAST reads some supplementary files [6].

Table 4.5: Wind turbine mode shapes and configuration. Taken from FAST archive (Test03.fst).

Number of blades used	: 3
First and second flap-wise blade mode DOF	: Yes
First edge-wise blade mode DOF	: Yes
Drivetrain rotational-flexibility DOF	: Yes
Generator DOF	: Yes
Yaw DOF	: Yes
First and second fore-aft tower bending-mode DOF	: Yes
First and second side-to-side tower bending-mode DOF	: Yes
Initial or fixed rotor speed	: 53.33 rpm
Blade tip radius from rotor apex	: 13.76 m
Hub radius from rotor apex to blade root	: 1.18 m
Tower height from ground level to rotor-shaft (hub-height)	: 42.7 m

Once FAST calls AeroDyn and exchanges the information on the model status including elemental pitch and velocities, AeroDyn starts to compute the elemental aerodynamic forces. The velocity components are expressed normal and tangential to the plane of rotation.

4.4.2 Results

Results are achieved for a blade element following the numerical setup described in Section 4.4.1. The force calculations are performed using the classical BEM, dynamic stall and stochastic models according to procedure given in flow chart Figure 4.4. The TurbSim generated synthetic wind is used as an input to AeroDyn. Simulations are performed for 10 realizations of 10 minutes of wind input. The synthetic wind, containing irregular speed and irregular turbulence level, led to strong fluctuations in local wind components and AOA as expected; see Figure 4.5. The figure portrays the complex fluctuations of the axial velocity component experienced by the blade element and its effect on AOA dynamics; compare [29]. The variations in velocity component are proportional to the AOA, i.e., the higher the wind fluctuations, the higher the AOA variation. A pronounced oscillation at $T = 1.13\,\mathrm{s}$ is visible in Figure 4.5, which possibly stems from boundary layer shear effects, as the tower-blade interaction was not included in the simulations[5].

The blade aerodynamics is function of the AOA, therefore, a change in AOA means a change in aerodynamic forces; compare Figure 4.5(b) with Figure 4.6. Figure 4.6 shows the resulting aerodynamic forces behavior for the selected element, where the force coefficient signals obtained with classical BEM represent the mean force dynamics as expected, being dependent on mean aerodynamic characteristics of the airfoil. The force coefficient signals achieved with the dynamic stall model represent the force dynamics with small fluctuations around the mean, while the force coefficient signals contributed by the stochastic model represent the force dynamics with extended local dynamics around the mean compared to the dynamic stall model. The means of the dynamic stall and stochastic models' local force dynamics along the signals match almost perfectly with the classical BEM model force signals.

In order to investigate the quality of the stochastic model results, their statistical properties are compared with the classical BEM and dynamic stall models' results in terms of increment probability density functions (PDFs). The increments in our case are the differences of an aerodynamic

[5]The appearance of harmonics of the 1P period seems to be typical for the rotating frame of reference of the rotor [30].

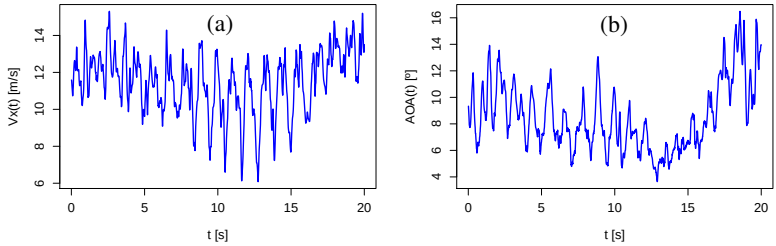

Figure 4.5: Excerpt of local axial wind velocity component and AOA time series for a blade element. (a) Local axial wind component experienced by the blade element and (b) local AOA. Note the rotor oscillation at $T = 1.13\,\mathrm{s}$ in (a) and (b), which possibly stems from ground boundary layer shear effects[5]. The oscillation in (b) is less visible because of short excerpt; however, it is present at the same period.

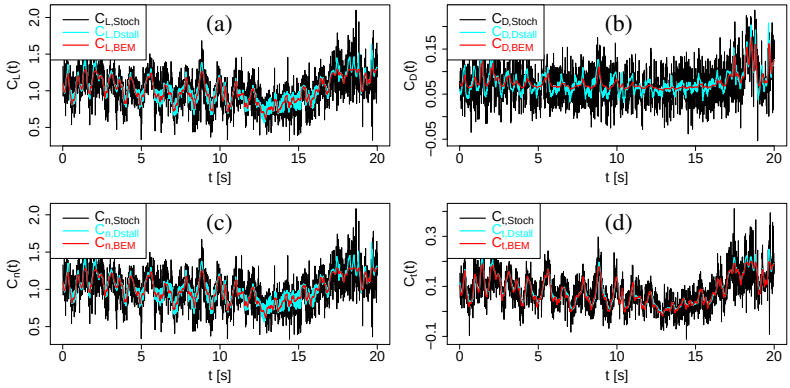

Figure 4.6: Excerpt of the stochastic model, the dynamic stall model and the classical BEM model aerodynamic forces time series for a blade element. Black represents the stochastic model forces, cyan the dynamic stall model forces and red the classical BEM model forces (color online). (a) $C_{L,Stoch}(t)$, $C_{L,Dstall}(t)$ and $C_{L,BEM}(t)$, (b) $C_{D,Stoch}(t)$, $C_{D,Dstall}(t)$ and $C_{D,BEM}(t)$, (c) $C_{n,Stoch}(t)$, $C_{n,Dstall}(t)$ and $C_{n,BEM}(t)$, and (d) $C_{t,Stoch}(t)$, $C_{t,Dstall}(t)$ and $C_{t,BEM}(t)$.

force over a specific time lag described as [31]

$$\delta x(t,\tau) = x(t+\tau) - x(t). \tag{4.6}$$

The increment statistics are basically two-point statistics, which determine

the nature of a parameter variation against a selected time lag. Using equation (4.6), the increment signals of the aerodynamic forces are derived for different time lags. Increment PDFs of the stochastic, dynamic stall and classical BEM models' results for different time lags are shown in Figures 4.7, 4.8 and 4.9, respectively.

For quantitative comparison, further kurtosis and standard deviations of the increment signals have been estimated. The kurtosis is calculated using the expression

$$\gamma_2 = \frac{\langle (x-\bar{x})^4 \rangle}{\sigma_x^4} - 3, \tag{4.7}$$

where γ_2 is the excess kurtosis, $\langle (x-\bar{x})^4 \rangle$ the fourth moment around the mean and σ_x^4 the square of the variance of the probability distribution. The $\gamma_2 = 0$ resemble a normal distribution, $\gamma_2 > 0$ a distribution with sharp peak and long heavy tails, and $\gamma_2 < 0$ a distribution with round peak and short light tails. The excess kurtosis is a measure of the deviation of PDF shape from the normal distribution.

Figure 4.7 presents the increment PDFs for stochastic model results, where all four aerodynamic force coefficients look similar at all three time lags except some differences at the tails. All PDFs almost resemble the normal distribution shape up to $\pm 3\sigma$; compare with added Gaussian fit. At the tails, the PDFs deviate from the Gaussian distribution and show intermittent behavior. To quantify for these shapes, the kurtosis and standard deviations of the increment signals have been estimated as given in Table 4.6. The estimations show slight to pronounced higher positive kurtosis for all four aerodynamic force coefficient signals at the selected time lags, meaning that the increment PDFs have slight to pronounced heavier tails. The main reason for this effect seem to be the non-linear lift and drag characteristics of the airfoil over AOA. The standard deviations of the increment signals in each force coefficient case at all three time lags are close to each other in magnitude; see Table 4.6.

Figure 4.8 presents the increment PDFs for dynamic stall model results. In this case, the increment PDFs except those of the drag coefficient, resemble similar shape with minor differences at the tails. The drag increment PDFs present heavier tails compared to other three force coefficients. However, the increment PDFs of all forces correspond fairly to the normal distribution up to $\pm 3\sigma$ (compare with added Gaussian fit) at all three time lags. The estimated kurtosis values given in Table 4.7 indicate very slight to pronounced heavier tails for all force coefficient signals except almost no deviations in case of the lift, normal force and tangential force coefficients at higher time lags. The contribution of pronounced intermittency in the force signals is believed to stem from the same phenomenon as described

in stochastic model case. The standard deviations of the all three increment signals in each force case depict increase with an increase in time lag; see Table 4.7.

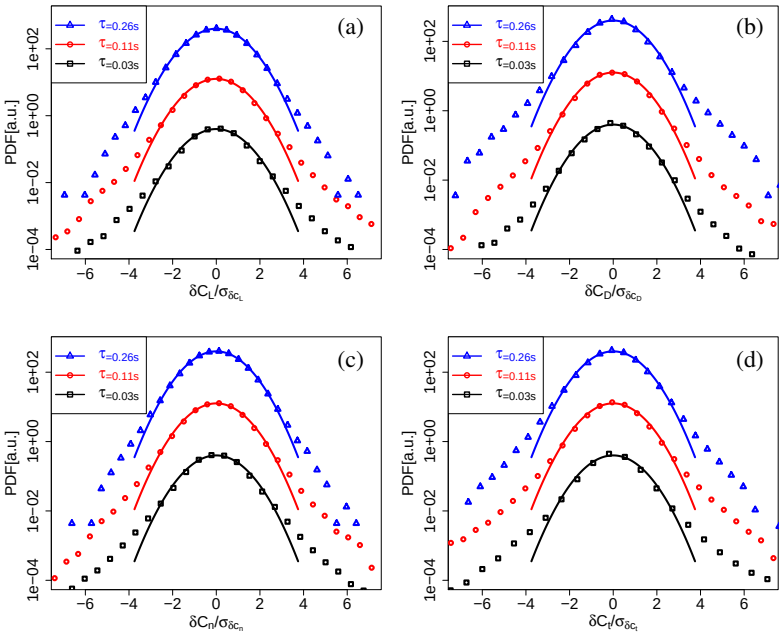

Figure 4.7: Increment PDFs of the stochastic model force coefficients for a blade element at time lags $\tau = (0.03, 0.11, 0.26)$ s in ascending order from bottom to top. The PDFs are added with a Gaussian fit having identical standard deviation (solid line) and shifted vertically for clarity of the display. The force coefficients are normalized with their standard deviations. (a) Lift coefficient increment $\delta C_L(t,\tau)$ PDFs, (b) Drag coefficient increment $\delta C_D(t,\tau)$ PDFs, (c) Normal force coefficient increment $\delta C_n(t,\tau)$ PDFs, and (d) Tangential force coefficient increment $\delta C_t(t,\tau)$ PDFs.

Table 4.6: Kurtosis and standard deviation of the increment signals of the stochastic model force coefficients at different time lags.

Inrement	Kurtosis				Standard deviation			
τ[s]	δC_L	δC_D	δC_n	δC_t	δC_L	δC_D	δC_n	δC_t
0.03	1.80	1.37	1.66	3.04	0.26	0.06	0.26	0.08
0.11	0.98	1.01	0.90	1.59	0.29	0.06	0.28	0.09
0.26	0.44	1.42	0.40	0.96	0.31	0.06	0.30	0.09

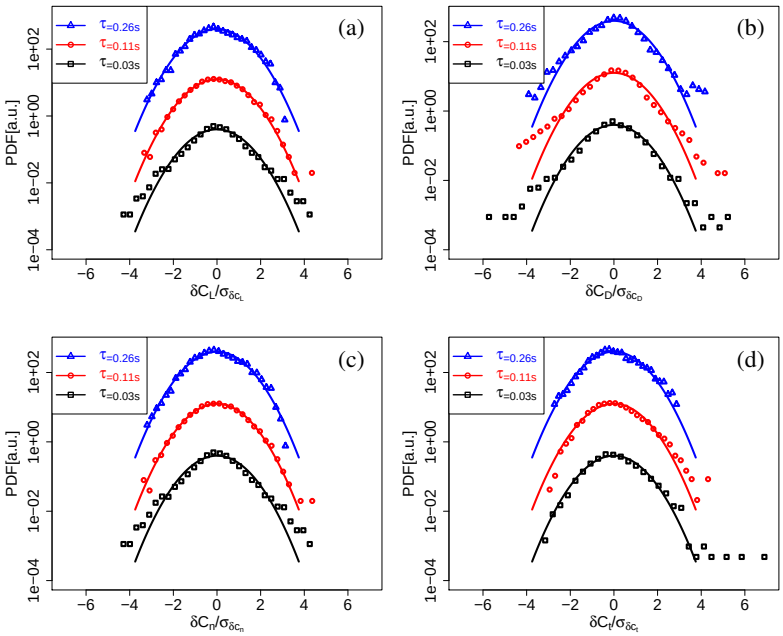

Figure 4.8: Increment PDFs of the dynamic stall model force coefficients for a blade element at time lags $\tau = (0.03, 0.11, 0.26)$ s in ascending order from bottom to top. The PDFs are added with a Gaussian fit having identical standard deviation (solid line) and shifted vertically for clarity of the display. The force coefficients are normalized with their standard deviations. (a) Lift coefficient increment $\delta C_L(t,\tau)$ PDFs, (b) Drag coefficient increment $\delta C_D(t,\tau)$ PDFs, (c) Normal force coefficient increment $\delta C_n(t,\tau)$ PDFs, and (d) Tangential force coefficient increment $\delta C_t(t,\tau)$ PDFs.

Table 4.7: Kurtosis and standard deviation of the increment signals of the dynamic stall model force coefficients at different time lags.

Inrement	Kurtosis				Standard deviation			
τ[s]	δC_L	δC_D	δC_n	δC_t	δC_L	δC_D	δC_n	δC_t
0.03	1.38	2.23	1.40	1.01	0.06	0.01	0.06	0.01
0.11	0.06	1.84	0.07	0.33	0.11	0.03	0.11	0.03
0.26	−0.09	1.34	−0.09	−0.05	0.17	0.04	0.17	0.05

Similarly, Figure 4.9 shows the increment PDFs for classical BEM model results. Here, except drag coefficient, the increment PDFs of other three force coefficients portray similar shape for same time lags. The in-

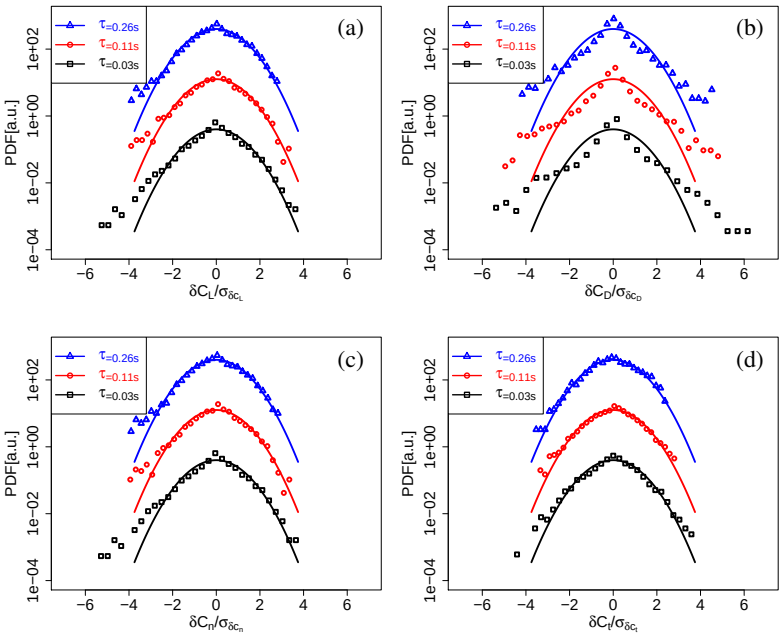

Figure 4.9: Increment PDFs of the classical BEM model force coefficients for a blade element at time lags $\tau = (0.03, 0.11, 0.26)$ s in ascending order from bottom to top. The PDFs are added with a Gaussian fit having identical standard deviation (solid line) and shifted vertically for clarity of the display. The force coefficients are normalized with their standard deviations. (a) Lift coefficient increment $\delta C_L(t,\tau)$ PDFs, (b) Drag coefficient increment $\delta C_D(t,\tau)$ PDFs, (c) Normal force coefficient increment $\delta C_n(t,\tau)$ PDFs, and (d) Tangential force coefficient increment $\delta C_t(t,\tau)$ PDFs.

Table 4.8: Kurtosis and standard deviation of the increment signals of the classical BEM model force coefficients at different time lags.

Inrement	Kurtosis				Standard deviation			
τ[s]	δC_L	δC_D	δC_n	δC_t	δC_L	δC_D	δC_n	δC_t
0.03	1.37	6.62	1.42	0.72	0.03	0.01	0.03	0.01
0.11	0.78	4.43	0.81	0.28	0.08	0.02	0.08	0.03
0.26	0.49	3.31	0.51	−0.02	0.14	0.03	0.14	0.05

crement PDFs of the lift, normal force and tangential force coefficients, resemble fairly the normal distribution shape up to $\pm 3\sigma$ (compare with added Gaussian fit), whereas the drag coefficient correspond to the inter-

mittent shape. The evaluated kurtosis given in Table 4.8 indicate strong heavier tails for drag coefficient increment PDFs at all three time lags. The other three force coefficients show slight to pronounced heavier tails for all three time lags except negligible lighter tails for higher time lag in case of the tangential force coefficient. The contribution of strong intermittency in the drag coefficient as well as slight to pronounced intermittency in other force coefficients can probably be addressed to the same phenomenon as in the stochastic model case. The standard deviations of the force coefficient signals follow the same behavior as in the dynamic stall model case above; compare Tables 4.7 and 4.8.

4.5 Discussion and outlook

The stochastic model of the lift and drag dynamics for an airfoil FX 79-W-151A described in Section 4.3 has been integrated to AeroDyn in the context of BEM wake model. The forces are obtained through the classical BEM, dynamic stall and stochastic models used by AeroDyn. For wind input, the full field turbulence simulated binary wind data is used. The forces are estimated for 10 blade elements; however, the results are analyzed here for one element only to avoid the repetition of similar statistics. With this ansatz it could be shown that local, short-time fluctuations of aerodynamic forces can be integrated as a stochastic model into a current WEC simulation tool.

The comparison of force time series given in Figure 4.6 show that the classical BEM model force coefficient signals represent the mean dynamics as expected, being dependent on mean aerodynamic characteristics of the airfoil. The dynamic stall model forces reflect small fluctuations around the mean, whereas the stochastic model introduces additional extended local force dynamics around the mean. The means of the local force dynamics achieved with dynamic stall and stochastic models seem to coincide with the classical BEM model force coefficient signals. Nevertheless, the stochastic model contributes additional extended dynamic response in terms of local force fluctuations, which is neglected by the classical BEM model fully and partially by the dynamic stall model.

The statistics of the stochastic and dynamic stall models presented in Figures 4.7 and 4.8 show good consistency. The increment PDFs of stochastic model force coefficients resemble normal distributions up to $\pm 3\sigma$. Similarly, the increment PDFs of dynamic stall model force coefficients also resemble fairly a normal distribution up to $\pm 3\sigma$. Both the stochastic and dynamic stall models' force increment PDFs yield slight to pronounced intermittency due to the non-linear lift and drag characteristics

of the airfoil over AOA. The magnitude of the standard deviations of the stochastic model force increment signals is significantly higher that of the dynamic stall model; compare Tables 4.6 and 4.7. That is because the dynamic stall model forces possess smaller magnitudes of local fluctuations compared to the stochastic model. Moreover, the behavior of the standard deviations of the increment signals is different in both the stochastic and dynamic stall model cases. The standard deviations in the stochastic model case seem nearly stable for all time lags, whereas for the dynamic stall model case they are proportional to time lags.

Similarly, the comparison of statistics between stochastic and classical BEM models given in Figures 4.7 and 4.9 also reflect good consistency except for the drag coefficient. The increment PDFs of the stochastic and classical BEM models' force coefficients resemble normal distributions up to $\pm 3\sigma$ besides the BEM model drag coefficient. The intermittency in this range in the stochastic model drag coefficient is mostly covered by Gaussian fluctuations. The strong intermittency in the BEM model drag coefficient as well as slight to pronounced intermittency in other force coefficients in both the stochastic and classical BEM model cases can probably be addressed to the same reason described above. The magnitude of the stochastic model force standard deviations is larger than the classical BEM model forces; compare Tables 4.6 and 4.8. The reason is the extended local force dynamics in case of stochastic model. The behavior of the standard deviations of the increment signals between stochastic and classical BEM models is very similar as observed between stochastic and dynamic stall models.

As described in Section 4.4.1 the stochastic model parameters have necessarily been obtained under different conditions than the simulations carried out here. As a first compensation, the diffusion function has been scaled according to the interpolated hub-height turbulence intensity of wind input taken for the present computations. This can; however, not guarantee completely comparable flow situations. Therefore, the comparability of results between the stochastic model and the dynamic stall and BEM models is limited at the current state. For better quantitative comparison of stochastic versus dynamic stall and BEM models, in the future the stochastic model parameters have to be derived from measurements in more realistic flow situations at wind turbine airfoils. Also a comparison to load measurements at a real WEC should be performed.

Additionally, at the present state, the stochastic model could not generate the expected intermittency in the resulting forces, which is probably washed-out by the Gaussian noise term of the model. To improve this point, multiplicative noise may be introduced to achieve intermittency in

the forces corresponding to intermittent properties of atmospheric flows, which is currently work in progress.

The stochastic model is being developed to extract and provide more complete local loading information on wind turbine blades, which could lead to an optimized rotor design under turbulent wind inflow. Here we have shown that the local force dynamics can be provided by a stochastic model integrated into existing BEM codes used by aerodynamic models such as AeroDyn. Further work will have to include more realistic model parameterization and corresponding experiments to allow for quantitative evaluation of the results.

We appreciate the open access to the FAST and AeroDyn archives granted by the NREL team. M. R. Luhur kindly acknowledges financial support for higher studies by Quaid-e-Awam University of Engineering, Sciences and Technology, Nawabshah, Pakistan.

4.6 Appendix A: Tip and root losses

The tip and root losses include the influence of vortices shedding from the tip and root of the blade. Due to pressure difference, the air flow around the blade tip into the wake leads to the formation of a tip vortex. Initially, there is decrease in the vortex diameter due to wake expansion (vortex stretching by wake), but later its diameter increases due to viscous effects [32]. Similar vortex shedding appears near the hub at root of the blade also. The wake pattern with described vortices for a rotating blade is shown in Figure 4.10.

The Figure 4.11 demonstrates an example of the effect of tip and root losses on an optimum blade design. It shows that tip loss correction factor decreases greatly as the radial position approaches to the blade tip. This leads to drastic increase in axial induction factor a, resulting in lower loading (lift and drag forces) at the tip. The increase in axial induction causes decrease in relative wind speed, therefore, decrease in flow angle as well as in AOA. As a result, the lift force becomes almost normal to the rotor plane having smaller tangential component, which leads to reduced torque and power. Similar phenomenon occurs at root of the blade also, as the blade root is at some distance from the rotor axis where wind flow through the disc inside the blade root radius is at free-stream velocity [26].

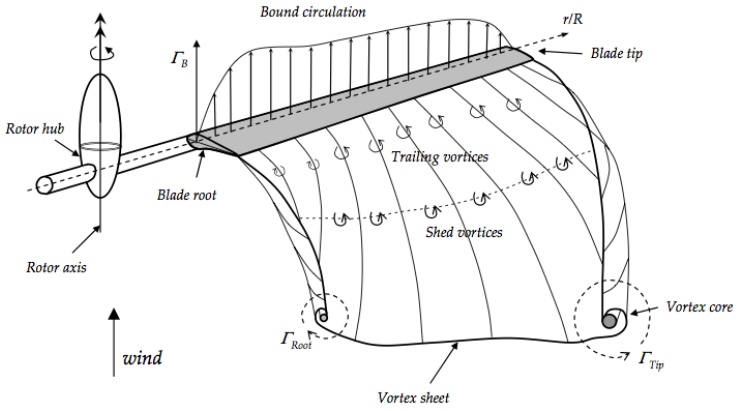

Figure 4.10: View of a wake pattern developed by a rotating blade of a wind turbine. Taken from [33].

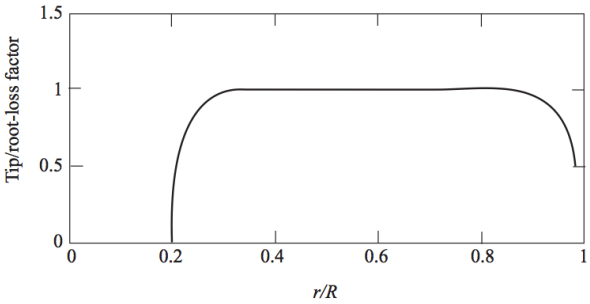

Figure 4.11: Radial distribution of combined tip and root loss correction factor for a three-bladed turbine optimized for TSR of 6 and blade root at 20% of the span. Taken from [26].

4.7 Appendix B: Correction for skewed wake

The wind turbines mostly operate at yaw angles because of unstable wind direction, and produce skewed wake as shown in Figure 4.12. In this misalignment, the upwind induced velocity gets smaller due to upwind orientation away from the wake, and downwind induced velocity gets higher being close to the wake.

This variation in induced velocities due to yaw misalignment, violets the assumption of axisymmetric flow considered in basic BEM theory. Therefore, a correction factor is needed to counterbalance for skewed wake

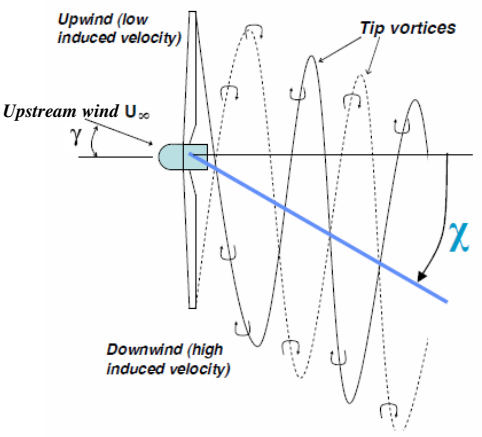

Figure 4.12: Yawed inflow with wake. Taken from [34].

effect produced by yaw misalignment. For this purpose, AeroDyn uses the extended Glauert's model by Pitt and Peters [24] based on steady inflow assumption. The expression reads

$$a_{skew} = a\left[1 + \frac{15\pi}{32}\frac{r}{R}tan\frac{\chi}{2}cos\psi\right], \tag{4.8}$$

where a_{skew} is the local element induction factor for skewed wake, χ the wake angle and ψ the blade azimuth angle. The yaw angle with rotor axis is slightly smaller than the wake angle and are related as [25]

$$tan\chi = \frac{U_\infty(sin\gamma - a\,tan\frac{\chi}{2})}{U_\infty(cos\gamma - a)}, \tag{4.9}$$

where γ is the yaw angle. According to Burton *et al.* [26] based on close approximate relationship between χ, γ, and a, equation (4.9) can be simplified further to

$$\chi = (0.6a + 1)\gamma. \tag{4.10}$$

Bibliography

[1] *Global wind report-Annual market update 2012*. Technical report, Global Wind Energy Council, Brussels, Belgium, April 2013.

[2] L. J. Vermeer, J. N. Sørensen and A. Crespo. Wind turbine wake aerodynamics. *Progress in Aerospace Sciences*, 39(6-7):467–510, August–October 2003.

[3] S. Liu and I. Janajreh. Development and application of an improved blade element momentum method model on horizontal axis wind turbines. *International Journal of Energy and Environmental Engineering*, 3:30 (10 pages), October 2012.

[4] K. Åhlund. *Investigation of the NREL NASA/Ames Wind Turbine Aerodynamics Database*. Scientific report FOI-Rñ1243ñSE, Swedish Defence Research Agency, Stockholm, Sweden, June 2004.

[5] M. O. L. Hansen and H. A. Madsen. Review Paper on Wind Turbine Aerodynamics. *Journal of Fluids Engineering*, 133(11):114001 (12 pages), October 2011.

[6] J. M. Jonkman and M. L. Buhl Jr. *FAST User's Guide*. Technical report NREL/EL-500-38230, National Renewable Energy Laboratory, Golden, Colorado, USA, August 2005.

[7] D. J. Laino and A. C. Hansen. *User's Guide to the Wind Turbine Dynamics Computer Program YawDyn*. Technical report prepared for NREL under subcontract No. TCX-9-29209-01, University of Utah, Salt Lake City, USA, January 2003.

[8] D. J. Laino and A. C. Hansen. *User's Guide to the Computer Software Routines AeroDyn Interface for ADAMS*. Technical report prepared for NREL under subcontract No.TCX-9-29209-0, University of Utah, Salt Lake City, USA, September 2001.

[9] S. Mulski. SIMPACK Multi-Body Simulation. *Wind and Drivetrain Conference*, SIMPACK AG, Hamburg, Germany, September 2012.

[10] M. L. Buhl Jr. and A. Manjock. *A Comparison of Wind Turbine Aeroelastic Codes Used for Certification*. Conference paper NREL/CP-500-39113, National Renewable Energy Laboratory, Golden, Colorado, USA, January 2006.

[11] S. Øye. *FLEX5 User Manual*. Technical report, Danske Techniske Hogskole, 1999.

[12] P. J. Moriarty and A. C. Hansen. *AeroDyn Theory Manual*. Technical report NREL/EL-500-36881, National Renewable Energy Laboratory, Golden, Colorado, USA, January 2005.

[13] G. A. Weinzierl. *A BEM Based Simulation-Tool for Wind Turbine Blades with Active Flow Control Elements*. Diploma thesis, Technical University of Berlin, Germany, April 2011.

[14] M. R. Luhur, J. Peinke, J. Schneemann and M. Wächter. Stochastic modeling of lift and drag dynamics under turbulent wind inflow conditions. *Wind Energy*, January 2014. doi: 10.1002/we.1699, published online.

[15] D. J. Laino and A. C. Hansen. *User's Guide to the Wind Turbine Aerodynamics Computer Software AeroDyn*. Technical report prepared for NREL under subcontract No. TCX-9-29209-01, University of Utah, Salt Lake City, USA, December 2002.

[16] N. D. Kelley and B. J. Jonkman. *Overview of the TurbSim Stochastic Inflow Turbulence Simulator*. Technical report NREL/TP-500-4113, National Renewable Energy Laboratory, Golden, Colorado, USA, April 2007.

[17] B. J. Jonkman and L. Kilcher. *TurbSim User's Guide: Version 1.06.00*. Technical report draft version, National Renewable Energy Laboratory, Golden, Colorado, USA, September 2012.

[18] J. Méndez and D. Greiner. Wind Blade Chord and Twist Angle Optimization by Using Genetic Algorithms. *Proceedings of the Fifth International Conference on Engineering Computational Technology*, Civil-Comp Press, Spain, 2006.

[19] J. F. Manwell, J. G. McGowan and A. L. Rogers. *Wind Energy Explained: Theory, Design and Application, Second Edition*. John Wiley & Sons, Chichester, UK, 2009.

[20] H. Glauert. *Airplane Propellers, Aerodynamic Theory W.F. Durand Edition*. Springer, Berlin, Germany 1935.

[21] M. L. Buhl Jr. *A new empirical relationship between thrust coefficient and induction factor for the turbulent windmill state*. Technical report NREL/TP-500-36834, National Renewable Energy Laboratory, Golden, Colorado, USA, August 2005.

[22] H. Glauert. *A General Theory of the Autogyro, Volume 1111 of Reports and Memoranda Edition*. British ARC, UK, 1926.

[23] H. Glauert. *The Analysis of Experimental Results in the Windmill Brake and Vortex Ring States of an Airscrew, Volume 1026 of Reports and Memoranda Edition*. HMSO, London, UK, 1926.

[24] D. M. Pitt and D. A. Peters. Theoretical Prediction of Dynamic-Inflow Derivatives. *Vertica*, 5(1):21–34, March 1981.

[25] R. P. Coleman, A. M. Feingold and C. W. Stempin. *Evaluation of the Induced-Velocity Field of an Idealized Helicopter Rotor*. Wartime report NACA ARR L5E10, National Advisory Committee for Aeronautics, Washington, USA, June 1945.

[26] T. Burton, D. Sharpe, N. Jenkins and E. Bossanyi. *Wind Energy Handbook, Second Edition*. John Wiley & Sons, Chichester, UK, 2011.

[27] H. Risken. *The Fokker-Planck Equation, Second Edition*. Springer, Berlin, Germany, 1996.

[28] A. Cordle. *State-of-the-art in design tools for floating offshore wind turbines*. Deliverable report under contract No. 019945 (SES6), UpWind project, Bristol, UK, March 2010.

[29] B. Stoevesandt, J. Peinke. Changes in angle of attack on blades in the turbulent wind field. *Proceedings of EWEC 2009*, Parc Chanot, Marseille, France, 2009.

[30] J. Jonkman. Personal communication, National Renewable Energy Laboratory, USA, 2014.

[31] A. Morales, M. Wächter and J. Peinke. Characterization of wind turbulence by higher order statistics. *Wind Energy*, 15(3):391–406, April 2012.

[32] N. J. Vermeer. How big is a tip vortex? *Proceedings 10th IEA symposium on aerodynamics of wind turbines*, 1996.

[33] T. Sant. *Improving BEM-based Aerodynamic Models in Wind Turbine Design Codes*. PhD thesis, Delft University Wind Energy Research Institute (DUWIND), the Netherlands, 2007.

[34] G. J. W. von Bussel. Recent advancements in yawed flow aerodynamics. *Dutch Wind Workshops*, October 2008.

Chapter 5

Conclusion and future work

Conclusion

The thesis manifests the application of stochastic processes in the field of wind energy. The stochastic processes can describe the complex systems composed of large number of microscopic subsystems with irregular behavior on fast time scales. The behavior of such systems is generally treated as random variables. The systems with many degrees of freedom can be described with low dimensional macroscopic order parameter equations and the effect of microscopic degrees of freedom can be superposed through dynamical noise. The selection of a particular class of stochastic processes, wholly depends on the nature of the system under investigation. Here, the approach is applied in the context of Langevin processes used to describe the dynamics of complex systems with drift and diffusion functions. The process can be applied directly on the measured data to approximate the system behavior in statistical sense.

The atmospheric wind being highly turbulent and intermittent, contributes highly dynamic forces on the wind turbines rotor blades and other structure. In our case, the Langevin approach is applied to describe the dynamic behavior of the aerodynamic forces on blades observed in time. The aim of the work was; better description and characterization of the aerodynamic forces acting on rotor blades in open atmosphere. In particular, the modeling of lift and drag dynamic response for blades exposed to unsteady flows, which could extract the forces with local dynamics disregarded by existing dynamic load models. The proposed model aims to replace the traditional static lookup tables used by aerodynamic codes, which in combination with a WEC model could provide a stochastic rotor model leading to an improved rotor design. The comprehensive view of the developed

concept is described as follows:

- An extended stochastic model for lift and drag dynamics based on wind tunnel measurements for an airfoil FX 79-W-151A has been introduced. Dynamic measurements of lift and drag forces were performed in the wake of a fractal square grid (at turbulence intensity of 4.6%), which generates the velocity fluctuations with similar statistics as observed for free field wind situations. The model parameters have been derived from empirical data for AOAs 0° to 30°. The extension in basic model is introduced to account for oscillation effects contained in lift and drag dynamics, which probably stem from unsteady aerodynamic effects. It is observed that model in the existing state reproduces well matching statistics with the actual measurements. Further, the model brings additional insight on local dynamics of lift and drag forces compared to standard averaging procedure, which follows only mean dynamics of the forces.

- To test the developed concept, in the first step, the stochastic model has been integrated into standard BEM model. The results show that in comparison to standard BEM model, the BEM model combined with stochastic model, additionally reflects the local force dynamics as expected. This suggests that the local force dynamics can be provided by a stochastic model integrated into existing BEM codes.

- In the further step, the stochastic model has been integrated into an aerodynamic model AeroDyn of the National Renewable Energy Laboratory. The simulations are performed using full field turbulence simulated binary wind data input. The stochastic forces are analyzed for a rotating blade element and compared with the classical BEM and dynamic stall models for similar situations. The observations manifest that the stochastic model provides additional extended dynamic response in terms of local force fluctuations, which is disregarded by the classical BEM model fully and dynamic stall model partly.

  The comparison of statistics between stochastic, dynamic stall and classical BEM models' results show good consistency except BEM model drag coefficient. The intermittency in stochastic model drag coefficient is mostly covered by Gaussian fluctuations. The strong intermittency in BEM model drag coefficient and slight to pronounced intermittency in other force coefficients in stochastic, dynamic stall and BEM model cases could be addressed to the non-linear lift and drag characteristics of the airfoil over AOA. The magnitude of the

stochastic model force standard deviations is significantly higher that of the dynamic stall and BEM models' forces standard deviations because of extended local force dynamics.

It is important to mention that the stochastic model parameters have necessarily been obtained under different conditions than the simulations carried out here. As a first compensation, the diffusion function has been scaled according to interpolated hub-height turbulence intensity of wind input taken for present computations. This can not guarantee completely comparable flow situations. Therefore, the comparability of results between the stochastic model and the traditional dynamic stall and BEM models is limited at the current state. For better quantitative comparison of stochastic versus dynamic stall and BEM models, the stochastic model parameters in future, have to be derived from measurements in more realistic flow situations at wind turbine airfoils. Additionally, a comparison to load measurements at a real WEC should be performed. Nevertheless, the aim of this has been to show that with this ansatz local, short-time fluctuations of aerodynamic forces can be integrated as a stochastic model into a current WEC simulation tool.

Therefore, it could be concluded that an improvement to table lookup approach used by traditional aerodynamic models has been achieved.

Future work

The outline of further investigations may read:

- The quantitative comparison of stochastic model statistics with actual measurements suggests that extension part of the model yet needs some minor improvements. The error is believed to come from amplitude modulation (breathing) length of lift and drag taken on average basis, which in actual appears in a random fashion along the measured lift and drag time series. This needs further close investigations on occurrence of breathing pattern along the lift and drag time series.

- Further, at the present state, the stochastic model could not produce the expected intermittency in the resulting forces (achieved with model integration into AeroDyn), which is probably washed-out by the Gaussian white noise term of the model. To correct for this, multiplicative noise may be introduced to achieve the intermittency in the forces corresponding to intermittent properties of atmospheric flows.

- Here, as an example only one type of airfoil has been studied to develop and demonstrate the method and its application. Different airfoils possess different dynamics, and therefore, drift and diffusion functions will in principle differ for different airfoils. Moreover, these functions are also expected to differ for different turbulence parameters and to be influenced by further effects such as tower interaction, vertical wind shear, yawed inflow and aeroelastic effects. Further, the additional effects covered in the form of extension to the basic model are also expected to differ in these cases. Hence, for future developments, more airfoils are needed to be tested under different and realistic conditions.

- Moreover, the model has been developed considering two-dimensional (2D) flow on a blade element, whereas the real blades observe 3D flow in operation. Therefore, the effect of 3D flow especially in terms of transition from one element to other needs to be investigated, and respective corrections be fixed depending on the findings.

Declaration

I declare hereby that this is my own work and have written independently and the information taken from other sources has been duly acknowledged.

Oldenburg, September 09, 2014

.....
(Muhammad Ramzan Luhur)

Acknowledgements

I would like to thank *Prof. Dr. Joachim Peinke* for his supervision with innovative ideas and full cooperation including providing different opportunities to present our work in different conferences and seminars. I specially appreciate his polite style and best concept of academic freedom.

I also would like to thank *Dr. Matthias Wätcher* for his supervision and support. I offer my exceptional gratitudes for his helpful discussions and ideas.

My special thanks to *Jörge Schneemann* for access to his measured data and being co-author in one of my paper. I also offer my sincere thanks to *Patrick Milan* for useful discussions with him.

I am also grateful to all my colleagues for their fascinating company, sympathies and friendly atmosphere in the group. Many thanks to *Dr. Michael Hölling, Dr. Gerd Gülker, Dr. Bernhard Stoevesandt, Dr. Mohammad Reza Rahimitabar, Dr. Wided Medjroubi, Mehrnaz Anvari, Allan Morales, Philip Rinn, Jörg Dapperheld, Hendrik Heißelmann, David Bastine, Bastian Dose, Thomas Greve, Ali Hadjihosseini, Ivan Herraez Hernandez, Christina Heßeling, Agnieszka Hölling, Tim Homeyer, Fatima Keshtova, Michael Langner, Jarek Puczylowski, Stanislav Rockel, Nils Kirrkamm, Anne Laupichler, Jose-Placido Parra Viol, Hamid Rahimi, Nico Reinke, Katrin Schmietendorf, Dominik Traphan, Lena Vorspel and Agnes Seeger.* I am sorry if I missed any friend's name.

Finally I thank my family for their support and sacrifices to achieve this goal. I dedicate this work to my father *Late Bahadur Luhur and family*.

Curriculum Vitae

Personal data

Name	Muhammad Ramzan Luhur
Date of birth	05.10.1977
Place of birth	Larkana, Pakistan

Education

1983 – 1995	Primary, secondary and higher secondary school education, district Larkana, Pakistan.
1997 – 2002	Bachelor in Mechanical Engineering, Department of Mechanical Engineering, Quaid-e-Awam University of Engineering, Sciences and Technology (QUEST), Nawabshah, Pakistan.
2007 –2009	Master of Science in Sustainable Energy Engineering, Department of Energy Technology, Royal Institute of Technology (KTH), Stockholm, Sweden.
2010 –2014	PhD in the area of wind turbine rotor aerodynamic forces (successfully defended on September 08, 2014), ForWind, Institute of Physics, Carl von Ossietzky University of Oldenburg, Germany.

Professional Experience

2003 – 2004	Assistant Manager Mechanical, Chemi Group of Industries at their Chemi Viscofibre Plant at Nawabshah, Pakistan.
2004 – todate	Lecturer, Mechanical Engineering Department, Quaid-e-Awam University of Engineering, Sciences and Technology, Nawabshah, Pakistan. On study leave during MSc and PhD.

Journal Publications

M. R. LUHUR, J. PEINKE, J. SCHNEEMANN and M. WÄCHTER, Stochastic modeling of lift and drag dynamics under turbulent inflow conditions, *Wind Energy*, 2014. doi: 10.1002/we.1699.

M. Wächter and J. Peinke have the supervision role in this work. J. Schneemann contributed the wind tunnel measurements. The scientific work is done by M. R. Luhur.

M. R. LUHUR, J. PEINKE and M. WÄCHTER, Stochastic modeling of lift and drag dynamics to obtain aerodynamic forces with local dynamics on rotor blade under unsteady wind inflow, *Mehran University Research Journal of Engineering & Technology*, 33(1):39-48, 2014.

M. Wächter and J. Peinke have the supervision role in this work. The scientific work is done by M. R. Luhur.

M. R. LUHUR, J. PEINKE, M. KÜHN and M. WÄCHTER, Stochastic model for aerodynamic force dynamics on wind turbine blades in unsteady wind inflow, *Submitted to Journal of Computational and Nonlinear Dynamics*, 2014.

M. Wächter, J. Peinke and M. Kühn have the supervision role in this work. The scientific work is done by M. R. Luhur.

Conference Publications

M. R. LUHUR, J. SCHNEEMANN, P. MILAN and J. PEINKE, Stochastic modeling of lift dynamics in turbulent inflows, *EAWE 6th PhD Seminar on Wind Energy in Europe*, NTNU Trondheim, Norway, 30th September-1st October 2010.

J. SCHNEEMANN, P. MILAN, M. R. LUHUR, P. KNEBEL and J. PEINKE, Lift measurements in turbulent flow conditions, *DEWEK conference*, Bremen, Germany, 17th-18th November 2010.

M. R. LUHUR, P. MILAN, J. SCHNEEMANN, M. WÄCHTER and J. PEINKE, Stochastic modeling of lift dynamics under turbulent conditions, *75th annual meeting of DPG*, Dresden, Germany, 13th-18th March 2011.

M. R. LUHUR, M. WÄCHTER and J. PEINKE, Stochastic modeling of lift and drag dynamics under turbulent conditions, *EWEA conference*, Copenhagen, Denmark, 16th-19th April 2012.

M. R. LUHUR, J. PEINKE and M. WÄCHTER, Stochastic modeling of lift and drag dynamics for a rotor aerodynamic model considering turbulent inflow, *EAWE 8th PhD seminar on Wind Energy in Europe*, ETH Zurich, Switzerland, 12th-14th September 2012.